2016

Understanding the photostability of perovskite solar cell

Pranav Hemanta Joshi
Iowa State University

Understanding the photostability of perovskite solar cell

by

Pranav H Joshi

A dissertation submitted to the graduate faculty

in partial fulfillment of the requirements for the degree of

DOCTOR OF PHILOSOPHY

Major: Electrical Engineering

Program of Study Committee:
Vikram Dalal, Major Professor
Rana Biswas
Sumit Chaudhary
Ruth Shinar
Mani Mina

Iowa State University

Ames, Iowa

2016

|| श्री ||

TABLE OF CONTENTS

LIST OF FIGURES

LIST OF TABLES

NOMENCLATURE

V_{oc}	Open circuit voltage
I_{sc}	Short circuit current
FF	Fill factor
PCE	Power conversion efficiency
R_s	Series resistance
R_{sh}	Shunt resistance
HOMO	Highest occupied molecular orbital
LUMO	Lowest unoccupied molecular orbital
TCO	Transparent conducting oxide
ITO	Indium tin oxide
FTO	Florine doped tin oxide
PEDOT:PSS	Poly(3,4-ethylenedioxythiophene) poly(styrenesulfonate)
P3HT	Poly(3-hexylthiophene-2,5-diyl)
Sprio-OMeTAD	$N^2,N^2,N^{2'},N^{2'},N^7,N^7,N^{7'},N^{7'}$-octakis(4-methoxyphenyl)-9,9′-spirobi[9H-fluorene]-2,2′,7,7′-tetramine
PTAA	Poly(triaryl amine), Poly[bis(4-phenyl)(2,4,6-trimethylphenyl)amine]
PCBM	Phenyl-C61-butyric acid methyl ester
PTB7	Poly[[4,8-bis[(2-ethylhexyl)oxy]benzo[1,2-b:4,5-b']dithiophene-2,6-diyl][3-fluoro-2-[(2-ethylhexyl)carbonyl]thieno[3,4-b]thiophenediyl]]

PTB7-Th	Poly[4,8-bis(5-(2-ethylhexyl)thiophen-2-yl)benzo[1,2-b;4,5-b']dithiophene-2,6-diyl-alt-(4-(2-ethylhexyl)-3-fluorothieno[3,4-b]thiophene-)-2-carboxylate-2-6-diyl)]
$PC_{70}BM$	Phenyl-C71-butyric acid methyl ester
MAI	Methylammonium iodide
FAI	Formamidium iodide
CB	Chlorobenzene
DCB	Dichlorobenzene
DMF	Dimethylformamide
DMSO	Dimethyl sulfoxide
PVDF	Polyvinylidene fluoride
PTFE	Polytetrafluoroethylene
SMU	Source measure unit
SCLC	Space charge limited current
UV-Vis	Ultraviolent-visual

ACKNOWLEDGMENTS

First and foremost, I would like to show my sincere gratitude towards Prof. Vikram Dalal, for giving my opportunity to work in his research group, and most importantly for being the infinite source of inspiration. His passion for research has always inspired me. I also thank my POS committee members, Dr. Rana Biswas, Dr. Sumit Chaudhary, Dr. Ruth Shinar and Dr. Mani Mina for their continuous and kind support. Various suggestions from them helped me sail through this endeavor.

A very special thanks to Max Noack. He taught me so many things related to experimental setup and also more importantly, the importance of patience. Thanks to Dr. Wai Leung for helping with various experimental setups, also to Andrew Kitahara for help with LabVIEW programming in the degradation chambers.

I consider myself very lucky to have to have had excellent mentors in Dr. Joydeep Bhattacharya, Dr. Balaji Ganapthy, Dr. Mehran Samiee and Dr. Ranjith Kottokkaran. Technical, non-technical discussions with them, their advice on various issues has helped me to become better researcher and person.

Special thanks to Liang Zhang for providing me the devices for stability studies and also technical inputs, also to Dr. Satyapal Nehra, Istiaque Hossain for help with device fabrication. Thanks to Dr. Siva Konduri, Dr. Shantan Kajjam, Dr. Rakesh Mahadevpuram, Dr. Sambit Pattnaik, Dr. Moniem Elshobaki, Fadzai Fungura, Dr. Dipak Paramanik, Satvik Shah, Hisham Abbas, Sabrina Stark, Akshit Peer, Tanvir Muntasir, Mohamed El-Henaway, Dr. Mahendra Dhaka, Behrang Bagheri, Harsh Gaonkar and all other former/ current MRC associates for their support during this work. Administrative support by Nancy, Rita and Marian was also very useful.

I would also to thank my friends Piyush, Anup, Ravi, Ashish, Sudhanshu, Ganesh, Chetan, Santosh, Srijita, Danqing, for making my stay in Ames a happy one. Support from my long distance friends; Tanuj S., Tanuj G., Vishal, Bharat, Aniket, Rohan, Devendra, Nayan, Indranil and others was also very helpful in these years.

Finally, my family; my mother Dr. Jyoti Varudkar, my father Hemanta Joshi, my brother Pushkar Joshi and my wife Gauri Ramasubramanian. No words can match their sacrifice and support. It is only because of their teachings and guidance, that I could achieve what I have. I would also like to thank my grandparents, my extended family and friends, who have played a significant role in shaping me into what I am today.

ABSTRACT

Global climate change and increasing energy demands have led to a greater focus on cheaper photovoltaic energy solutions. Perovskite solar cells and organic solar cells have emerged as promising technologies for alternative cheaper photovoltaics.

Perovskite solar cells have shown unprecedentedly rapid improvement in power conversion efficiency, from 3% in 2009 to more than 21% today. High absorption coefficient, long diffusion lengths, low exciton binding energy, low defect density and easy of fabrication has made perovskites near ideal material for economical and efficient photovoltaics.

However, stability of perovskites, and organic solar cells, especially photostability is still not well understood. In this work, we study the photostability of organic solar cells and of perovskite solar cells.

In the first part of this work, effect of modification of sidechain of polymer in high efficiency organic solar cell was investigated. It was observed that PTB7-Th polymer with alkyl thiophene sidechain degrades more than PTB7 with alkoxy sidechain.

Next, we study the stability of perovskite cells. When the perovskite cells are exposed to light under open circuit condition, very intriguing results were observed. I_{sc} decreased during exposure, whereas surprisingly, V_{oc} of the device increased. Even more intriguing phenomena were observed after exposure. After exposure, I_{sc} of the device recovered very quickly whereas increased V_{oc} of the device decreased to a value lower than initial value after around 30 minutes of exposure. V_{oc} of the device then slowly recovered to initial value. Capacitance, dark IV of the device also showed intriguing but similar changes.

We explain all these observations using a model based on ionic migration. We consider intrinsic thermally generated ions and generation of more ions during light exposure and then recombination of these ions when light exposure is turned off. This model can be used to explain all anomalous observation during light exposure and recovery after exposure. Few more experiments were done, effect of intensity on degradation, effect of temperature on after degradation recovery, which confirm the model presented. Experiment on devices with different grain size suggest that ion migration is grain boundary assisted phenomena, such that for higher grain size films, degradation is slower.

CHAPTER 1

INTRODUCTION

1.1: Why Solar Photovoltaics

It all began when the human race learnt how to start and maintain fire, the first energy source (other than food energy) which we could harness. Since then, development of the human race can easily be correlated with the amount of energy utilized. Energy utilization or generation in simple terms is dependent on how many energy sources we can harness, potential of these energy sources, and the efficiency of conversion of these energy sources to a usable form.

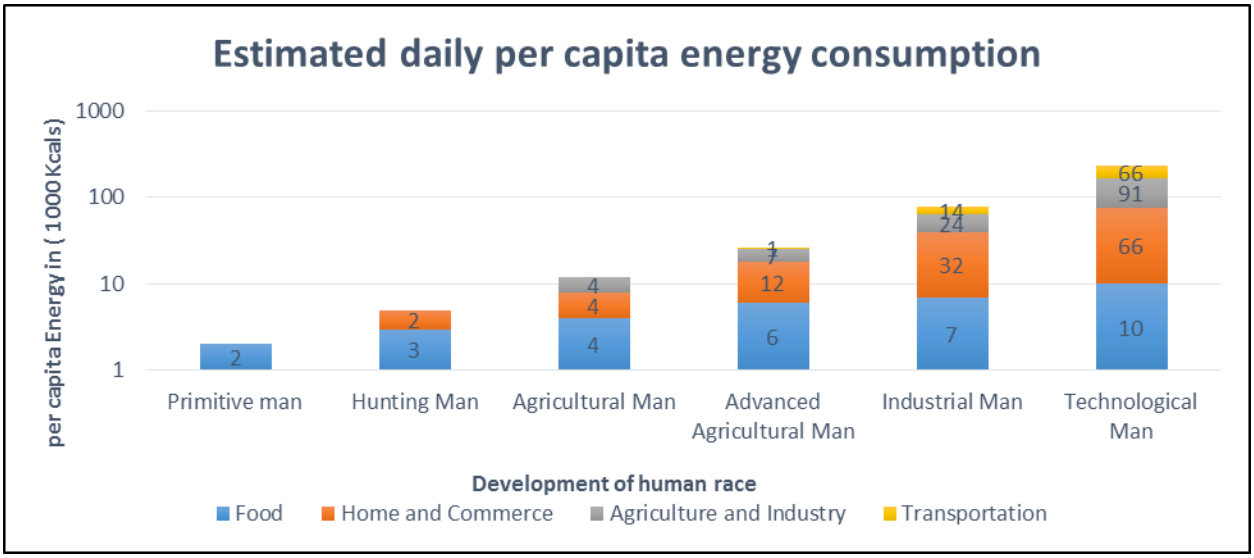

Fig 1.1: Estimated daily per capita energy consumption of human at various developmental stages [1].

From the dawn of mankind till as late as 1800s, wood was the predominant energy source utilized. Main reason for wood's domination as an energy source was local, easy and abundant availability. Wood, if considered is also a renewable energy source and thus a small usage of wood did not create any big problems for the human race. However, with industrialization, the energy requirement started to increase and coal got more and more prominent for its higher energy density

and ease of use. Even today, coal is the main energy source for thermal electricity generation plants, which dominate all energy generation. Discovery of oil and gas fields and improvements in extraction technologies in 19th and 20th centuries made oil the main source of vehicular transport and gas the main source for electricity generation, especially in North America and Europe. Fig. 1.2 shows how different fuels were utilized in last two centuries.

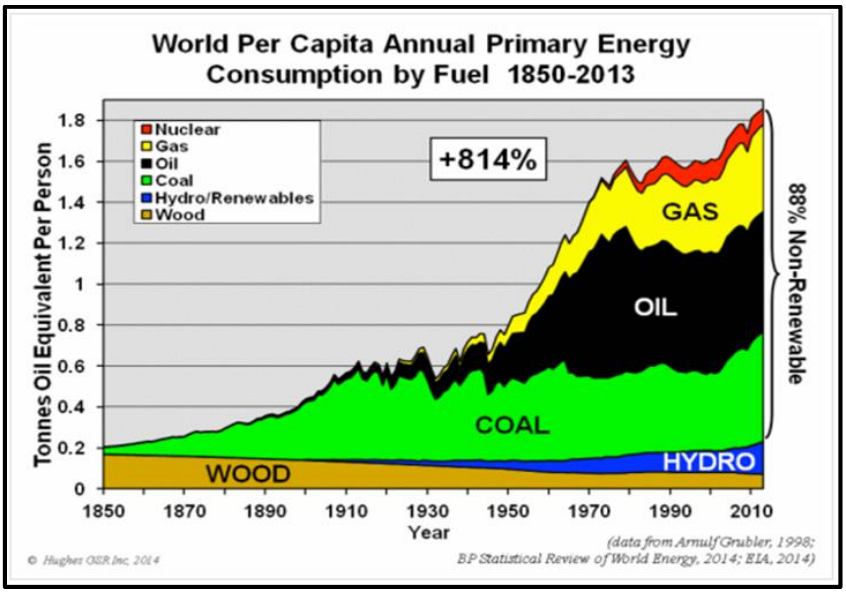

Fig.1.2: World per capita annual primary energy consumption by fuel from 1850 – 1923 [2].

The source of energy in wood, coal, oil, and gas is a hydrocarbon, which is essentially an organic compound made simply of carbon and hydrogen. When hydrocarbons are combusted, they react with oxygen in an exothermic reaction and as a result release energy.

However, one of the products of the reaction is carbon dioxide. Carbon dioxide is a green-house gas. Greenhouse gases absorb and re-emit the infrared radiation which results in an increase in the temperature. The temperature of the earth would have been 15 degrees lower if not for greenhouse gases [3]. Excess greenhouse gas however would result in a further increase in the earth's temperature. CO_2 concentration in the atmosphere has increased from 300 ppm to more than 400 ppm in the last 50 years and there has been an increase of ~0.75^0C in global average

temperature over this period [4]. After initial disagreements, the Intergovernmental Panel on Climate Control in 2007 published a data correlating these two events. The data suggests that CO_2 is the most significant driver in the global temperature rise (Fig 1.3). This global warming and thus the climate change can result and in some parts has already resulted in, melting of polar ice, rise in sea levels, glacier retreat, expansion of deserts, and extreme weather. Basically it would have serious harmful effects on human civilization in the long term. To avoid this dangerous future, at the United Nations conference on climate change in 2015, an agreement was negotiated that 196 countries in the world would set a goal to limit the increase in temperature by 2100 (from 1850) to 2^0C [6]. Achieving the 2^0C limit would require reducing CO_2 emissions to ~50% by around 2050 [8].

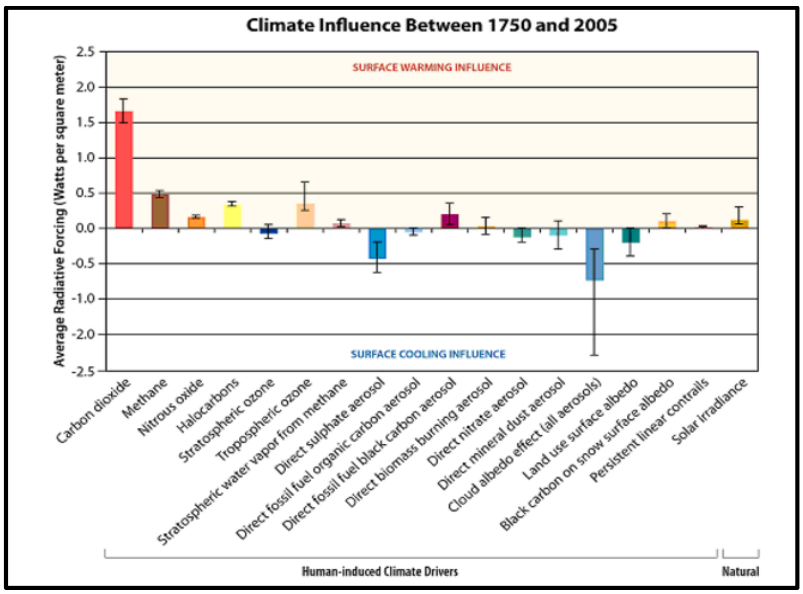

Fig.1.3: Effect of various gases on earth surface warming [5].

Apart from hydrocarbon-based energy sources, other significant energy sources that human has learnt to tap efficiently are hydro energy, solar energy, wind energy, tidal energy, nuclear energy and geothermal energy. Fig. 1.4 shows evolutions for CO_2 emission or carbon footprint for various technologies.

Geothermal energy is a possible source of relatively clean and sustainable source of energy, coming out from radioactivity in earth's core. However harnessing this energy is not easy as drilling is very expensive and otherwise we are left only with few locations on the tectonic plate boundaries. Nuclear energy is a promising energy source and many countries in the world have been utilizing nuclear energy effectively, however it is expensive, non-renewable and also it can be extremely hazardous as seen in some of accidents like Chernobyl and Fukushima. Wind and tidal energy have enormous potential, and are very clean and sustainable. However they have huge fluctuations and have very high installation costs. Hydro power is a green, reliable, safe and also flexible energy source, however much of the suitable reservoirs have already been used and it might have environmental consequences.

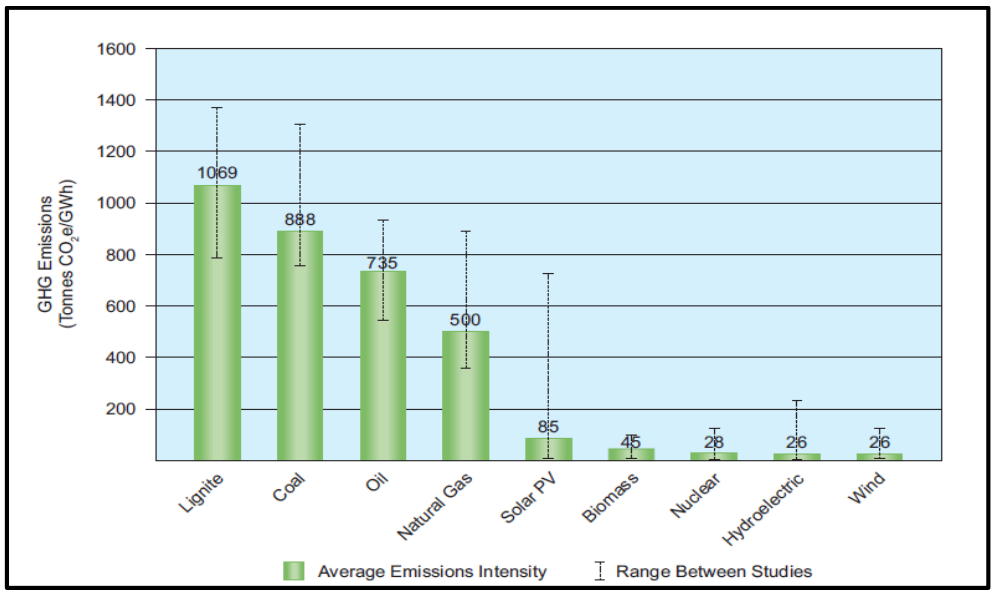

Fig.1.4: CO_2 gas emissions per GWh energy generation from different sources [7].

Two of the most prominent tapping methods for solar energy are *Solar thermal* and *solar photovoltaic*. In solar thermal, solar energy is converted to heat which is then used to run a heat engine producing electricity. Since heat can be stored easily, solar thermal generator can be run even at night, making solar thermal a very attractive large scale generation method. In solar

photovoltaics (PV), solar energy is directly converted to electricity. Solar PV is the most direct conversion of most abundant energy source to the most useful energy form. Solar PV does not need a big plant and can be very effective source for distributed power generation. Solar PV can be run only in daylight hours, but that is also the time of peak load and thus integration of solar PV in the grid can be very useful.

As mentioned all of these alternative energy sources have some disadvantages and some advantages and best solution would be to use all of these energy sources in their advantageous areas.

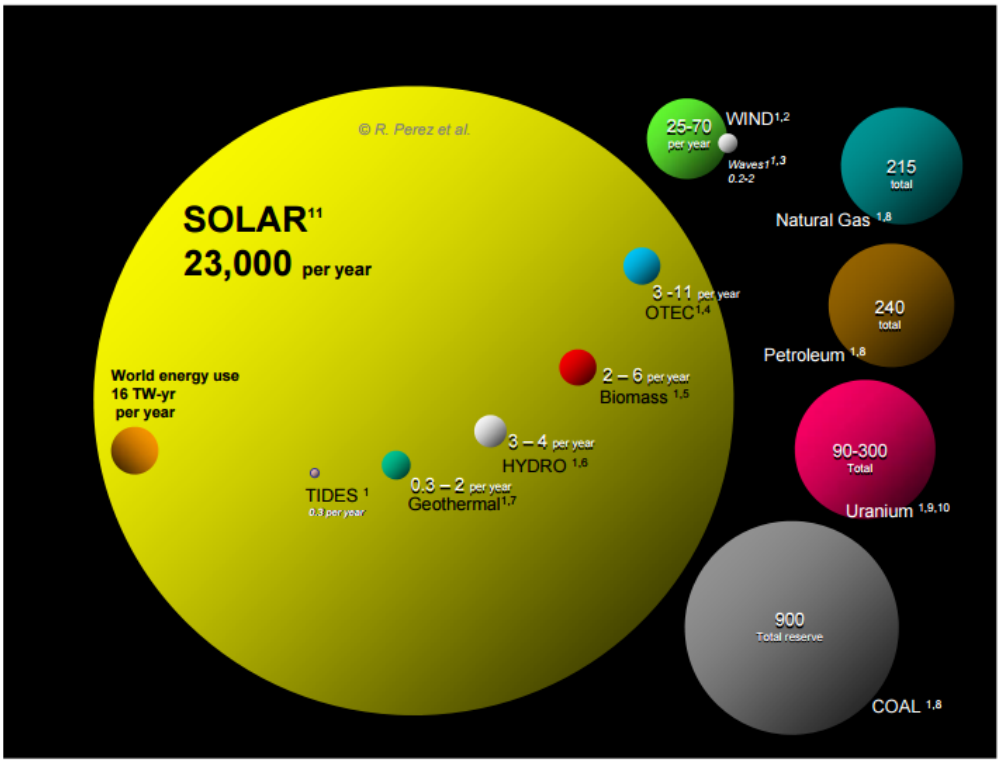

Fig. 1.5: Potential of various energy sources and global annual energy consumption [10].

Apart from climate change reasons, coal, oil, gas and also nuclear are non-renewable energy sources or their rate of generation is too small compared to their rate of consumption. Under the assumption that the population of mankind does not change drastically and it consumes energy at the current level, the fossil fuel reserves will be exhausted within 320 years and the nuclear

energy within 260 years [9]. Fig. 1.5 beautifully represents how solar energy if tapped efficiently can be a sustainable solution.

The International Energy Agency in its roadmap for solar photovoltaic envisions 16% of total electricity generation coming from solar photovoltaic to achieve 2^0C scenario in high renewable energy scenario and 10% in 2^0C in high nuclear, carbon capture technique scenario [8].

1.2: Status of Solar Photovoltaics

Photovoltaic effect was first demonstrated in 1839 in silver halides [11]. By end of 19th century, photovoltaic effect was also observed in Selenium and nearly 1% all-solid thin film solar cell was made [12]. In the first half of 20th century, photovoltaic effects were observed in Copper-Copper Oxide junction [13]. During the same time, in the initial works of Silicon, photovoltaic effect was observed in the naturally grown junctions in silicon ingots [14].

The first modern solar photovoltaic cell was made by Bell Labs in 1954 with the help of advancements in silicon technology. This 6% cell helped in understanding the basic working mechanism and predicting the ideal material. Soon Gallium Arsenide and Cadmium Telluride cells were developed for solar cell applications. First real push for solar cells came in late 1950s and 60s for space applications. Solar cells were an ideal source for sustainable operation of satellites. Satellites needed high efficiency cells and cost was not a big problem, and thus, very little progress was done on terrestrial or daily use photovoltaics. It was mainly used in devices which needed small amounts of power and which were difficult to connect to grid electricity. It took the 70s oil crisis to give a second push to solar cell research, where efforts were put to reduce the price of the solar cells. Thin film technologies were developed to reduce the amount of material and hence cost of solar cells, especially in amorphous Silicon, Cadmium Telluride and Copper Indium Selenide.

Multicrystalline Silicon was developed in this era reducing costs in silicon. In the late 80s and early 90s, a third generation of solar cells were developed with potentially even cheaper technologies like dye sensitized solar cells, organic solar cells and quantum dot solar cells. With the increasing awareness of climate change, a third and the most real push for solar cells came in first decade of 21st century. This spurred a rapid installation of solar cells for last 10 years. Recently perovskites were found to be a promising material for photovoltaic application. Chart by National renewable energy laboratory (Fig. 1.6) gives a good idea of the development of various technologies in last 40 years.

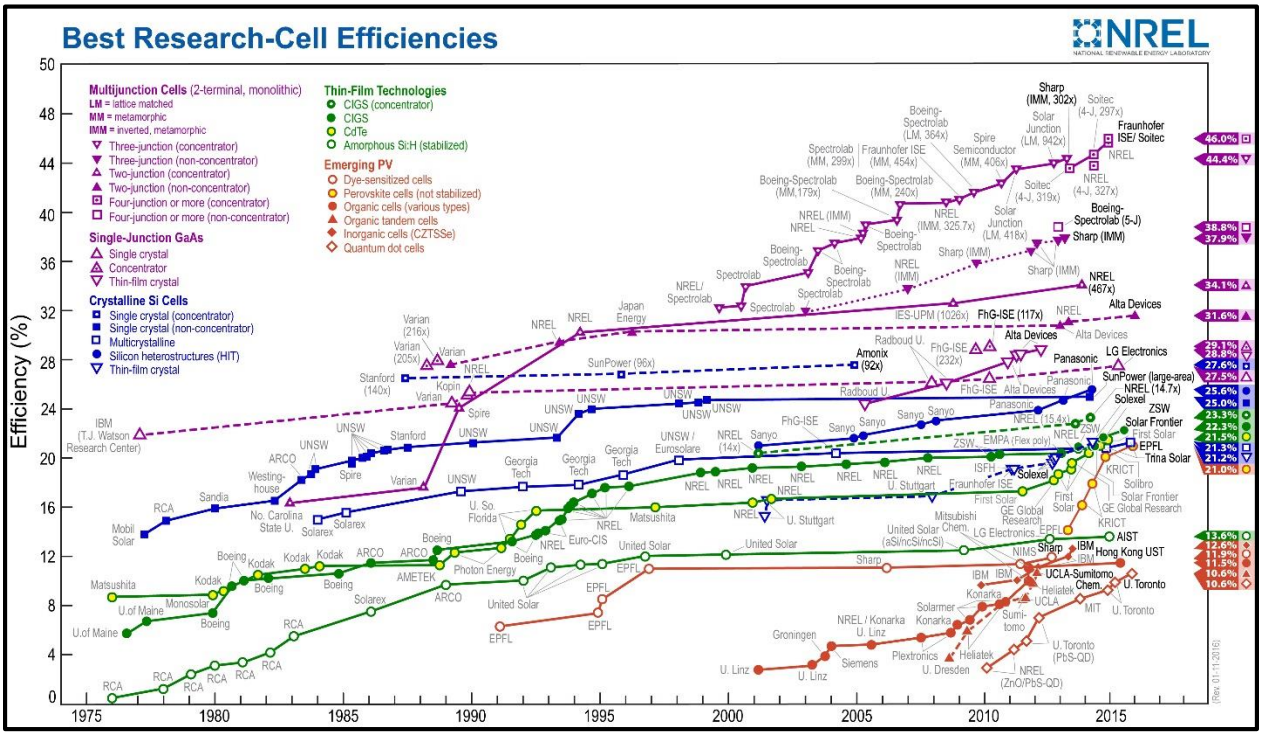

Fig. 1.6: Evolution solar cell efficiencies over time for various technologies [16].

Solar cells, like transistors, have also shown an exponential decrease in price/watt. Just like Moore's law, Sunpower's founder Swanson has observed that photovoltaic module prices tend to drop by 20% with doubling of shipping volume. At present costs halve every 10 years. Recent

report from Fraunhaufer Institute of Solar Energy suggests that payback time has already come down 1-2 years in Europe which receives much less sunlight than equator [20].

The current market share of various technologies in overall solar cell installations is shown in the Fig. 1.7. Solar PV electricity generation is still mostly dominated by Crystalline Silicon. Cadmium Telluride and Copper Indium Gallium Selenide (marked as other thin films in Fig. 1.7) however are making rapid inroads in solar PV markets [19].

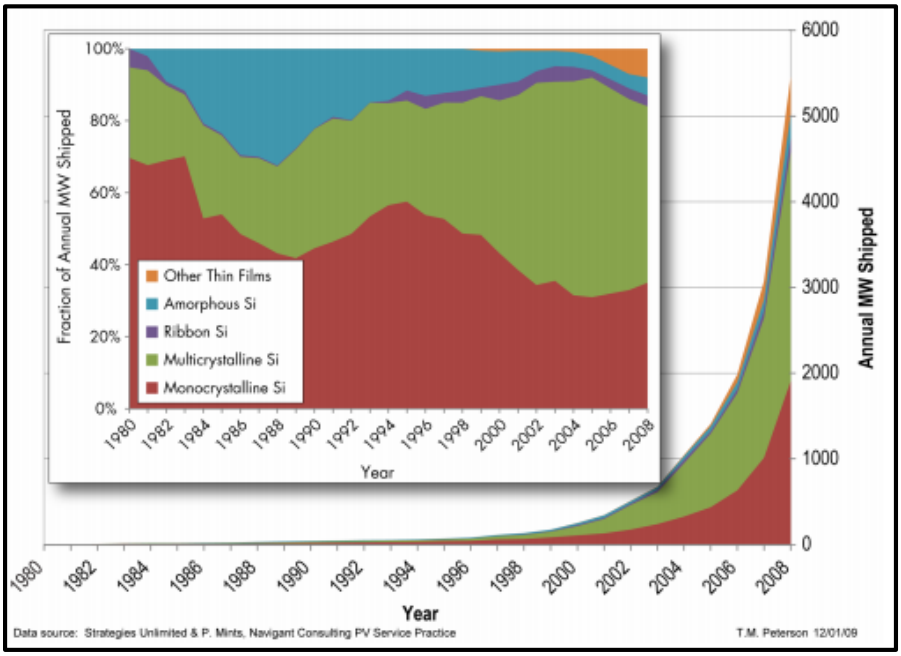

Fig.1.7: Share of various solar cell technologies in overall solar cell shipments over time [19].

In a 2015 article [21], You's group compares energy payback time for various solar cell technologies in southern Europe. It can be seen that third generation technologies like organic solar cells and perovskite solar cells have a huge potential to reduce the cost of energy generation by solar cells. It can be noted that unlike other technologies which are now mostly saturated, organic and perovskite technologies are still in research and are showing huge improvements every year and thus price are expected to decrease even further.

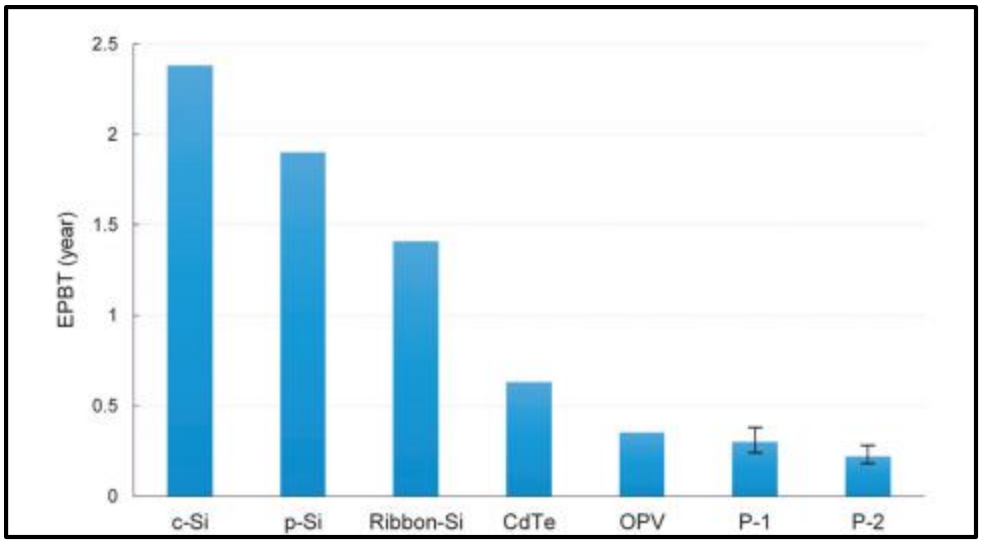

Fig. 1.8: Energy payback time for various solar cell technologies for southern Europe. P-1 and P-2 are for two different architectures of perovskite solar cells [21].

Thorough understanding of silicon from microelectronics industry has helped in fabricating high efficiency solar cells from crystalline Si. However, silicon is not an ideal material for photovoltaic applications and thus very thick layers of silicon are required resulting in higher costs. Multicrystalline Si can be made using easier and thus cheaper techniques, however overall efficiencies are lower in multicrystalline Si because of the increased defects. Amorphous Si is even cheaper than multi-crystalline Si, however it has further lower efficiency and lower lifecycle. Cadmium telluride and copper indium gallium selenide have bandgaps that are close to ideal bandgap for photovoltaic technologies, and high efficiency cells have been made from them at much lower cost. However, the materials used in these technologies are hazardous/toxic and also are rare in earth. Organic solar cells and perovskite solar cells can be fabricated very easily, making them very cheap. In addition, fabrication can also be done on flexible substrates. High efficiencies have been achieved, especially in perovskite solar cells, and can potentially revolutionize the entire solar cell market. However, there are still some serious concerns about the stability of these technologies and in this work; we would try to understand the same.

1.3: Organic Solar Cells

Photovoltage was first observed in organic molecules in late 1950s [22]. These devices were made by sandwiching organic pigments in two metals, and thus forming a Schottky barrier solar cell. A 0.7% device was made in 1970s [23]. The next breakthrough was using a bi-layer structure, where two organic layers were sandwiched between metals, one having high electron mobility and other high hole mobility [24]. Improvements in conjugated polymers [25-26] and observation of electron transport in C-60 [27] lead to fabrication of organic devices using polymers and C-60. In the 90s critical ideas like co-evaporation of p-type and n-type organic molecules [28] and the bulk-heterojunction for soluble molecules/polymers/C-60 modifications [29] were thought of. These ideas and the development of polymers and soluble C-60s lead to the exponential growth in the efficiency of organic solar cells in the past decade. Efficiencies of more than 10% have already been achieved in single junction organic solar cells [30]. Multijunction solar cells have also been used with organic solar cells with efficiencies higher than 12% [31].

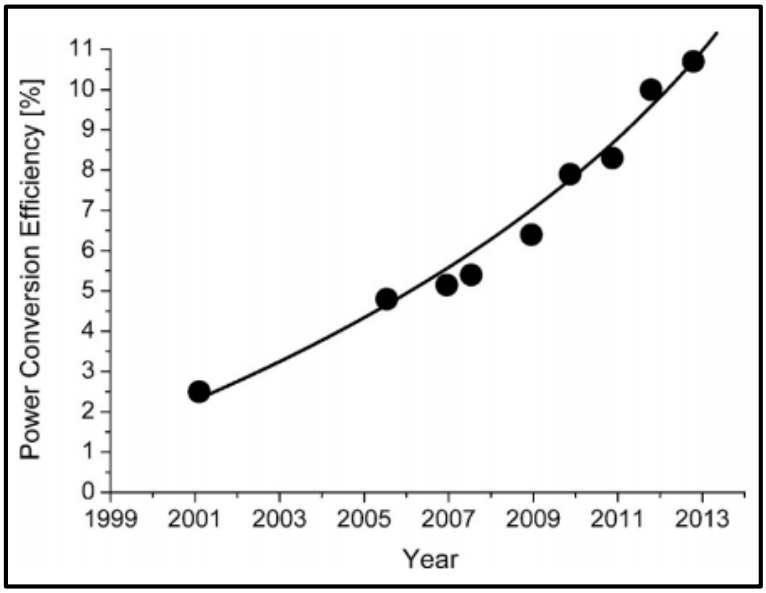

Fig. 1.9: Evolution of organic solar cell efficiencies in last decade [36].

The sp^2 hybridization in carbon atoms is responsible for the semiconducting properties of the organic molecules/polymers [32]. The π-electrons on sp^2 hybridized carbon are delocalized in nature which result in electronic polarizability. The main disadvantages of organic materials are high exciton binding energy resulting in the formation of bound excitons and lower charge carrier mobilities. However, organic materials generally have high absorption coefficients (~10^{-5} cm^{-1}), which helps in balancing the mobilities as lower thicknesses are enough to absorb most of the light. Typical thicknesses of organic photoactive layers are of the order of 100 nm. Built-in electric field at bulk-heterojunction has been used to separate excitons. Generally organic materials have high bandgaps (~2 eV) which is not very ideal for photovoltaic applications, however easy tailoring in organic materials has been used to synthesis lower bandgap polymers [33-35].

Main advantages of organic solar cells are potentially low cost materials and easy processing. The easy, low temperature processing can also be extended to roll-to-roll processing, reducing the costs even further. The possibility of tailoring the functional materials in organics leads to the possibility of synthesizing better suited materials and thus getting even higher efficiencies. However, stability is a major concern which needs to be solved before successful commercialization. Degradation in organic materials is still not completely understood [37]. Our group and Street group have proposed a hypothesis for the degradation in the organic materials. According to this hypothesis, increased mid-gap defects in the polymer because of bond breaking at the sidechains of the polymers in organic molecules decreases the efficiency of the device [38, 39]. A possible solution to the stability problem is to modify the sidechain of the polymer [40]. The effect of sidechain modification in organic solar cells is presented in Chapter 4 of this dissertation.

1.4: Perovskite Solar Cells

Perovskite is a specific crystal structure ABX_3, where A, B are cations with valency +1, +2 respectively whereas X is an anion, mostly oxygen or halogen. Fig. 1.10 shows such a crystal structure, where larger cation A occupies cubo-octahedral site shared with twelve 12 X anions, whereas smaller cation B is at octahedral site shared with 6 X anions. Oxide perovskites are intensely studied for past 50 years for their ferroelectricity and superconductivity.

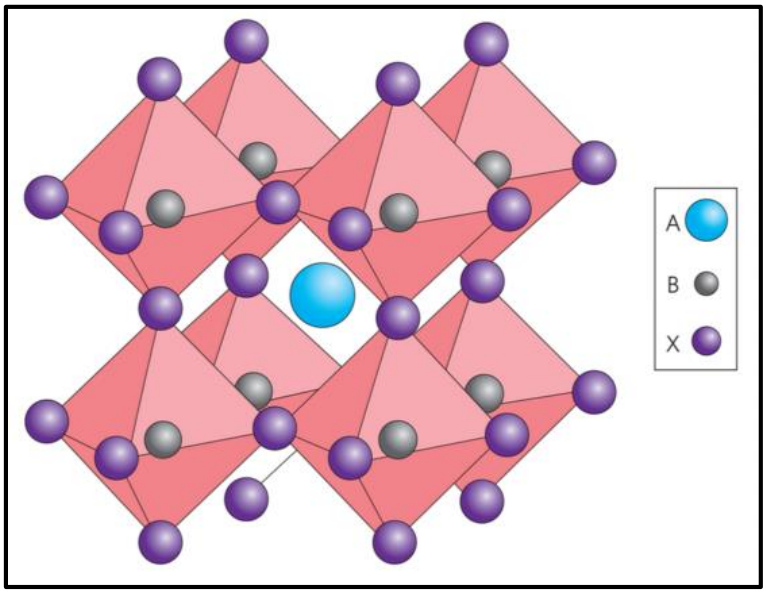

Fig. 1.10: ABX_3 perovskite crystal structure [41].

Miyasaka group first showed the photovoltaic applications of halide perovskites. In 2006 and 2009 they utilized methylammonium lead bromide ($CH_3NH_3PbBr_3$) and methylammonium lead iodide ($CH_3NH_3PbI_3$) perovskites for the sensitization in dye sensitized solar cell (DSSC) structure and achieved efficiencies of 2.8% [42] and 3.6% [43] respectively. In 2011, Park group achieved 6.5% efficiency with $CH_3NH_3PbI_3$ used in extremely thin absorber (ETA) type dye sensitized solar cell structure [44]. Fig. 1.11 represents the development of structure of perovskite solar cells. In 2012, Park group used solid electrolyte to improve the corrosion of perovskite from

electrolyte by using Spiro-OMeTAD and achieved 9.5% efficiency [45]. Non-sensitized type perovskite solar cell was first proposed by Snaith group where 10.9% efficiency was demonstrated using mixed halide $CH_3NH_3PbI_{3-x}Cl_x$ perovskite [46]. Since then rapid progress has been reported in perovskite solar cells made in non-sensitized types. Even though majority of the devices are still made in mesoporous structure, ambipolar transport in perovskites also allows for planar devices.

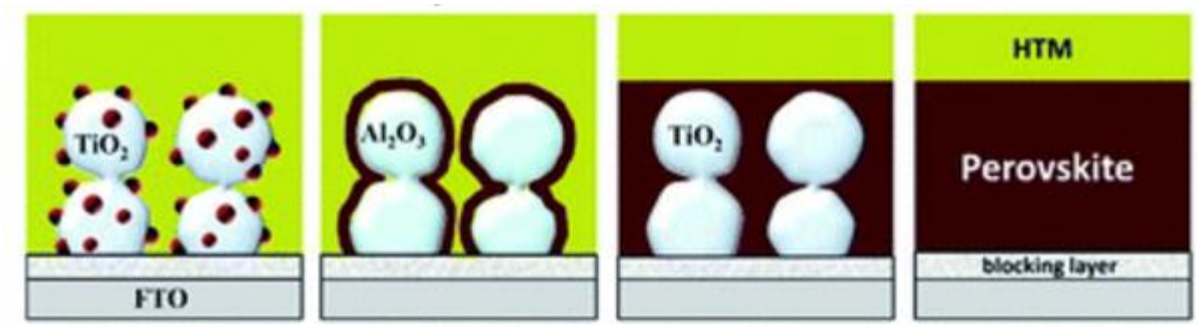

Fig. 1.11: Structural progress in perovskite solar cells. From left to right, perovskite solar cells started with DSSC type structure, ETA type devices were made in 2011. In 2012 mesoporous non-sensitized solid state devices were made. Perovskite solar cells can also be made in planar type structure. Figure from [47].

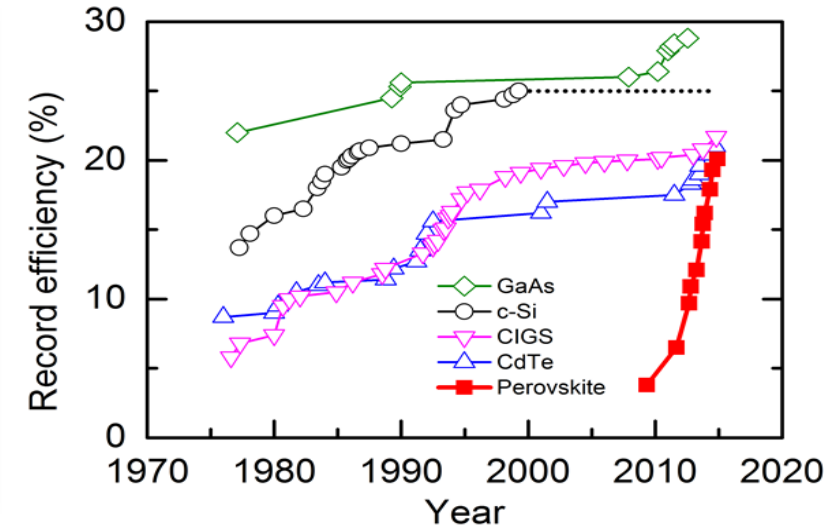

Fig. 1.12: Evolution of power conversion efficiency in perovskite solar cells compared to other technologies [53].

In 2013, 15% cells were reported by Gratzel group [48] and Snaith group [49]. Yang group reported 19.3% efficient cells in 2014 [50]. In 2015, Seok group reported efficiencies of 20.2% by

mixing FAI and MABr instead of MAI with PbI_2 to make the perovskite layer [51]. In 2016, so far, efficiency of 21.1% has been reported by Gratzel group by adding Cs to make triple cation mixture of Cs, FA and MA [52]. Fig. 1.12 represents the rapid evolution of power conversion efficiencies in perovskite technology when compared to matured technologies.

Perovskite, is direct bandgap semiconductor with bandgap of around 1.6 eV [54], which can be tuned quite easily. As will be discussed in chapter 2, direct bandgap helps in absorption and as it can be seen from Fig. 1.13, absorption coefficient of perovskite is quite high.

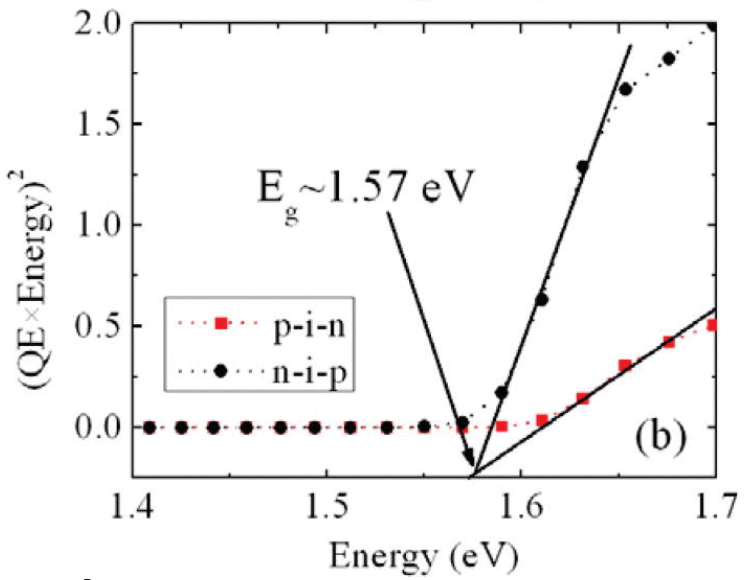

Fig. 1.13: (QE x Energy)^2 vs Energy plot for perovskite suggesting a direct bandgap of 1.57 eV [54].

Fig. 1.13 shows absorption coefficient of $CH_3NH_3PbI_{3-x}Br_x$ perovskite for different values of x. It can be seen that absorption coefficient of perovskite is quite high in the range of 10^4-10^5 /cm^{-1}. Suggesting a penetration depth in the range of 100 nm-1 μm. Thus a thin layer of perovskite can be used to absorb all photons, reducing the material cost and hence the cost of the perovskite technology.

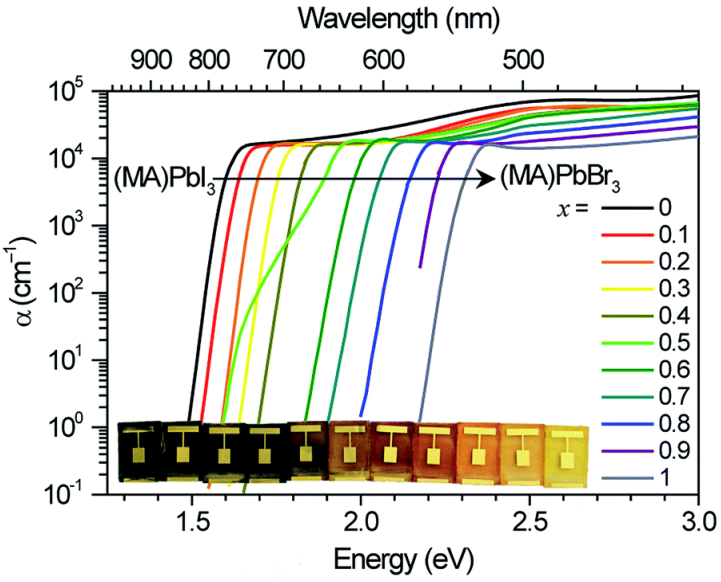

Fig. 1.14: Absorption coefficient of perovskite at different proportion ratio of I and Br as measured by Hoke et al. [55].

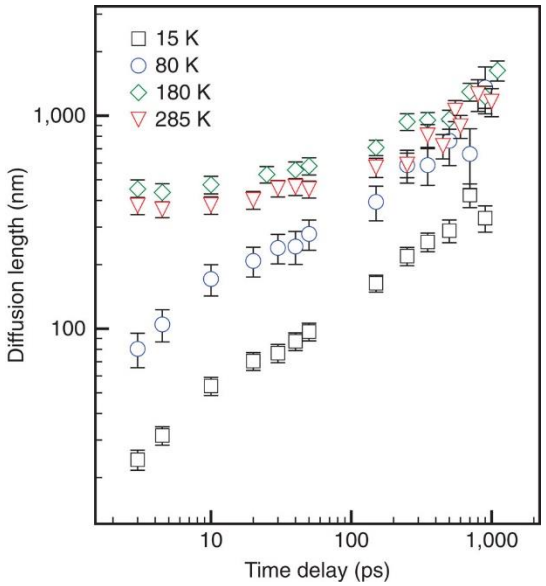

Fig. 1.15: Diffusion length in perovskite thin film at various temperatures, as measured by La-o-vorakiat et al. [60].

Various groups have shown high values for free charge carrier mobilities for perovskites. Stoumpos et al. calculated mobility in perovskite to be 66 cm^2/Vs [56], whereas Leijtens et al. [57] reported mobility in the range of 20 cm^2/Vs. High career mobility, coupled with high career lifetime [58], leads to high diffusion lengths. Diffusion lengths in the order of 100 nm -1 μm have

been reported by multiple groups in perovskite thin films [58, 59, 60]. Higher diffusion length reduces recombination losses in the solar cell and thus a thick photovoltaic active layer can be used to absorb more photons. It has been also been shown that perovskite active layer has low defects [54], further reducing recombination losses in the perovskite solar cell.

Another important parameter for photovoltaic application is the exciton binding energy. Perovskites have very high dielectric constant and giving very low exciton binding energies [61, 62]. Thus thermal energy at room temperature is enough to form free electron-hole pair reducing recombination losses at exciton level.

Perovskite deposition is also very easy and cost-effective. Perovskite is formed just by mixture of PbI_2 and MAI at room temperature or slightly elevated temperatures ($<100^0$C). Multiple ways can be used to deposit perovskite thin film. PbI_2 and MAI either be mixed before and then deposited to form perovskite or they can be separately deposited on top of each other on the substrate and then thermal diffusion can be used to make perovskite. PbI_2 and MAI can also be either used in liquid solution phase or in vapor phase. This gives multiple easy ways to deposit perovskite. Recent work in our group and some other groups has shown that various precursors of Pb (e.g. $Pb(NO_3)_2$, $Pb(SCN)_2$, $Pb(OAc)_2$) can be used with higher molar ratio of MAI to form same CH_3NH_3MAI perovskite[63, 64]. Mixed cation perovskites have also been formed giving higher efficiency and stability [52].

Bandgap of perovskite can be easily tuned, which can be of great use, especially in white LED or even in tandem photovoltaic applications. Necessary conditions to make a perovskite for A, B and X are given by tolerance factor (should be between 0.81 and 1.1) and octahedral factor (should be between 0.44 and 0.89) [41, 65]. Fig. 1.13 shows different elements that can form perovskite with two different cations, MAI and FAI. Apart from these different perovskites,

cations and anions in the perovskite can also be mixed in various ratio thus giving a big control for the tuning of the bandgap and also other properties of the perovskite [52, 66].

Tolerance Factor

MA	Pb	Sn	Ge	Cd	Zn
I	0.83	0.86	0.97	0.90	0.96
Cl	0.84	0.87	0.99	0.91	0.98
Br	0.85	0.88	1.00	0.92	1.00
F	0.88	0.91	1.07	0.97	1.07

FA	Pb	Sn	Ge	Cd	Zn
I	0.86-0.92	0.88-0.94	0.99-1.06	0.92-0.99	0.99-1.06
Cl	0.87-0.93	0.89-0.96	1.01-1.09	0.94-1.01	1.01-1.09
Br	0.87-0.95	0.90-0.97	1.03-1.12	0.95-1.03	1.03-1.11
F	0.91-0.99	0.94-1.03	1.11-1.21	1.00-1.09	1.11-1.21

Octahedral Factor (0.44-0.90)

	Pb	Sn	Ge	Cd	Zn
I	0.54	0.50	0.33	0.43	0.34
Cl	0.61	0.56	0.37	0.48	0.38
Br	0.66	0.61	0.40	0.52	0.41
F	0.89	0.83	0.55	0.71	0.56

Fig. 1.16: Tolerance factor and octahedral factor calculations for different elements in perovskite.

Main disadvantages of perovskite solar cell is the presence of lead. Perovskite if disintegrated can turn to PbI_2 which is water soluble and would be a big environmental hazard. Fig. 1.13 shows the possibilities of other metals that can be used to make perovskite solar cell and research is going on to make efficient non-lead perovskite solar cell [67-69].

Major unexplored area for perovskite solar cells is stability. Perovskite material rapidly degrades in presence of moisture [70]. Recent reports have also shown degradation of perovskites in oxygen [71]. Encapsulation and over-layers on perovskite film have shown to stop partially or fully the degradation caused by air ambience [72, 73].

A fundamental with perovskite is however the intrinsic degradation in perovskites under light. Unfortunately very little work has been done on light-induced degradation in perovskite solar cells. Thus we decided to investigate the light-induced degradation in perovskites. Findings of our work on perovskite photostability are reported in Chapter 5.

1.5: Outline of this report

In first chapter, importance of solar photovoltaics and current status of various solar photovoltaic technologies has been discussed. We observed that organic solar cells and perovskite solar cells have commercial potential, however their photo-stability needs more research. In second chapter, I would go briefly over basic device physics of solar cells. Working principle of solar cells is explained mostly using classical theory. In third chapter, methods of fabrication and characterization has been discussed in detail. From fourth chapter, I would start discussing results of this work. In fourth chapter, effect of sidechain modification in high efficiency polymer on the photostability of the organic solar cell has been discussed. In fifth chapter, photostability of perovskite solar cell has been discussed. Initially anomalous behavior in perovskites has been explained using ionic motion model and then the stability of perovskite solar cell has been explained. In this work, a p-i-n NiO_x/perovskite/PCBM structure was used.

1.6: References

1. Cook E., *The flow of energy in an industrial society*, Scientific American 1971. https://www.wou.edu/las/physci/GS361/electricity%20generation/HistoricalPerspectives.htm

2. Heinberg R., *Our Renewable Future, Simplicity Institute Report 2015* http://simplicityinstitute.org/wp-content/uploads/2011/04/Our-Renewable-Future-Simplicity-Institute.pdf

3. Karl T.R., and K.E. Trenberth, *Modern global climate change.* Science **302** (5651) 1719–23 (2003).

4. www.climate.nasa.gov

5. *International Panel on Climate Change 2007 WGI report*, https://www.ipcc.ch/

6. *Conference of parties 21*, www.cop21paris.org/

7. World Nuclear Agency Report 2011, *Comparison of lifecycle greenhouse gas emissions of various electricity generation sources*

8. IEA roadmap to Solar Photovoltaics https://www.iea.org/publications/freepublications/publication/TechnologyRoadmapSolarPhotovoltaicEnergy_2014edition.pdf

9. Zemen M., *Chapter 1: Introduction to Photovoltaic Solar Energy in Solar Cells, TU Delft open course*

10. Perez R., and M. Perez, *A fundamental look at energy reserves for the planet* http://www.asrc.albany.edu/people/faculty/perez/Kit/pdf/a-fundamental-look-at%20the-planetary-energy-reserves.pdf

11. Becquerel A.E., *Recherches sur les effets de la radiation chimique de la lumiere solaire au moyen des courants electriques*. Comptes Rendus de L´Academie des Sciences 1839. 9:145-149.

12. Fritts C.E., *On a new form of selenium photocell.* American J. of Science. 1883, ;26: 465.

13. Grondahl L.O., *The copper-cuprous-oxide rectifier and photoelectric cell*. Review of Modern Physics. 5:141 (1933).

14. Ohl R.S., *Light-sensitive electric device*. U.S. Patent 1941. 2:402, 602.

15. Green M. A., *Photovoltaics: coming of age.* 21st IEEE Photovoltaic Specialists Conference 1900, 1-8

16. http://www.nrel.gov/ncpv/images/efficiency_chart.jpg

17. International Technology Roadmap for Photovoltaics http://www.itrpv.net/Reports/Downloads/2015/

18. https://en.wikipedia.org/wiki/Swanson%27s_law#/media/File:Swansons-law.png

19. EPRI white paper on Solar Photovoltaics: Status, Costs, Trends 2009. http://www.epri.com/

20. Fraunhaufer Report on Photovoltaics 2015 https://www.ise.fraunhofer.de/en

21. Gong J., Darlingbc S.B., and F. You, *Perovskite photovoltaics: life-cycle assessment of energy and environmental impacts,* Energy Environ. Sci**.,** 2015, 8, 1953.

22. Kallmann H. and M. Silver., *Symposium on Electrical Conductivity in Organic Solids,* Wiley Interscience, New York, pp.1961. 39, 69, 291.

23. Morel D.L. et al. *High-efficiency organic solar cells*. Appl. Phys. Lett. 1978, **32,** 495.

24. Tang C.W., *Two-layer organic photovoltaic cell.* Appl. Phys. Lett. 1986. **48,** 183.

25. Marks R.N., Halls J.J.M., Bradley D.D.C., Friend R.H., and A.B. Holmes, *The photovoltaic response in poly(p-phenylene vinylene) thin-film devices*. J. Phys.: Condens. Matter. 1994. 6, 1379.

26. Yu G., Zhang C., and A.J. Heeger: *Dual-function semiconducting polymer devices: Light-emitting and photodetecting diodes*. Appl. Phys. Lett. 1994. 64, 1540.

27. Sariciftci N.S., Smilowitz L., Heeger A.J., and F. Wudl, *Photoinduced electron transfer from a conducting polymer to buckminsterfullerene*. Science 1992. 258, 1474.

28. Hiramoto M., Fujiwara H., and M. Yokoyama, *Three-layered organic solar cell with a photoactive interlayer of codeposited pigments*. Appl. Phys. Lett. 1991. 58, 1062.

29. Yu G., Gao J., Hummelen J.C., Wudl F., and A.J. Heeger: *Polymer photovoltaic cells: Enhanced efficiencies via a network of internal donor-acceptor heterojunctions*. Science 270, 1789 (1995).

30. Hu, H., et al., *Terthiophene-Based D–A Polymer with an Asymmetric Arrangement of Alkyl Chains That Enables Efficient Polymer Solar Cells.* Journal of the American Chemical Society, 2015. **137**(44): p. 14149-14157.

31. Heliatek press release, accessed on April 4th 2016, http://www.heliatek.com/en/press/press-releases/details/heliatek-sets-new-organic-photovoltaic-world-record-efficiency-of-13-2

32. Pope, M. and C.E. Swenberg, *Electronic Processes in Organic Crystals and Polymers* 2nd edn. (Oxford Univ., 1999).

33. Wohrle D., and D. Meissner, *Organic solar* cells, Advanced Materials 1991, 3(3), 129-138.

34. Hoppe H. and N. S. Sariciftci, *Organic solar cells: An Overview* 2004, Journal of Material Research 19(7) 1924-1945.

35. Li G., Zhu L and Y. Yang, *Polymer solar cells*, Nature Photonics 2012, 6, 153-161.

36. Scharber, M.C. and N.S. Sariciftci, *Efficiency of bulk-heterojunction organic solar cells.* Progress in Polymer Science, 2013. **38**(12): p. 1929-1940.

37. Jorgensen, M., et al., *Stability of Polymer Solar Cells.* Advanced Materials, 2012. **24**(5): p. 580-612

38. Bhattacharya, J., et al., *Photo-induced changes in fundamental properties of organic solar cells.* Applied Physics Letters, 2012. **100**(19).

39. Street, R.A. and D.M. Davies, *Kinetics of light induced defect creation in organic solar cells.* Applied Physics Letters, 2013. **102**(4).

40. Lu, L., et al., *Recent Advances in Bulk Heterojunction Polymer Solar Cells.* Chemical Reviews, 2015. **115**(23): p. 12666-12731.

41. Green, M.A., A. Ho-Baillie, and H.J. Snaith, *The emergence of perovskite solar cells.* Nature Photonics, 2014. **8**(7): p. 506-514.

42. Kojima A.T., Teshima K. and Y. Shirai, *Novel Photoelectrochemical Cell with Mesoscopic Electrodes Sensitized by Lead-halide Compounds*, Proceedings of 210th ECS Meeting (ECS, 2006), 2006, abstract #397.

43. Kojima, A., et al., *Organometal Halide Perovskites as Visible-Light Sensitizers for Photovoltaic Cells.* Journal of the American Chemical Society, 2009. **131**(17): p. 6050-+.

44. Im, J.-H., et al., *6.5% efficient perovskite quantum-dot-sensitized solar cell.* Nanoscale, 2011. **3**(10): p. 4088-4093.

45. Kim, H.-S., et al., *Lead Iodide Perovskite Sensitized All-Solid-State Submicron Thin Film Mesoscopic Solar Cell with Efficiency Exceeding 9%.* Scientific Reports, 2012. **2**.

46. Lee, M.M., et al., *Efficient Hybrid Solar Cells Based on Meso-Superstructured Organometal Halide Perovskites.* Science, 2012. **338**(6107): p. 643-647.

47. Luo, S. and W.A. Daoud, *Recent progress in organic-inorganic halide perovskite solar cells: mechanisms and material design.* Journal of Materials Chemistry A, 2015. **3**(17): p. 8992-9010.

48. Burschka, J., et al., *Sequential deposition as a route to high-performance perovskite-sensitized solar cells.* Nature, 2013. **499**(7458): p. 316-+.

49. Liu, M., M.B. Johnston, and H.J. Snaith, *Efficient planar heterojunction perovskite solar cells by vapour deposition.* Nature, 2013. **advance online publication**.

50. Zhou, H.P., et al., *Interface engineering of highly efficient perovskite solar cells.* Science, 2014. **345**(6196): p. 542-546.

51. Yang, W.S., et al., *High-performance photovoltaic perovskite layers fabricated through intramolecular exchange.* Science, 2015. **348**(6240): p. 1234-1237.

52. Saliba, M., et al., *Cesium-containing triple cation perovskite solar cells: improved stability, reproducibility and high efficiency.* Energy & Environmental Science, 2016.

53. RLE perovskite seminar series, MIT.

54. Samiee, M., et al., *Defect density and dielectric constant in perovskite solar cells.* Applied Physics Letters, 2014. **105**(15).

55. Hoke, E.T., et al., *Reversible photo-induced trap formation in mixed-halide hybrid perovskites for photovoltaics.* Chemical Science, 2015. **6**(1): p. 613-617.

56. Stoumpos, C.C., C.D. Malliakas, and M.G. Kanatzidis, *Semiconducting Tin and Lead Iodide Perovskites with Organic Cations: Phase Transitions, High Mobilities, and Near-Infrared Photoluminescent Properties.* Inorganic Chemistry, 2013. **52**(15): p. 9019-9038.

57. Leijtens, T., et al., *Electronic Properties of Meso-Superstructured and Planar Organometal Halide Perovskite Films: Charge Trapping, Photodoping, and Carrier Mobility.* ACS Nano, 2014. **8**(7): p. 7147-7155.

58. Stranks, S.D., et al., *Electron-Hole Diffusion Lengths Exceeding 1 Micrometer in an Organometal Trihalide Perovskite Absorber.* Science, 2013. **342**(6156): p. 341-344.

59. Zhao, Y., A.M. Nardes, and K. Zhu, *Solid-State Mesostructured Perovskite CH3NH3PbI3 Solar Cells: Charge Transport, Recombination, and Diffusion Length.* Journal of Physical Chemistry Letters, 2014. **5**(3): p. 490-494.

60. La-o-vorakiat, C., et al., *Elucidating the role of disorder and free-carrier recombination kinetics in CH3NH3PbI3 perovskite films.* Nat Commun, 2015. **6**.

61. Miyata, A., et al., *Direct measurement of the exciton binding energy and effective masses for charge carriers in organic-inorganic tri-halide perovskites.* Nature Physics, 2015. **11**(7): p. 582-U94.

62. Hu, M., et al., *Distinct Exciton Dissociation Behavior of Organolead Trihalide Perovskite and Excitonic Semiconductors Studied in the Same System.* Small, 2015. **11**(18): p. 2164-2169.

63. Balaji, G., et al., *CH3NH3PbI3 from non-iodide lead salts for perovskite solar cells via the formation of PbI2.* Physical Chemistry Chemical Physics, 2015. **17**(16): p. 10369-10372.

64. Forgacs, D., M. Sessolo, and H.J. Bolink, *Lead acetate precursor based p-i-n perovskite solar cells with enhanced reproducibility and low hysteresis.* Journal of Materials Chemistry A, 2015. **3**(27): p. 14121-14125.

65. Li, C., et al., *Formability of ABX(3) (X = F, Cl, Br, I) halide perovskites.* Acta Crystallographica Section B-Structural Science, 2008. **64**: p. 702-707.

66. Amat, A., et al., *Cation-Induced Band-Gap Tuning in Organohalide Perovskites: Interplay of Spin–Orbit Coupling and Octahedra Tilting.* Nano Letters, 2014. **14**(6): p. 3608-3616.

67. Lee, S.J., et al., *Fabrication of Efficient Formamidinium Tin Iodide Perovskite Solar Cells through SnF2-Pyrazine Complex.* Journal of the American Chemical Society, 2016. **138**(12): p. 3974-3977.

68. Stoumpos, C.C., C.D. Malliakas, and M.G. Kanatzidis, *Semiconducting Tin and Lead Iodide Perovskites with Organic Cations: Phase Transitions, High Mobilities, and Near-Infrared Photoluminescent Properties.* Inorganic Chemistry, 2013. **52**(15): p. 9019-9038.

69. Serrano-Lujan, L., et al., *Tin- and Lead-Based Perovskite Solar Cells under Scrutiny: An Environmental Perspective.* Advanced Energy Materials, 2015. **5**(20).

70. Leijtens, T., et al., *Stability of Metal Halide Perovskite Solar Cells.* Advanced Energy Materials, 2015. **5**(20).

71. Bryant, D., et al., *Light and oxygen induced degradation limits the operational stability of methylammonium lead triiodide perovskite solar cells.* Energy & Environmental Science, 2016.

72. Mei, A.Y., et al., *A hole-conductor-free, fully printable mesoscopic perovskite solar cell with high stability.* Science, 2014. **345**(6194): p. 295-298.

73. Kaltenbrunner, M., et al., *Flexible high power-per-weight perovskite solar cells with chromium oxide-metal contacts for improved stability in air.* Nature Materials, 2015. **14**(10): p. 1032-+.

CHAPTER 2

DEVICE PHYSICS OF SOLAR CELLS

In first chapter importance of next generation, organic and perovskite solar cells were highlighted. These next generation photovoltaic technologies are unfortunately intrinsically instable to light exposure. And it is very essential to understand the reasons for the photo-degradation. However, before going to photo-degradation, working of solar cell needs to be understood. In this chapter, device physics of solar cell is briefly described.

Idea of solar cell is to directly convert solar energy into electricity. Solar energy reaches earth in the form of light, photons. Conversion of these photons to flowing current, mainly involves four processes.

1) Absorption of incident photons
2) Creation of free electron-hole pairs
3) Free charge carrier transport
4) Collection of charge carriers at respective electrodes

Following sections of this chapter will go over each of these four processes. Here all these process are explained mostly assuming classical semiconductor properties. Apart from these four processes of current generation, recombination is very significant process leading to losses in performance of solar cell. Recombination process is thus also discussed in section 2.3.1. Finally solar cell's equivalent electric circuit model is discussed.

2.1: Absorption

The first step of direct conversion of solar energy into electricity requires absorption of the solar energy. Solar energy reaches earth in the form of photons, some of which can be absorbed by given material depending on the quantum energy photon and energy levels in the material. When a material absorbs a photon, a carrier would acquire that energy and move from its relaxed ground state to a higher energy state. This carrier in excited state would tend to quickly release the absorbed energy in various forms to again attain its ground state. Thus to utilize the absorbed energy, a two-level system is required where carrier in excited state has lifetime which is at least higher than timespan required to extract the carrier. Semiconductor material with a forbidden energy bandgap between lower energy level valance band and higher energy level conduction band is an ideal two-level system for such an absorption. In semiconductor, negatively charged electron from valance band can absorb photon of energy higher than the bandgap and get excited to conduction band. This process will also create a positively charge vacancy or hole in the valance band. These electrons and holes can then be collected as current, which will be explained in the next sections.

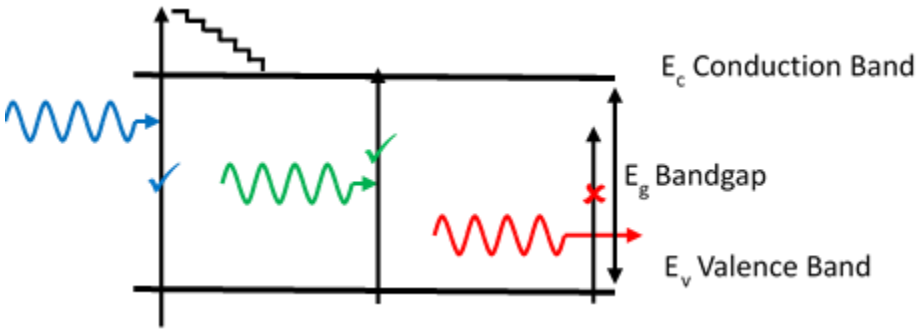

Fig. 2.1: Absorption (or transmission) of photons incident on semiconductor.

Fig. 2.1 shows the absorption in semiconductor for different photon energies. In perfect semiconductor crystal, photon (red in the Fig 2.1) whose energy (hν) is lower than the bandgap

(E_g) of the semiconductor will not be absorbed and will transmit through the semiconductors. Only those photons would be absorbed whose energies are higher than the bandgap (blue and green in Fig. 2.1). However it should be noted that energy excess to the bandgap would be immediately dissipated thermally when electron excited higher than the conduction band minima will come down to the minima of conduction band and thus would be lost.

These two phenomena give a very important criterion for deciding the semiconductor material for photovoltaic application. Solar light reaching earth's surface is basically a black body radiation of 5500^0C minus various absorptions especially in the earth's atmosphere and thus has photons from ultra-violet to all the way to near infra-red. If a very low bandgap semiconductor is chosen, it will absorb many more photons, and thus we would have many excited electrons but lot of energy will be lost in excess energy relaxation. On the other hand, if a high bandgap material is chosen, heat loss would be minimized, but number of excited electrons would also go down. Considering these two loss mechanisms, and also black body radiation of solar cell at room temperature and ideal radiation recombination, optimum bandgap and efficiency was calculated by Queisser and Shockley in 1961 to be 1.34eV and 34%[1]. An elegant solution to overcome the Shockley-Queisser limit is to use multiple absorber materials. Another solution to minimize the thermodynamic loss is hot carrier solar cells [2]. Up-conversion or down-conversion of photons can also be used to modify photon spectra to match absorber material [3, 4]. However multiple absorber tandem approach adds to the cost, where as hot carrier and up/down conversion approach is still under research.

Material absorbs all photons above its bandgap, this statement is perfectly valid only for the direct bandgap semiconductors. Semiconductors, where minimum of conduction band and maximum of valence band do not have same crystal momentum are called as indirect bandgap

semiconductor. As momentums are not matched, transition of electron from maximum valence band to minimum conduction band would not fulfill the momentum conservation and thus such a transition by itself would not occur. Thus in indirect bandgap material electrical and optical bandgaps are different. It can still absorb photons with energy lower than optical bandgap but higher than electrical bandgap with a help of phonon of correct momentum which then can satisfy both energy and momentum conservation in the three body system. However probability of such an absorption would be significantly lower than direct absorption.

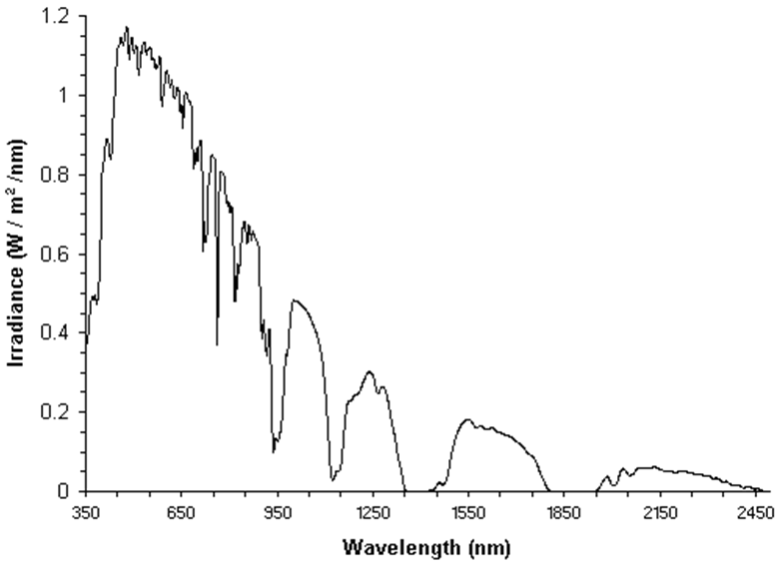

Fig. 2.2: Solar spectrum reaching on earth's surface after the absorptions in the atmosphere.

Probably of absorption can be expressed in terms of absorption coefficient. Absorption in a semiconductor is usually exponential with distance, thus intensity of incident light (I) decreases with distance x as

$$I = I_0 e^{(-x\alpha)}$$

α in this equation is called as absorption coefficient and it determines how much light is absorbed is given thickness of the semiconductor.

Thus for photovoltaic application absorption coefficient is very important parameter. Higher the absorption coefficient, higher the amount of light absorbed in same thickness of the material. Fig. 2.3 shows absorption coefficient of perovskite material compared to that of conventional photovoltaic technologies. It can be seen that perovskite material has higher absorption coefficient than c-Silicon, which is indirect bandgap semiconductor. Thus a very thin perovskite material (500nm) can be used to obtain good currents. C-Si does absorb very deep, however it should be noted that solar photons are concentrated in the visible region. Organic polymers also have high absorption coefficients in the order of high 10^6 m^{-1} and thus thin layers or organic polymers are also sufficient to get high current out of solar cell.

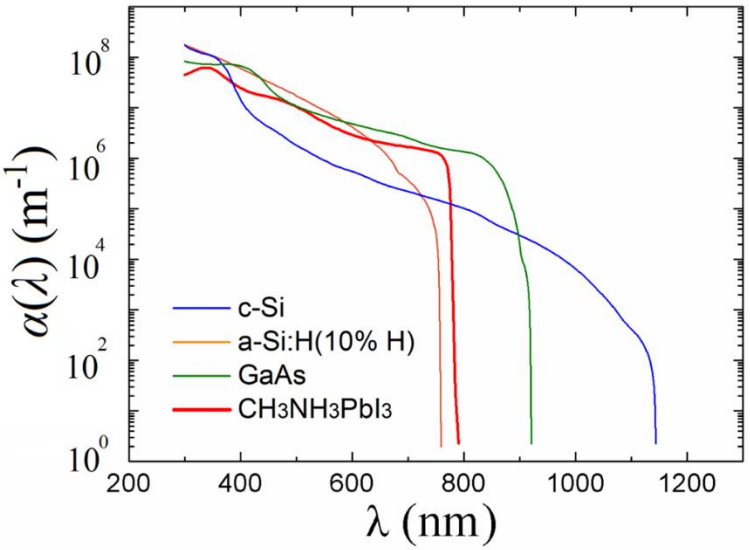

Fig. 2.3: Absorption coefficient of c-Si, a-Si:H, GaAs and perovskite [5].

2.2: Creation of free electron-hole pair

Photon absorption results in electron getting excited to conduction band. This also creates a vacancy of electron, called as hole in the valence band. This photo-generated electron-hole pair form the same photon, are attracted to each other by the attractive Coulombic force. This attractive Coulombic force gives stabilizing energy to the electron-hole pair and their energy is slight

lowered than the energy of the unbound electron in conduction and hole in valence band Thus a charge neutral bound state quasiparticle, called 'exciton' is formed as a result of photon absorption.

In a material, if photo-generated electron-hole results in bound exciton or unbound free charges depend on the binding energy of the exciton in the material and the thermal energy provided which tends to break the exciton. Thermal energy at room temperature is about 26 meV. Thus, if binding energy of exciton in material is higher than 26 meV, then at room temperature we would expect excited electron-hole pair to be in bound state, whereas it would be free if exciton binding energy is less than 26 meV.

Binding energy of exciton in a dielectric material depends on the dielectric constant of the material. Dielectric constant of relative permittivity is the material property that lowers the Coulomb attraction in any material relative to the attraction in vacuum. Binding energy of exciton in a dielectric material is given by,

$$E_b = \frac{\mu e^4}{2\hbar^2 \varepsilon^2}$$

Where, E_b is the binding energy of the exciton, μ is the reduced mass of electron, e is the electronic charge, $\hbar$ is the Planck's constant and ε is the dielectric constant of the material.

In c-Si, relative dielectric constant is 11.9, leading to exciton binding energy of around 15meV [6]. Thus, in c-Si, photo-generated electron-holes pairs would be free and can be swept easily.

However, for organic semiconductors, dielectric constants, are very low, with relative dielectric constants in 2-5. For such low dielectric constants, exciton binding energy is high around 0.2-1 eV [7]. Such high binding energy leads to inability to break exciton by mere thermal energy and thus electrons and holes are bound in an exciton state in organic semiconductors. Such bound excitons can be broken by making a heterojunction between p–type and n-type semiconductor.

Difference in conductions bands would create a heterojunction built-in field. And in most of the organic materials, field generated by 0.3 eV difference in LUMO (analogous term of conduction band in organic semiconductors) is enough to overcome exciton binding energy and break it. Fig. 2.4 represents schematic of exciton dissociation at heterojunction and entire solar cell operation in organic solar cells.

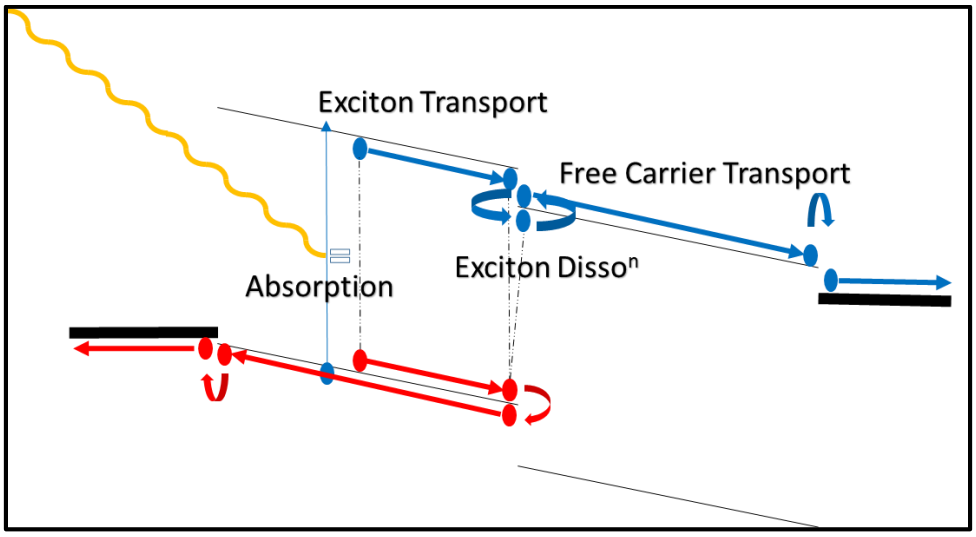

Fig. 2.4: Schematic of organic solar cell operation.

However, before breaking excitons have very small diffusion length in the order of 10-20nm. And thus even using heterojunction concept only excitons that are generated in the distance up to diffusion length of heterojunction will be separated, all other excitons will simply get recombined and energy will be lost as heat. And thus to effectively collect electron-holes some efficiency strategy needs to be used. In this context, the strategy of bulk heterojunction is very critical and was also revolutionary in organic solar cells. In bulk heterojunction, p-type and n-type materials are intermixed to form an intermixed, 3D heterojunction with an interface area orders higher than planar heterojunction. Fig. 2.5 represents a planar heterojunction in bilayer structure and intermixed 3D heterojunction in bulk heterojunction structure.

For methyl ammonium lead iodide perovskite, reported values of relative dielectric constants are 50-70 and thus estimated binding energies are about 2 meV [8]. Thus many reports have suggested that in perovskites free electron-hole pairs generated.

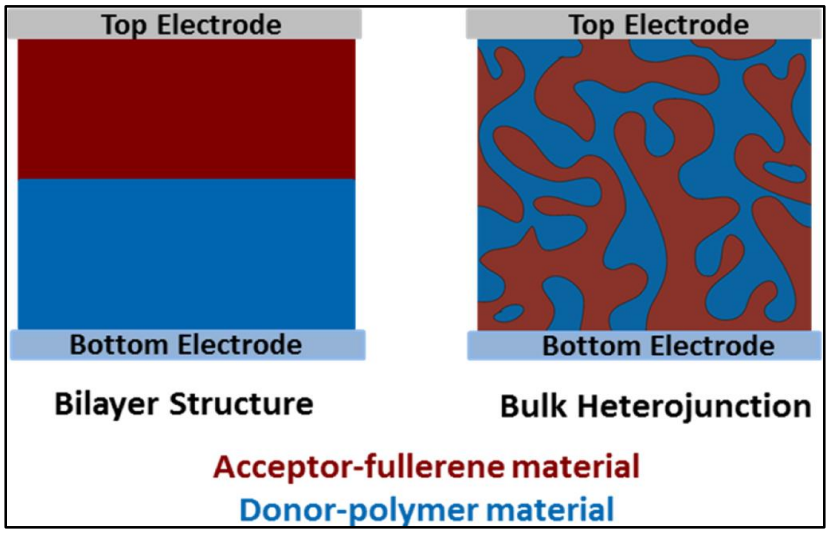

Fig. 2.5: Schematic of bilayer and bulk heterojunction structure used in organic solar cells.

2.3: Transport

Next step after creating on free charge carriers in realization of a solar cell is to separate the charges of opposite polarity towards respective electrodes. Electric field is usually used as it would force charges of opposite polarity to opposite direction. p-n junction, or a Schottky junction can be used to achieve this. In p-n junction Schottky barrier, equalization of fermi level would result in formation of depletion region near the junction, where energy bands would bend giving rise to electric field. Charges can be easily swept to the other side of the depletion region in this electric field. Device thickness in a device might be higher than depletion region and in the region outside depletion diffusion dominates the charge transport.

For photogenerated excess carriers, a complete drift-diffusion, charge continuity equation is given by,

$$D\frac{\partial^2(\Delta n)}{\partial x^2} + \mu E\frac{\partial(\Delta n)}{\partial x} + G - R = \frac{\partial(\Delta n)}{\partial t} \quad (2.1)$$

Where D is diffusion coefficient, μ is mobility, E is the electric field, G is generation and R is recombination. This is called as ambipolar transport equation.

The first term in the equation 2.3, $D\frac{\partial^2(\Delta n)}{\partial x^2}$ gives the diffusion component of current. Outside depletion region, in an absence of electric field, distribution of minority carrier charges is given by,

$$n = \Delta n\,(x = 0)e^{(-\frac{x}{L_n})}$$

Where L_n is diffusion length and is given by,

$$L_n = \sqrt{D_n \tau_n}$$

where, τ_n is the minority carrier lifetime.

Thus to effectively sweep all charge carriers to interface, one either needs high diffusion length or lower thickness.

In materials, with very low diffusion lengths, device thickness can be reduced such that depletion region extends all the way in the bulk of the device. In such conditions, drift component, as given by second term in equation 2.3,$\mu E\frac{\partial(\Delta n)}{\partial x}$ would dominate charge transport. Charge transport using drift, depends on term similar to diffusion length, referred as range, which is given by,

$$R = \mu \tau E$$

In materials with low diffusion lengths, p-i-n junction can be used to improve charge transport. In a p-i-n junction, a thick intrinsic layer is inserted between very thin p and n type layers. Here p and n layers are made thinner than diffusion length thus reducing loss because of lower diffusion length. Loss in absorption because of reduction in thickness of p and n region is

balanced by the absorption in i layer. Here depletion region extends through entire i region and thus all charges generated in i layer can be swept by drift.

2.3.1: Recombination

Excited electrons and holes would tend to recombine and come back to ground state. This recombination would lead to decrease in charge collection and hence current output of the solar cell. Recombination would be a major loss during the charge transport and thus it is considered in this section.

Excited charges can recombine through different routes. Charge can recombine by direct recombination of an electron in conduction band and a hole in valence band, which usually results in a radiative photon release. This type of recombination is called as band-band recombination. If defect density inside bandgap in the device is high, electron and holes can also recombine through trap states in the device, called as Shockley-Read-Hall (SRH) recombination. Energy release in SRH recombination is usually non-radiative resulting in heating of the sample. At very high doping level, Auger recombination, where energy released from recombination is transferred to excite another carrier, is also observed. In solar cell applications, typically at low doping levels, Auger recombination is negligible, but both band-band and SRH recombination are significant.

Band-band recombination depends on the density of electrons in conduction and holes in valance band, where recombination rate is given by

$$R = c_b\ (np - n_i^2)$$

where, c_b is a band to band recombination constant, n and p are number of electrons and holes respectively in conduction and valance band. And n_i is the intrinsic carrier concentration.

In small signal condition, lifetime for band-band recombination can be derived be inversely proportional to doping density in the semiconductor.

$$\tau_b = \frac{1}{c_b N}$$

SRH recombination, depends also on number of trap states, apart from, electron density in conduction band and hole density in valance band. In a small signal condition, SRH recombination lifetime can be derived to be inversely proportional to defect density.

$$\tau_n = \frac{1}{c_n N_T}$$

Thus the dominating recombination would depend on doping level and trap density of the material. Dominating recombination mechanism would also change in different regions of the device and at different bias conditions.

2.4: Collection

Even after efficient sweeping of charges to the edge of bulk, charges needs to be collected at the electrode. Electrode would collect charges effectively when an ohmic contact is formed between electrode and semiconductor. If workfunction of electrode is higher than workfunction of semiconductor, then a barrier would be formed for electron collection. Whereas, electrode with lower workfunction than semiconductor would result in barrier for hole collection. Thus, to effectively collect electrons, lower workfunction should be used, whereas to effectively collect holes, higher workfunction metal should be used. Fig. 2.6 from Streetman [1] shows ohmic contacts for electron and hole collections.

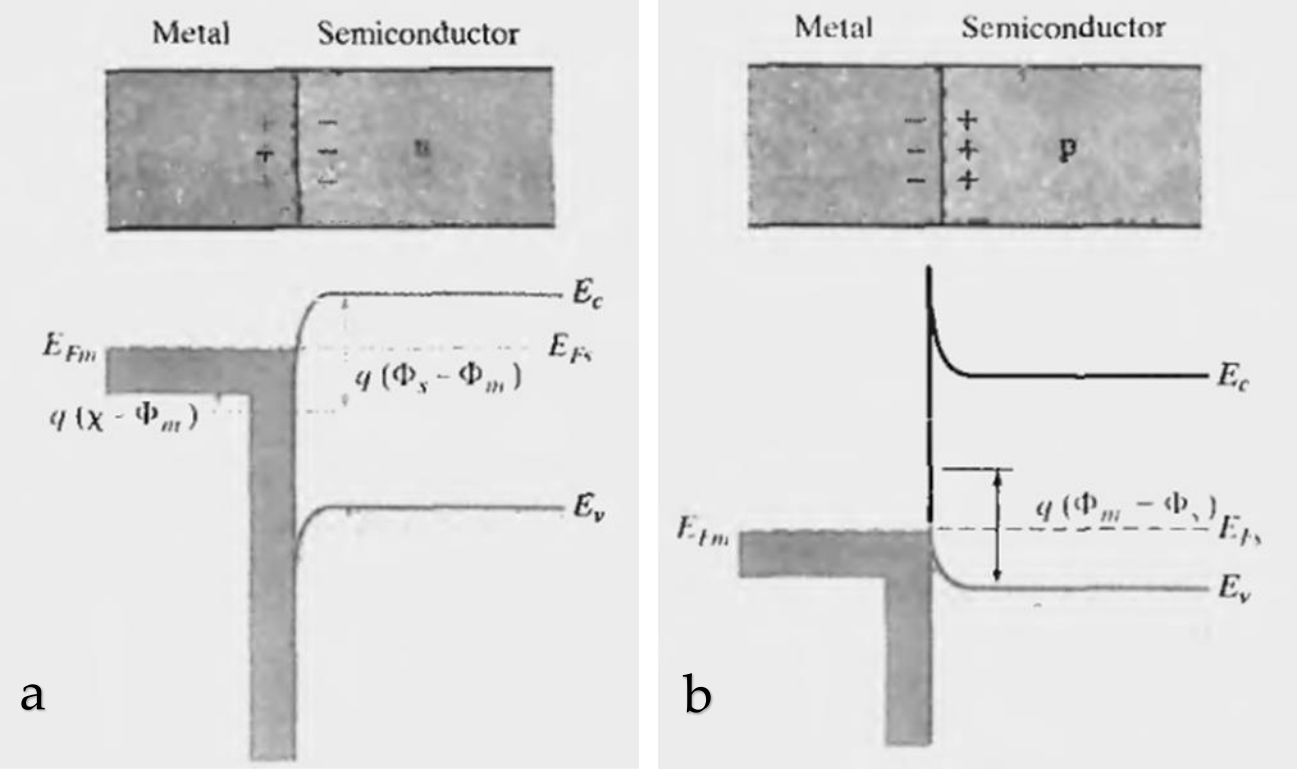

Fig. 2.6: Metal-semiconductor junctions for ohmic collection of (a) electron from n type semiconductor and (b) hole from p type semiconductor.

2.5: Equivalent Circuit

Equivalent circuit of a solar cell is shown in Fig. 2.7. Solar cell can be considered to be a current source producing current equal to photo-generated current (I_L). Two diodes are used to represent two different kinds of recombination in the bulk of solar cell. In any practical solar cell, there would be alternative shunt paths, which is represented by shunt resistance. Contact resistance would also not be perfectly zero and thus a series resistance is also included in the circuit.

In a single diode, current and voltage share an exponential relationship.

$$I = I_0(e^{\frac{qV}{n\,kT}} - 1)$$

where, *n* is the ideality factor of the diode, which depends on the recombination mechanism in the diode. $\frac{kT}{q}$ is the thermal energy at the given temperature. And I_0 is the reverse saturation current in the diode.

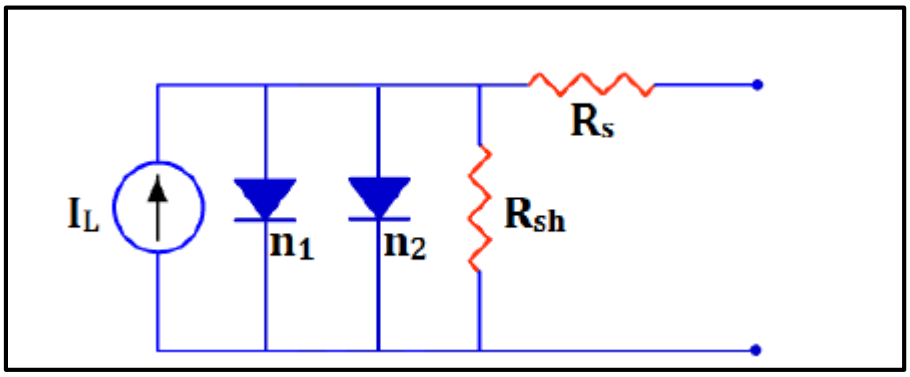

Fig. 2.7: Equivalent circuit of a solar cell.

IV relationship for the double diode model solar cell as suggested by Fig. 2.7 is thus given by,

$$I = I_L + I_{01}\left(e^{\frac{q(V+IR_s)}{n_1\,kT}} - 1\right) + I_{02}\left(e^{\frac{q(V+IR_s)}{n_2\,kT}} - 1\right) + \frac{V + IR_s}{R_{sh}}$$

Here two different diode are used to include possibility of two different recombination mechanisms. In depletion region, diode current is proportional to $e^{\frac{qV}{2\,kT}}$, whereas in quasi-neutral region, diode current is proportional to $e^{\frac{qV}{1\,kT}}$. At lower bias, device is still in depletion and thus n=2 region can be seen at lower bias. When high forward bias is applied on device, depletion region is reduced and n=1 quasi-neutral region recombination dominates. This n=1 and n=2 region can be easily in dark IV when, $I_L = 0$.

In presence of light, I_L has a high negative value. Device thus has negative current at 0 bias and even at positive bias until applied bias is equal to

$$V_{oc} = \frac{qV}{n\,kT}\ln\left(\frac{I_L}{I_0}\right)$$

Here for simplicity, one diode model is considered.

Thus, for voltages between 0 and V_{oc}, device has positive voltage and negative current. And in these values device can be used as power source.

2.6: References

1. Shockley, W. and H.J. Queisser, *DETAILED BALANCE LIMIT OF EFFICIENCY OF P-N JUNCTION SOLAR CELLS.* Journal of Applied Physics, 1961. **32**(3): p. 510-.

2. Koenig, D., et al., *Hot carrier solar cells: Principles, materials and design.* Physica E-Low-Dimensional Systems & Nanostructures, 2010. **42**(10): p. 2862-2866.

3. Trupke, T., M.A. Green, and P. Wurfel, *Improving solar cell efficiencies by down-conversion of high-energy photons.* Journal of Applied Physics, 2002. **92**(3): p. 1668-1674.

4. van Sark, W.G.J.H.M., et al., *Upconversion in solar cells.* Nanoscale Research Letters, 2013. **8**.

5. Xie, Z., et al., *Refractive index and extinction coefficient of CH3NH3PbI3 studied by spectroscopic ellipsometry.* Optical Materials Express, 2015. **5**(1): p. 29-43.

6. Green, M.A., *Improved value for the silicon free exciton binding energy.* Aip Advances, 2013. **3**(11).

7. Knupfer, M., *Exciton binding energies in organic semiconductors.* Applied Physics a-Materials Science & Processing, 2003. **77**(5): p. 623-626.

8. Lin, Q., et al., *Electro-optics of perovskite solar cells.* Nature Photonics, 2015. **9**(2): p. 106-112.

9. http://pveducation.org/

10. https://www.pvlighthouse.com.au/

11. Streetman B and S. Banerjee, *Solid State Electronic Devices*, Prentice-Hall Inc.New Jersey, 2006.

12. Samiee M., *Device physics of organic and perovskite solar cells*, 2015. *Graduate Theses and Dissertations*.

13. Bhattacharya, J., *Understanding the physics of degradation of polymer solar cells* (2013). *Graduate Theses and Dissertations.* Paper 13475.

CHAPTER 3

METHODS: FABRICATION AND CHARACTERIZATION

In second chapter, the device physics of solar cells was discussed. The working of a solar cell was briefly explained in the chapter. In this chapter, the fabrication and characterization methods for both organic and perovskite solar cell would be discussed.

3.1: Device architecture

Solar cells can be made in four structures depending on the order of fabrication and direction of flow of current.

If a device is grown on the top of a glass substrate with metal back contact, such that light comes from glass side, then such a structure is called as substrate cell. If a device is made on metal surface (for example stainless steel) with transparent front contact, then such a device is called as superstrate device. Making a superstrate device requires ability to deposit transparent contacts, which usually require high temperature step. Active layer of devices made in this work, especially perovskites are not very stable at high temperature, and thus perovskites are made only in substrate type. Organic films also show degradation in presence of plasma and thus in this work only substrate type devices were made. Depositing metal back contact is comparatively easy and does not harm the active layer.

Devices can also be distinguished depending on the direction of flow of current. If the light falling on device first sees n type electron transport layer and then active layer and then p type hole

transport layer, then such a device is called as n-i-p device. Whereas if light follows path in the order of hole transport layer, active layer, electron transport layer then it is called p-i-n device.

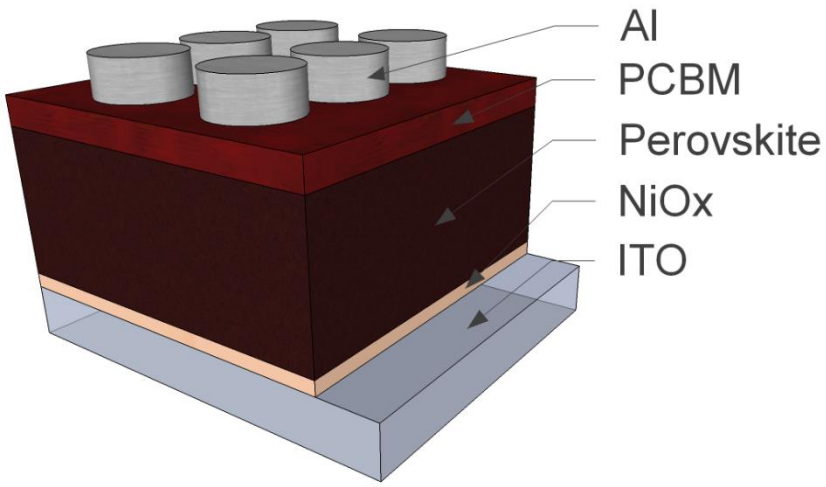

Fig. 3.1: Typical substrate p-i-n perovskite solar cell.

Fig. 3.1 shows a typical p-i-n perovskite solar cell made on the top of glass in substrate structure, where NiO_x is the hole transporting layer, whereas PCBM is electron transporting layer. NiO_x can be changed for any hole transporting layer and PCBM by other electron transporting layers and the device would still be p-i-n. If the layer next to glass is changed to electron transporting layer and layer before metal is changed in hole transporting layer, then such a device would be n-i-p. Most of the work in this report was done on p-i-n structure substrate devices and thus explanation would be mostly from p-i-n perspective.

3.2: Fabrication

As mentioned in previous chapter, a complete solar cell consists of photovoltaic layer sandwiched between the transport layers. Finally charges are collected from transport layers either through metal or transparent conductive oxides (TCO).

Indium tin oxide (ITO) or Fluorine doped Tin Oxide (FTO) are common transparent conductive oxides used. As it can be seen from Chapter 2, transport layer should form an ohmic contact with the TCO for effective collection of charges. Thus, ITO which has a work function of around 4.7-4.9 eV works better for hole transport layers, as both organics and perovskites have a valance band or HOMO (highest occupied molecular orbital) at around 5-5.4 eV. FTO which has a work function of around 4-4.3 eV would work better for electron transport layer, as conduction bands in organics and perovskites are around 3.8-4 eV.

3.2.1: TCO

ITO / FTO are commonly deposited by sputtering. In this work, one side ITO/FTO-coated glass slides purchased from Colorado Concept (ITO) and Delta Technologies (FTO) were used. ITOs were 120 nm thick, with a sheet resistance of 12-15 Ω/□ as reported by the manufacturer. Our measurements also gave sheet resistance between 13-14 Ω/□ for them.

The device was first scribed on the back of the ITO coated glass (glass side) so that devices can be distinguished after complete fabrication. After scribing the name, first step was to clean the substrate. For cleaning, substrate was sonicated in surfactant for at least 30 minutes. It was observed that sonication at higher temperatures is beneficial and thus 50^{o}C was routinely used during sonication. After sonication in surfactant, substrate was sonicated in DI water three times, to completely remove the remaining detergent. At this stage, substrate should be hydrophobic, in case of hydrophilicity surfactant sonication is repeated to get a good hydrophobic substrate. This is followed by sonication in isopropanol, acetone and again isopropanol, each for 5 minutes. For all the sonication steps, clean petri-dishes were used, such that we had one petri-dish designed for

one particular solvent. Substrates were finally stored in fresh isopropanol and were blow-dried by pure N_2.

In case of devices with PEDOT as hole transport layer, it was observed that oxygen plasma cleaning just before depositing the hole transport layer is beneficial for device performance and it can further remove some contaminations and also reduce workfunction of ITO. However, for devices with NiO_x hole transporting layers, plasma cleaning was found to worsen the device performance.

3.2.2: Transporting Layers

Common hole transporting layers used are PEDOT:PSS, NiO_x, MoO_x, P3HT, etc. In this work, PEDOT (workfunction: 5.1eV) was used in organic devices, whereas NiO_x (valence band = 5.3 eV) was used in perovskite devices. MoO_x has also shown good results, especially in organic devices, it further is advantageous that it can be evaporated inside glovebox and thus can also be deposited on top of organic film in the n-i-p architecture. P3HT or for that matter any organic polymer which have HOMO of around 5.1-.5.4 eV can be effective hole transporting layers, however perovskite solution does not spread well on such polymers, thus P3HT was used mainly in n-i-p perovskite device.

PEDOT:PSS can be spin-coated on cleaned substrate and thus is very commonly used. In this work, all organic devices were made on PEDOT:PSS. PEDOT:PSS as purchased usually from Clevious comes in an aqueous solution form. PVP AI 4083 PEDOT:PSS was used in this work. Note that PEDOT:PSS is stored in refrigerator and it is necessary to sonicate the solution for a few minutes and then filter it (usually 0.45 μm PVDF filter) before use. Sometimes PEDOT:PSS was filtered twice as single filtering was still giving patterns in the film. Spincoating at 4000rpm for

40 seconds gives a uniform film of around 30-40 nm. As PEDOT:PSS is aqueous solution, all processing is done outside the glovebox in chemical hood. The film needs to be annealed at 150^{o}C for 20 minutes in air to completely remove any moisture from the PEDOT:PSS before transferring it to glovebox. PEDOT:PSS being highly hygroscopic might absorb some moisture during transfer and thus after transferring inside glovebox also, PEDOT:PSS is annealed at 150^{o}C for 10 minutes. Aqueous solution, 150^{o}C temperature requirements restrict the use of PEDOT:PSS on top of organic or perovskite, which degrade in presence of moisture and thus PEDOT:PSS is used only in p-i-n architecture.

In our lab, NiO_x thermal evaporation or spincoating was not very successful. However NiO_x e-beam evaporation has given us very good results, especially with perovskites. In this work, devices were made on 40 nm thick NiO_x, deposited by e-beam evaporation at base pressure of $4x10^{-6}$ T at 0.5 Å/s. Deposition was done at room temperature, however film was then annealed at 200^{o}C for one hour in air.

Common electron transporting layers are Cs_2CO_3, Ca, TiO_2, ZnO, PCBM, etc. Cs_2CO_3 has been used mainly in n-i-p organic films, whereas TiO_2 is mostly used in n-i-p perovskites. ZnO can also be used in n-i-p architecture, however our work suggested that ZnO by itself gives lower V_{oc} in organic devices, whereas perovskites grown on top of ZnO were thermally instable. Ca and PCBM were mostly used in the devices here.

Ca (workfunction =2.7 eV) can be deposited on top of organic layer (polymer:PCBM) easily by thermal evaporation. Very thin layer of Ca would pin the fermi function of PCBM and thus help in achieving higher V_{oc}. Usually 20 nm of Ca is thermally evaporated on top of organic layer at 0.4-0.5 Å/s after achieving a base pressure of $4x10^{-6}$ T. 5 nm and 25 nm of Ca has also given similar results.

PCBM has shown good results when used as electron transport layer on perovskite film. PCBM has LUMO at 4 eV and thus it forms a good ohmic contact with 3.8 eV perovskite conduction band. In this work, 30 mg/ml solution of PCBM in Chlorobenzene is spincoated at 2000 rpm to get thickens of around 80 nm. PCBM layer is then annealed at 50^{o}C for 20 mins. Annealing PCBM to higher temperatures like 100^{o}C has also given similar results.

It should be noted that in the bulk heterojunction organic devices, both p-type polymer and n-type PCBM are in contact with both transport layers and thus there can be significant recombination at the transporting layer interface. And thus for effective charge collection, hole transporting layer should also have energy bands such that it will act as electron blocking layer, and electron transport layer as hole blocking layer.

3.2.3: Back Contacts

Aluminum (workfunction = 4.0-4.2 eV), silver (workfunction = 4.2-4.7 eV), gold (workfunction = 5.1-5.5 eV) are commonly used metals. Al, Ag work better for p-i-n devices for their low workfunction, whereas Au works better for n-i-p.

In this work Al was used as it is cost-effective and also it can be evaporated easily. Al is deposited on top of Ca or PCBM to make back contact on the device at base pressure of $4x10^{-6}$ T and at growth rates of 2-5 Å/s. Al is very reactive and higher base pressure or higher O_2 content would result in formation of Al_2O_3. 120 nm is usually deposited as lowering down the thickness would increase the probability of shorting out device when touched by the probe, however thickness as less as 60 nm has given good devices, but one needs to be very careful to not poke Al when it is this thin.

3.2.4: Organic film

As mentioned in Chapter 2, bulk heterojunction structure is used in organic devices. In this, polymer is mixed with PCBM in solution which is then spin-coated. Polymer:PCBM phase separation can be adjusted by adding additives in the solvent which selectively dissolve only one of the two phases.

In this work, PTB7 and PTB7-Th polymers were used. 10 mg of polymer was mixed with 15mg of $PC_{70}BM$ in 1 ml of solvent. $PC_{70}BM$ is used instead of $PC_{60}BM$ as it has better absorption in lower wavelengths and thus results in higher I_{sc}. Work on PTB7 has shown that mixing 3% of DIO in DCB solvent results in smaller phase of polymer, thus giving higher performance. In this work also 97% DCB + 3% DIO was used as solvent for both polymers. Such a solution is stirred using magnetic stirrer at 70^{o}C for at least two nights. PTB7 and PTB7-Th polymers are difficult to dissolve in DCB and thus higher temperature and longer time are needed. Solution is filtered using 0.2 µm PTFE filter before spin-coating. It was found that spin-coating at 1000rpm for 60 seconds gives around 100 nm film, which shows optimal performance. Such deposited film is then thermally annealed at 110^{o}C for 10 mins. Thermal annealing is very important as it increases V_{oc} from 0.75V to 0.78V for PTB7 with a very slight decrease in I_{sc}. Higher annealing temperature and times can also be used, however after a point it would lead to significant decrease in I_{sc} and slight increase in V_{oc}.

3.2.5 Perovskite film

Perovskite can be formed by simple mixture of PbI_2 and MAI, and thus it can be formed in multiple ways. Both constituents can be first mixed and then deposited on substrate or each one of them can be deposited on top of each other (usually MAI on top of PbI_2) and allowed to diffuse in.

All these depositions can be done either by solution processing or through vapor deposition. In this work, perovskite films were mainly deposited by single step liquid processing.

PbI_2 and MAI are mixed in DMF solvent in 1:1 ratio at 1.67M concentration. DMSO, a Lewis base, is also added in solvent in 1.67M as it forms an either complex with Lewis acid [PbI_2.DMSO] or [PbI_2.DMSO.MAI], which gives lower pin-holes in the film. It was observed that for NiO_x (and even PEDOT), 50 µL of solution is enough to completely cover the substrate as solution has low contact angle. After starting spin-coating of such solution, when uniform thickness of film is formed and when film still has significant amount of DMF, anti-polar solvent CB is added on the rotating substrate. DMF is miscible with CB and thus gets dissolved in CB, however perovskite is insoluble in CB. And thus when the large amounts of CB (usually 150 µL) are being spun away, CB takes DMF with it resulting in fast-crystallization of perovskite film. Such a crystallization results in dense perovskite film. In this work, CB was added exactly after 10 seconds, within half a second on substrate spinning at 4000 rpm. It should be noted that out of these 10 seconds, first 4 seconds are set for ramp up and thus substrate is at 4000 rpm only for 6 seconds. It was observed that if CB is added late it results in foggy film, whereas if it is added too early splash patters are observed on the film. Such 4000 rpm/ 25 second spinning results in light brown color film, which when annealed at 60^{o}C turns to dark brown in around 10 seconds. Film is annealed for 60^{o}C/1 min and 100^{o}C/2 min to completely remove DMSO. It was observed that if second annealing temperature is increased, device gives higher I_{sc}, especially in the case of PEDOT substrate, which have lower currents at standard 100^{o}C annealing condition.

3.3: Characterization

3.3.1: Degradation setup

In this study, focus was to understand light induced degradation in organic and perovskite solar cells. Moisture is known to degrade organic and perovskite solar cells. Whereas oxygen is also known to degrade organic solar cells. As devices were not encapsulated, to study effect of only light, moisture and oxygen needed to be removed from the setup. Inert atmosphere were developed in two setups 1) environmental chamber 2) glovebox.

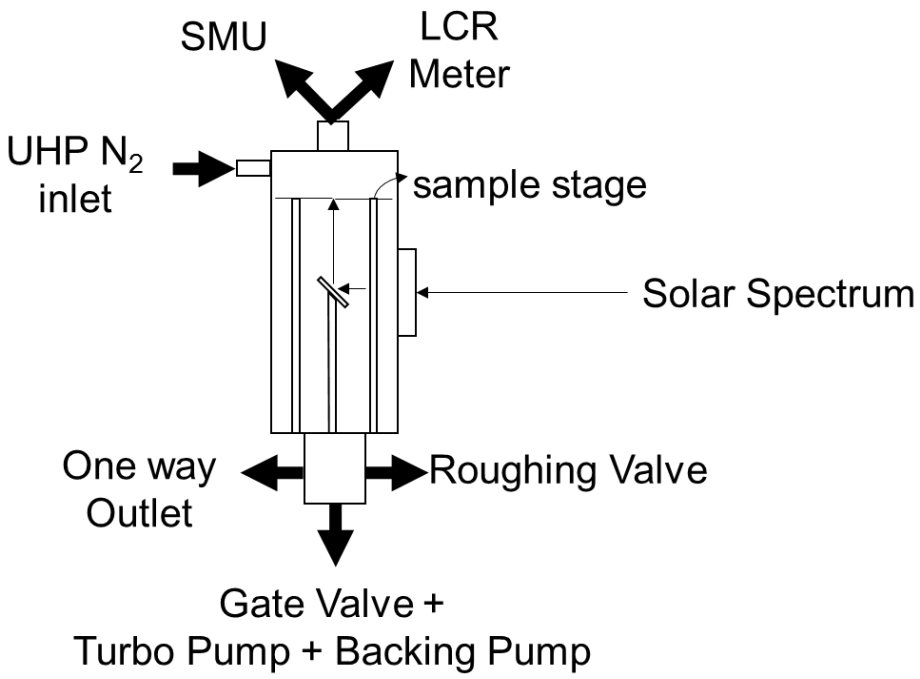

Fig. 3.2: Schematic diagram of environmental chamber.

Fig. 3.2 represents a schematic diagram of the environmental chamber. Loading the sample in the environmental chamber required opening to chamber to air. However, the chamber could then be evacuated to practically evacuate all moisture and oxygen, and then inert gas was filled in the chamber. Chamber was connected with a turbo pump supported by a backing pump and also a roughing pump. Mechanical roughing pump was used to evacuate chamber from atmospheric

pressure to 1 T. Turbo pump was opened after pressure of the chamber lowered to a value below 1 T. This is because at higher pressures, turbines of the turbo moving at high speed of 27000 rpm would stop, failing the turbo pump. A mechanical pump was also connected to back the turbo pump as even at the back end turbo pump can't be exhausted to atmospheric pressure. Using this assembly, pressure of the chamber was reduced such that outgassing in the chamber (after reduction of pressure and with all pumps/gas inflows closed) is very less. 0.1 mT/ min outgassing was considered to be the threshold where it is assumed that chamber is inert enough. This low outgassing was achieved usually when the pressure of the chamber is reduced below $2x10^{-5}$ T. After evacuating chamber of all air, ultrahigh pure N_2 was filled in the chamber using N_2 dewer connected to the system. A N_2 cylinder was also kept as a reserve to the dewer. It was also observed in different solar cell technologies, that temperature can have an effect on the performance of the solar cell and thus it is necessary to keep temperature of the sample constant and not let it heat up from the infra-red photons. During exposure, a fan was kept next to sample under exposure to avoid heating of the sample. A fan also needs continuous flow of gas, otherwise in closed system fan would not be able to avoid heating. It was observed that 0.5 SLPM flow of N_2, along with fan is enough to maintain temperature of the device under exposure for an AM1.5 exposure. A one-way outlet valve was connected to the chamber to only let the N_2 go out and not let any outside air leak inside chamber. Chamber was also otherwise tightly screwed to avoid any air leakage.

While loading also, sample was blasted with N_2 to avoid any degradation during the few tens of seconds which loading required.

Another system was a N_2 purged glovebox. Glovebox is never exposed to air and samples are loaded through pass-chambers. Moisture, oxygen is completely removed from the sample and pass-chamber by purging system with mechanical pump and pure N_2 from the glovebox. Only

when pass-chamber does not outgas it is opened to glovebox thus making sure no moisture or oxygen comes into the system. A copper catalyst, molecular sieve and continuous circulation of N_2 is also used to reduce any moisture/oxygen leaked in the system.

Fig. 3.3: Photograph of the environmental chamber (left) and glovebox systems used for exposure of the device in inert atmosphere.

It can thus be confidently asserted that during exposure, both the systems were completely inert. In both systems, a transparent window was used for the incident illumination. Quartz window was used to minimize any absorption of the incoming AM1.5 spectrum. Fig. 3.3 shows photographs of both the systems.

3.3.2: Light source

Previous studies have shown that degradation is lowered when UV component is not present in the light source. Thus using only white LED would lead to incorrect determination and a full solar spectrum light source was used. ABET 105000 solar simulator was used to obtain a full solar spectrum. Fig. 3.4 shows a typical output spectrum of the xenon lamp of ABET 105000. From Fig. 3.4 it can be seen that there are few high intensity peaks in IR region for ABET. An extra AM1.5G filter from ABET technologies was used to reduce the extra photons in the IR region. ABET technologies suggest that no two AM1.5G filters are the same and thus there can be

minute differences in the spectrum of different systems. It should also be noted that incorrect alignment of ABET can result in wrong spectrum. Even though both organic and perovskite solar cells don't absorb in IR region, it is necessary to use AM1.5G filter as reference cell used for calibration of ABET is crystalline-Si which absorbs till 1100 nm.

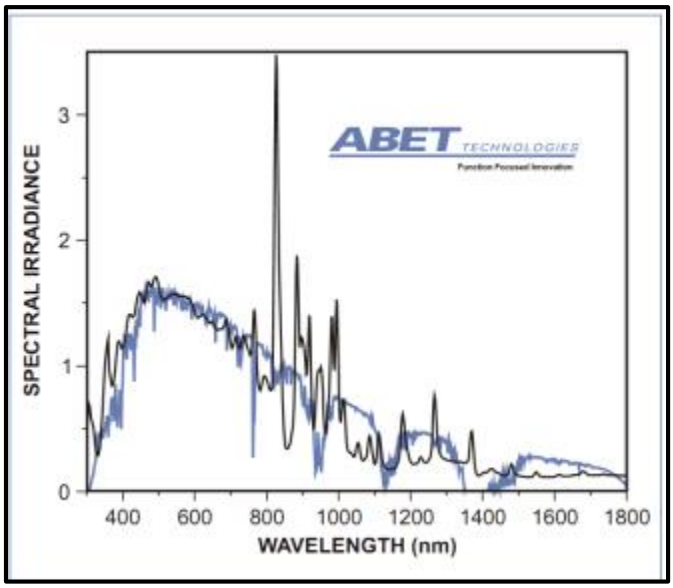

Fig. 3.4: Spectrum of the ABET 10500 (black) compared to AM1.5 [1].

3.3.3 Light IV

As mentioned above ABET simulator was used to simulate solar spectrum during current-voltage measurements under light to evaluate performance of the solar cell.

Keithley 236 source-measure-unit (in some systems Keithley 237 SMU) was used to measure current-voltage curve. A customized LabVIEW program was used during measurements. In perovskite solar cells, IV measurement direction and sweep rate can have significant effect on the obtained IV and thus conditions used during IV measurement were noted. IV was always scanned from high bias-low bias. Value of high bias was kept usually at 15% higher than V_{oc}, which was measured before starting sweep. Low bias value was usually kept between 0V and -1V depending on the device. V_{oc}, $I_{sc,}$ FF and efficiency of solar cell can be estimated by sweep till 0V,

but going negative in voltage sweep usually provides more information, especially about the collection of charges.

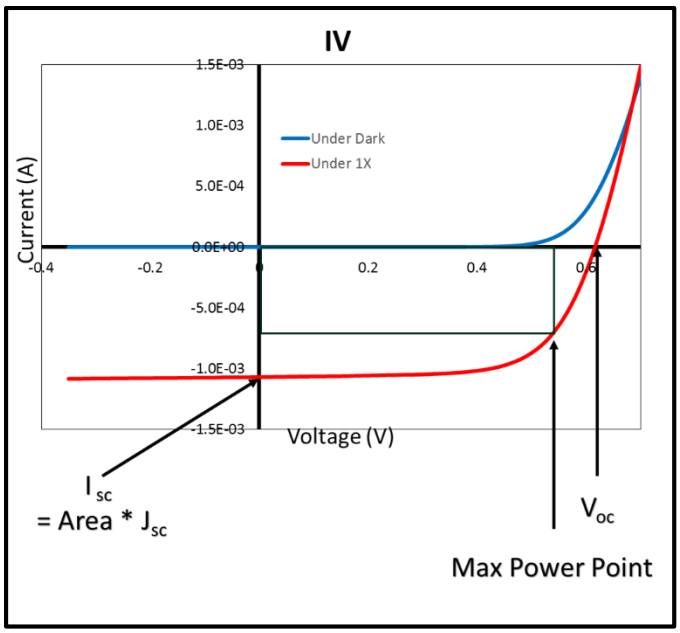

Fig. 3.5: Typical IV of an organic solar cell.

Fig. 3.5 shows a typical IV curve of a solar cell. As seen in Chapter 2, a solar cell is a simple p-n junction diode optimized to operate in fourth quarter in IV graph where it can be used as a power source. Important parameters of the solar cell are the voltage at zero current (also called as the open circuit voltage, V_{oc}) and current at zero bias (also called as short circuit current, I_{sc}). Fill factor is defined as the squareness of the IV curve or the ratio of maximum power to product of V_{oc} and I_{sc} and is usually reported in percentage. Thus the product of V_{oc}, I_{sc} and FF gives maximum possible power output of the device. When this number is divided by AM1.5 intensity which is 100mW/cm^2 gives us the efficiency of the solar cell. Thus for current density J_{sc} in mA/cm^2, power conversion efficiency (PCE) of a solar cell simplified to be given by equation below,

$$PCE = V_{oc}J_{sc}FF$$

In simple terms, V_{oc} of a solar cell is determined by the bandgap of the active material and recombination in the device. I_{sc} of a solar cell is determined by the absorption coefficient and thickness of the active layer. FF depends on the series and the shunt resistance in the device. Series resistance and shunt resistance can also be calculated from the IV curve. In an approximate procedure R_{sh} and R_s can be estimated by calculating resistance near short circuit and open circuit conditions. In an ideal solar cell R_s is zero and R_{sh} is infinite. R_s, R_{sh} calculations from IV curve can help in understanding about the presence of barrier at interface and shunting in the device.

3.3.4: Hysteresis in IV measurement

Perovskite device shows different values in IV measurement depending on the pre-biasing condition, scan direction, scan speed and also voltage range. The term hysteresis, however, is generally used for difference in IV curves when measured in different sweep directions.

Exact measurement protocol for hysteresis is rarely reported in research papers. However, hysteresis is typically measured by sweeping IV in one direction, immediately followed by IV sweep in other direction. It should be noted that the amount of hysteresis also depends on the direction that is scanned first. Hysteresis is usually measured such that first high bias-low bias is measured followed by low bias-high bias. In this work all hysteresis are measured only in this way. However, we propose to measure IV in different sweep directions only after complete relaxation of the charges to get more accurate idea of hysteresis in the device.

3.3.5: Dark IV

As solar cell is simply a diode, dark IV of a solar cell can give significant information about the recombination in the solar cell. Fig. 3.7 shows a typical dark IV plotted in semi-log scale in a

perovskite solar cell. At very low voltages, shunt resistance dominates, whereas at very high voltage series resistance dominates both giving linear shape. At intermediate voltage, recombination in the device dominates, showing exponential behavior in the curve. Dark IV shown in fig. 3.6 shows a classical double diode type behavior with n=2 and n=1 as explained in Chapter 2.

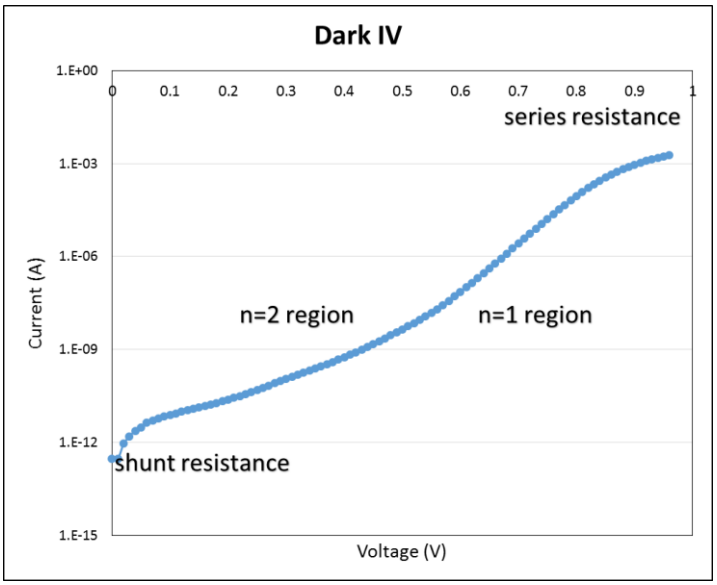

Fig. 3.6: Typical dark IV in a perovskite solar cell.

Dark IV of a device is a crucial measurement as dark IV suggests if any recombination is dominating in the device. More importantly reverse saturation current from dark IV is directly proportional to the number of defects in the device and thus reverse saturation current can give an estimate of the number of defects in the device.

3.3.6: Quantum Efficiency and Subgap Quantum Efficiency

External quantum efficiency (QE) is the ratio of the collected photo-generated charge carriers to the number of incident of incident photons. It is usually measured as a function of wavelength or energy of the incident photons. Thus QE gives an idea of the absorption of the

material at different wavelength (thus bandgap) and also collection efficiency of the device. It is essential to only measure photo-generated charge carriers to get correct estimate of collection in the device. In the QE system, we measure only photo-generated charge carriers by using a lock-in amplifier connected to a chopper. Chopper is used to have square wave type input of light at fixed wavelength. Lock-in amplifier is synchronized with the frequency of the chopper and it measures only signal which changes with the same frequency as incident light, thus giving only photo-generated current. QE can also be measured as a function of bias, which would give a better idea of the collection of the device than IV as in QE only photocurrent is measured.

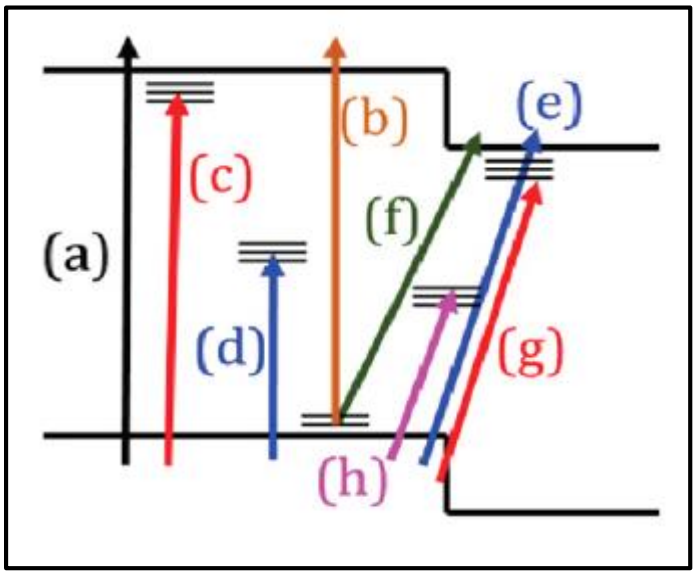

Fig. 3.7: Absorptions in the bulk-heterojunction solar cell with defects inside bandgap [2].

Subgap QE is an extension of QE in energies lower than the bandgap of the active material. Active layers with defects will also absorb photons with energies lower than bandgap energy. This is because apart from band-band absorption, such active layers can absorb photons through defect energy states. Fig. 3.7 shows possible absorptions in the organic bulk heterojunction solar cell. Bulk heterojunction would further add more possible absorption paths across interface of heterojunction. In Fig. 3.7 bandgap absorption is shown by (a). (b), (c) and (d) show tail-band,

band-tail and mid-gap absorption in the bulk of the active layer. (e), (f), (g), (h) show band-band, tail-band, band-tail and mid-gap absorption at the heterojunction interface. Subgap QE can give an idea about defects in the bandgap of the device by correlating energy required for different absorptions to the subgap QE signal at different energies below the bandgap of the material. Urbach energy of a material for both bands gives an idea about the depth of tail states at the band and can be calculated by the slope of the subgap in semi-log scale.

3.3.7: Capacitance spectroscopy

Capacitance of a p-n junction depends on the depletion region and thus applied bias. Measuring capacitance versus voltage can be used to calculate doping density in the active layer. Assuming Schottky junction and considering depletion assumption capacitance of the device can be written in terms of the doping density of the device.

$$C = \frac{\varepsilon A}{W_{dep}} = \sqrt{\frac{q\varepsilon A N_D}{2\,(V_{bi} + V_{app})}}$$

Thus doping density of the device can be calculated from the C-V measurements.

Depletion width of the device can increase up to the device thickness, at the most. Thus CV measurement will show saturation at lower biases. The saturated capacitance can be used to estimate thickness of the device.

CV measurements also gives an estimate on the effective built-in field in the device and thus effects of any ion accumulation on built-in field can also be seen in CV measurements.

Defects in the bandgap of the device might also respond to capacitance measurements. Depth inside the bandgap where defects would respond would depend on the frequency used

during capacitance measurement. CF measurement can be used to estimate density of states at various energy levels inside bandgap.

As at lower frequencies more defects would respond, CV measurement for doping density should be done at very low frequencies. Whereas to reduce the effect of any defects, depletion width and thus device thickness calculations should be done at very high frequencies.

In this work, Hioki 3500 LCR meter was used for capacitance measurement. This meter can use two element model and thus estimation of capacitance would require to use either series equivalent model or parallel equivalent model. In Appendix B we derive which model to use for solar cell, which is modelled by a diode with a series and shunt resistance. We show that for series resistance R_1, for shunt resistance R_{sh} and for assumed uniform over frequency capacitance C_0, there is a frequency ω, below which parallel equivalent would be more accurate and above which series equivalent model would be more accurate and this frequency is given by,

$$\omega = \sqrt{\frac{\sqrt{R_1^2R_2^2 + R_1^2(R_1+R_2)^2} - R_1R_2}{R_1^2R_2^2C_0^2}}$$

3.3.8 Other characterizations

In this work, Cary 3500 photospectrometer was used to measure absorption of thin films. Nanoscale atomic force microscopy (AFM) was used to measure surface roughness. Device thickness was measured either using Nanoscale AFM or profilometer. Raith scanning electron microscopy was used to measure grain size of the films.

3.4: References

1. Streetman B and S. Banerjee, *Solid State Electronic Devices*, Prentice-Hall Inc.New Jersey, 2006.

2. Pierret R.F., *Advanced Semiconductor Fundamentals*,Pearson Education Inc., New Jersey, 2002.

3. ABET 10500 brochure http://abet-technologies.com/wp-content/uploads/Low-cost-Solar-Simulators-2015.pdf

4. Samiee, M., et al., *Measurement of defect densities and Urbach energies of tail states in PTB7 solar cells.* Applied Physics Letters, 2014. **105**(13).

CHAPTER 4

UNDERSTANDING THE PHOTODEGRADATION MECHANISM IN ORGANIC SOLAR CELL

Organic photovoltaic devices degrade in light even in inert ambience [1-16]. This raises serious doubts on the feasibility for commercial application. Long term commercially viable application would be possible only when the intrinsic photo-degradation in OPVs is resolved. This necessitates a comprehensive and through understanding of photo-degradation mechanism. In organic solar cells, side chains on the polymer not only helps in increasing its solubility, but it can also affect the optical and electrical properties and significant enhancements in efficiency has been reported by modifying sidechain [17-21]. However, weak bonds on side chain of polymer have been often proposed as the origin of the intrinsic degradation in many polymers [4, 11, 22, 23]. In this work, we attempted to understand the effect of side chain (alkyl/thienylalkyl) on the intrinsic photo-degradation of OPV device.

4.1: Motivation

P3HT: PCBM system has been extensively studied for photo-degradation. In our lab, we have showed that P3HT: PCBM organic solar cells degrade when exposed to light in inert atmosphere [2]. Fig. 4.1 shows IV measured on ITO/PEDOT/P3HT:PCBM/Ca/Al cell before and after 2X (200mW/cm^2) exposure for 96 hours.

Further investigation showed that, degradation in performance in the device can be perfectly matched with increase in interface mid-gap defect density. Continued light exposure

increased mid-gap defect density. Density of states calculated from impedance spectroscopy substantiates increase in mid-gap defects after exposure. This increase in defect density is also supported by the increase in reverse saturation current in dark IV. Such increase in the density of mid-gap defects results in increased SRH recombination. Increased recombination increases reverse saturation current and thus decreasing the V_{oc}. Increased recombination also affects carrier collection, thus reducing I_{sc} and FF. Similar results have been shown by McGehee and Street group [4, 13].

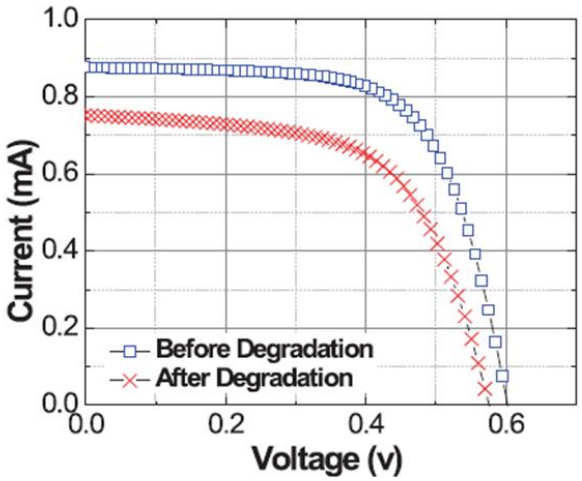

Fig. 4.1: IV measured on P3HT: PCBM device before and after exposure to 200mW/cm^2 AM 1.5 solar spectrum irradiation under Nitrogen atmosphere for 96 hours [2].

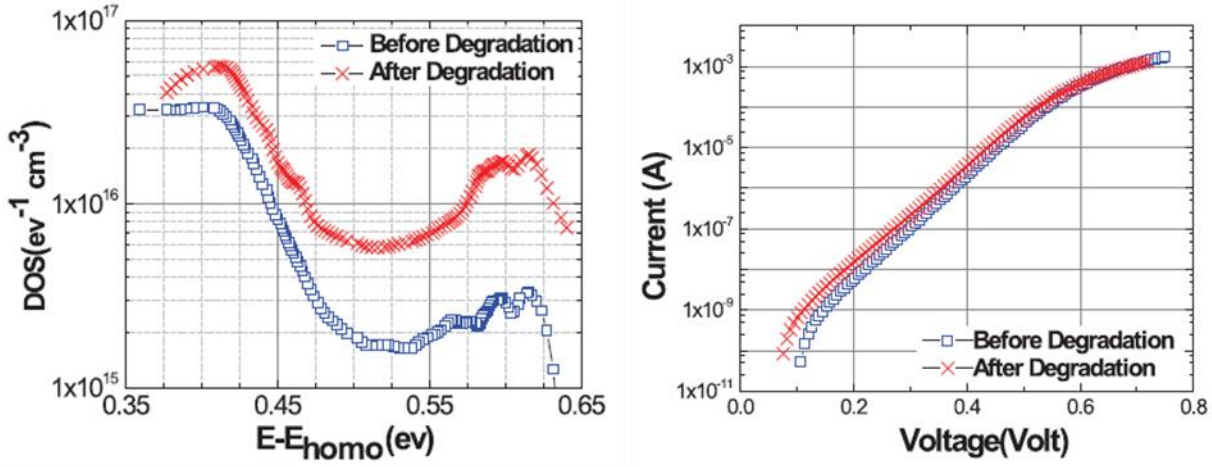

Fig. 4.2: Density of states and Dark IV measured on P3HT: PCBM device before and after exposure to 200mW/cm^2 AM 1.5 solar spectrum irradiation under Nitrogen atmosphere for 96 hours [2].

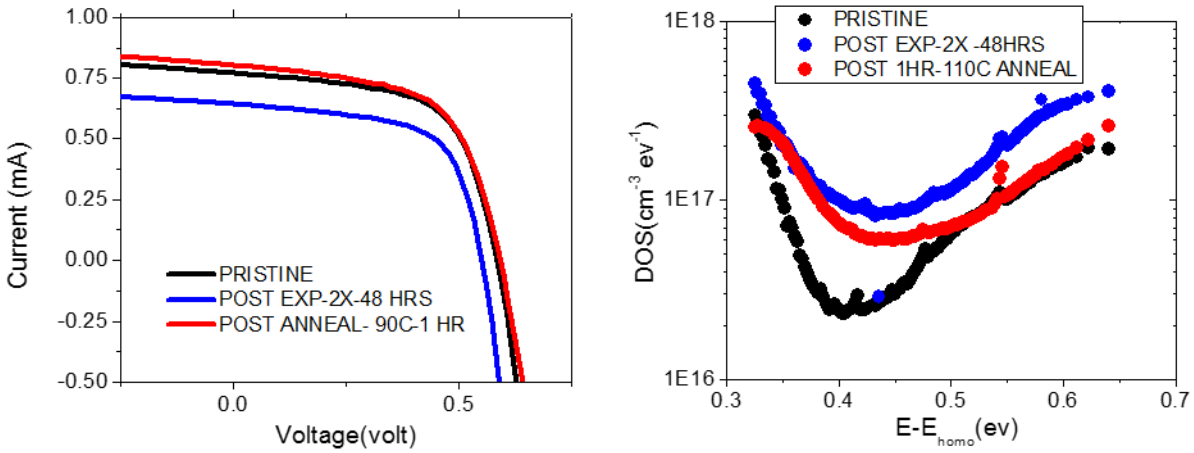

Fig.4.3: IV and Density of states measured on P3HT: PCBM device 1) before exposure, 2) after exposure to 200mW/cm^2 AM 1.5 solar spectrum irradiation under Nitrogen atmosphere for 96 hours and 3) after 90^0 C/1 hour anneal in Nitrogen purged glovebox [1].

A very interesting result was that this increase in defect density can be recovered by post degradation thermal annealing. Reduced defect density in turn also enhances photovoltaic performance to a complete recovery [1]

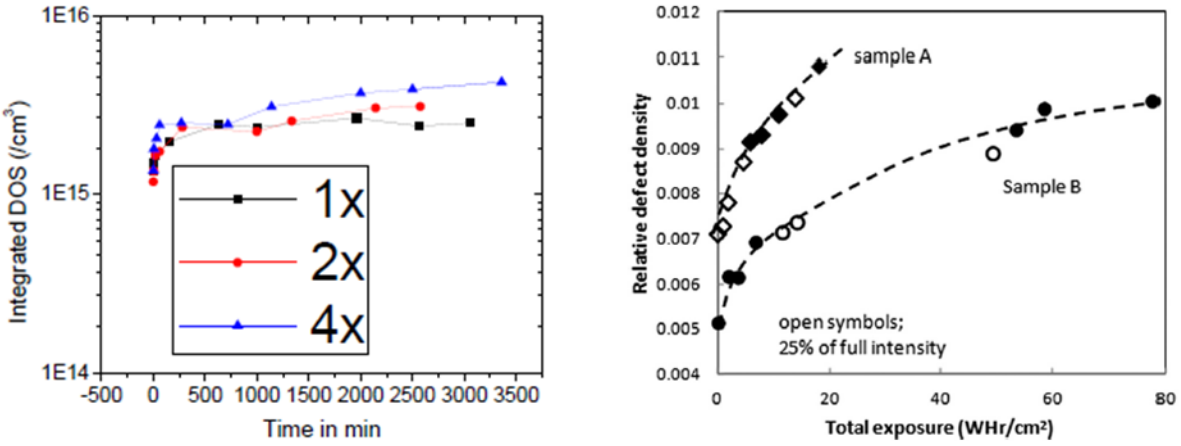

Fig. 4.4: a) Increase in Integrated density of states in P3HT/PCBM solar cell exposed to different light intensities for different times [1] and b) Increase in relative defect density in polymer: PCBM and P3HT: PCBM (sample B) device with light exposure.

It was also showed that the enhancement in mid-gap defects saturates with time. Fig.5.4 a) shows enhancement in integrated density of states over time measured in our lab. It can be seen

that, integrated density of states saturates with time. Similar results have also been shown by Street group [3].

Increase in defect density with light exposure, reversible nature of the degradation and saturation of defect density have been previously observed in the amorphous silicon solar cells [24-28]. It was observed in the amorphous silicon solar cells that upon prolonged illumination the mid-gap defect density increases. This phenomena is popularly known as Staebler-Wronski effect [25] which results in decreased photovoltaic performance. It was proposed [29] that the recombination of electron-hole pair releases energy enough to break weak Si-Si bond. Hydrogen attached to the dangling bonds switches to these broken bonds forming a metastable state, which also results in increased dangling bonds and thus increases defect density.

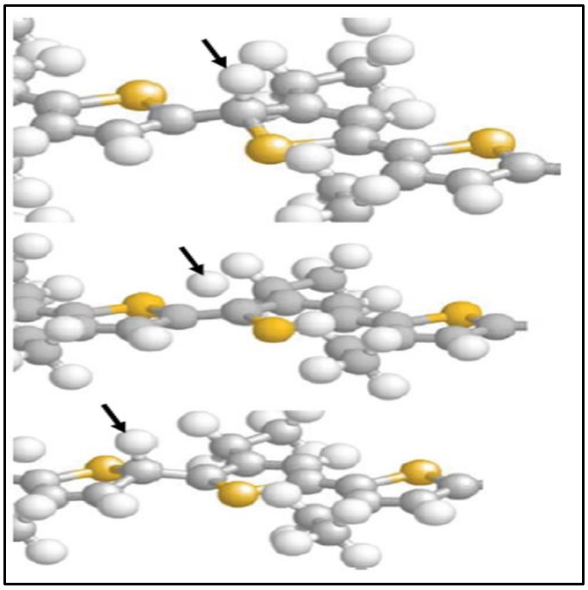

Fig. 4.5: Atomic model showing possible path of hydrogen migration. (top) initial state (central) C-H bond at α carbon breaks (bottom) hydrogen is attached to the thiophene ring [3].

Taking this argument in the arena of organic photovoltaic, Street group [4, 11] proposed a similar photo induced degradation mechanism for P3HT: PCBM based bulk heterojunction solar cells. According to this mechanism, weakest bond in the P3HT structure, α C-H bond (carbon directly connected to thiophene ring) breaks when exposed to light and H moves to thiophene ring

forming a metastable state. This leads to increased defects and which in turn leads to photo-degradation. One important point to note is this state is metastable and thus correct excitation can again make the hydrogen migrate to the α C, as is possibly case of recovery by thermal annealing.

Calculations done by Northrup and Street suggest that, bond strength of α C-H in P3AT (polymer similar to P3HT) is 4-5 eV, which raises question how could a yellow-white light, which is of around 2-3 eV breaks the bond [3, 11]. Street has suggested that there can be a few possible ways in which solar spectrum can still break the bond. (1) Two-step process, where photon excites already excited electron and (2) calculations also suggest that the H moving to thiophene ring releases energy of around 2 eV and thus net required energy is only about 2 eV, which can be provided by solar spectrum.

Similar degradation mechanism can be expected in other polymeric systems also. The weakest bond in the polymer structure will break under external excitation such as light, which might result in higher defect states, thus leading to trap assisted recombination and consequent photo-degradation. In conjugated polymers, usually the side chains have the weaker bonds as conjugation makes ring bonds stronger.

There is significant research on degradation sites for photo-oxidation reactions. Manceau et al. [30] showed that for P3HT, photo-oxidation reactions starts at the α C and not at thiophene ring as was previously believed [31]. Manceau et al. [23] studied photo-oxidation for various backbones. They concluded that polymers with side chains are most susceptible to degradation, especially the fluorine and cyclopentadithiophene. The most stable backbone was the one without side chains [23]. Xia et al. [32] reported that aryl side chains impart higher stability relative to alkyl side chains.

Photo-oxidation reactions usually starts at the weakest bond in the polymer and it is expected that even in inert atmosphere light induced degradation would also affect the same bonds first. Similar to photo-oxidation, even for photo-degradation in inert atmosphere, side chains would be the Achilles heel.

However, side chains are necessary in polymers for they give solubility to the polymer. Without sidechain solubility would be drastically affected and solution processing would be difficult. Side chains also affect the molecular packing and the electron affinity. Careful modification of the sidechain has helped in enhancing efficiency of organic solar cells [17-20, 33]. It would be interesting to see how the stability of solar cell changes with change in polymer sidechain.

4.2: Polymer selection and theoretical calculations

Two ideal candidates for this study are PTB7 and PTB7-Th. Both polymers have benzodithiophene- (BDT-) based backbones, which is considerably stable based on the rule of thumb photo-oxidation stability rankings [23]. These polymers have attracted significant attention because of their superior photovoltaic performance. High efficiencies of around 9% have been reported for both polymers in p-i-n architecture, n-i-p architecture in both these polymers have shown higher efficiencies [19, 34-37]. And most importantly for this study, they have very similar conjugated backbone, with alkoxy side chain in the PTB7 being replaced by alkyl thiophene side chain in PTB7-Th.

Low bandgap polymers have attracted a lot of attention in past decade and for their deeper absorption low bandgap polymers have achieved higher efficiencies [38, 39]. Both PTB7 and PTB7-Th have lower bandgaps of around 1.7 eV and thus absorbing deep into NIR. Their LUMO,

which is near 3.5eV, is matched for efficient electron-hole separation at the polymer: PCBM interface. Matching of LUMO allows these polymers to have lower HOMO of around 5.2 eV (even at lower bandgaps) which helps to have higher interface bandgap with PCBM giving high V_{oc}. Also both polymers exhibit high hole mobilities, in the order of 10^{-4}s cm^2/Vs [40, 41].

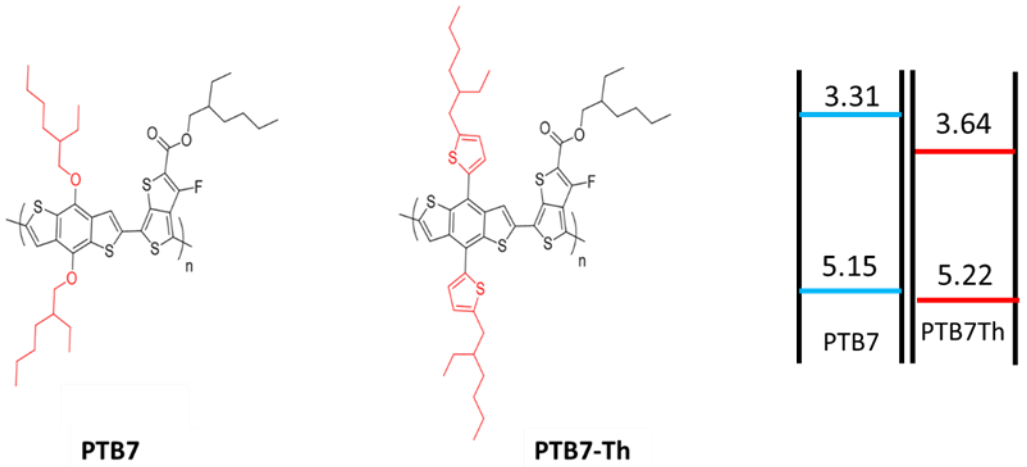

Fig. 4.6: Chemical structure and band level for PTB7 and PTB7-Th.

After deciding on PTB7 and PTB7-Th, basic DFT analysis was done on these polymers and bond strength of α C-H was found to be higher for PTB7 than PTB7-Th. Graduate student Satvik Shah in our lab, did all the calculations. For the calculations, the Spanish initiative for electronic simulations with thousands of atoms (SIESTA) method was employed, to simulate the electronic properties of organic materials. The ab initio density functional theory (DFT) with the SIESTA method utilized Troullier−Martins norm-conserving pseudopotentials, in a fully nonlocal form, with a basis set composed of multiple-ζ pseudo atomic orbitals. The exchange correlation functional used was the general gradient approximation (GGA) using the Perdew−Burke−Ernzerhof (PBE) parametrization of the exchange-correlation functional to treat the nonlocal exchange and correlation energies. Electronic structure, density of states, and total energies was obtained. The local orbital based SIESTA method allows computationally efficient

calculations in a multiprocessor environment. The structural relaxation is performed with a steepest descent algorithm to obtain the low energy configurations.

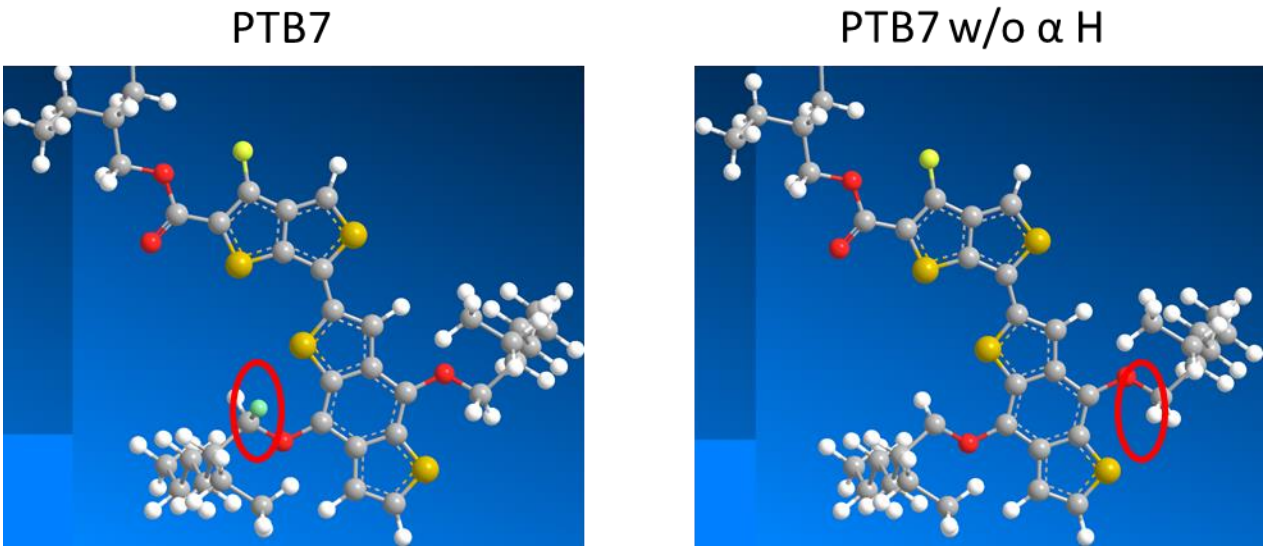

Fig. 4.7: 3D structure of PTB7 with and without α H, used for the DFT calculations of bond strength.

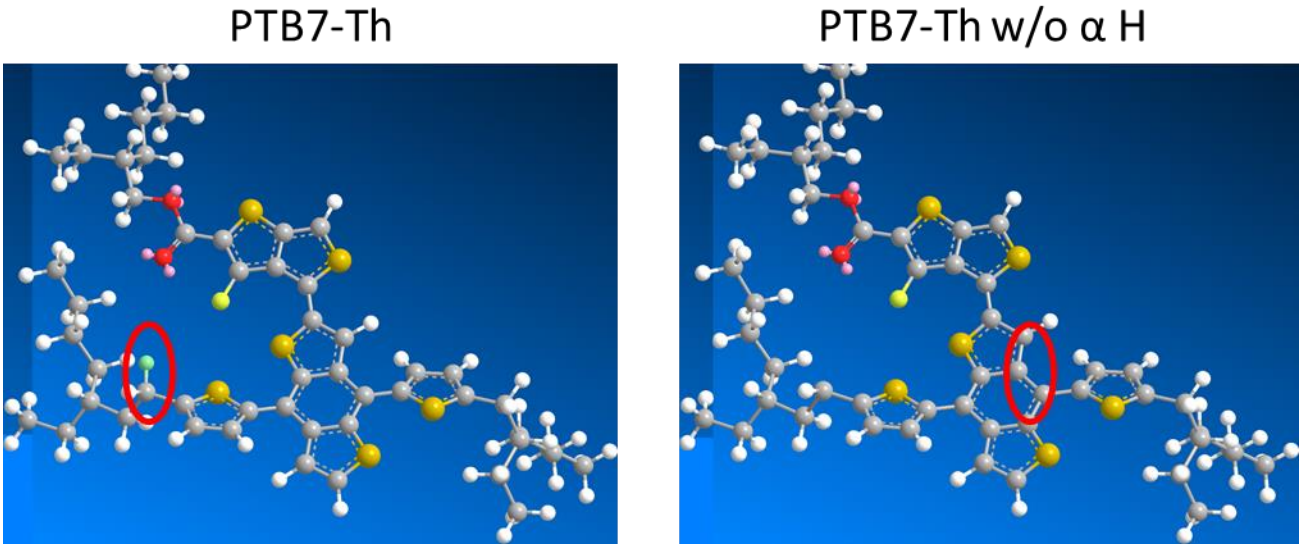

Fig. 4.8: 3D structure of PTB7-Th with and without α H, used for the DFT calculations of bond strength.

Fig. 4.7 and Fig. 4.8 show the 3D structures of PTB7 and PTB7-Th, with and without α-H used for calculations of the bond strength of α C-H bond. Energy of the α C-H bond was calculated

by calculating energy of polymer was calculated with and without (one) α-H. As shown in the Table 4.1, bond strength for α C-H bond in PTB7 was 0.1 eV stronger than the one in PTB7-Th. Also note that, C-O bond in PTB7 was found to be weaker than both α C-H bonds [42]. At this stage, we are not sure if the C-O bond will break first or if the C-H bond will break when exposed by light. Also just like in case of P3AT, numbers suggested from calculations are higher than usual energy of white photon and this raises some questions about possibility of breaking of α C-H bond by photon. However as reported by Street [3], white light might strong enough to break the bond by 1) two-step process or 2) using the energy released when H from the broken C-H bond moves to thiophene forming a metastable state.

Table 4.1: Bond strength of α C-H bond as calculated from DFT calculations for PTB7 and PTB7-Th

Bond Strength from DFT calculations in eV		
	PTB7	PTB7-Th
Energy of the polymer	-6353.51	-7454.99
Energy of the polymer after breaking C-H bond	-6348.05	-7449.62
Difference or energy required to break C-H bond	5.46	5.37

4.3: Device data

First a polymer only film was deposited on top of ITO/PEDOT substrate. Half area of the film was made available for absorbance measurements, whereas on the other half three circular dots of 0.106cm^2 MoOx/Al were deposited so that hole mobility in polymer only film can be measured using space charge limited current (SCLC).

Fig 4.9. Shows the absorbance in polymer only films of PTB7 and PTB7-Th. Film thicknesses were measured to be 60 and 55 nm respectively. PTB7-Th which has slightly higher bandgap absorbs further in near-infra-red region.

SCLC mobility was measured on the ITO/PEDOT/polymer/MoOx/Al hole only device. Details on mobility measurement can be found in chapter 3. Both polymers gave similar motilities of $1.1x10^{-4}$ $cm^2V^{-1}s^{-1}$ and $1.7\ x10^{-4}$ $cm^2V^{-1}s^{-1}$ respectively for PTB7 and PTB7-Th. These mobility values are similar to what has been reported in the literature for these polymers [40, 41].

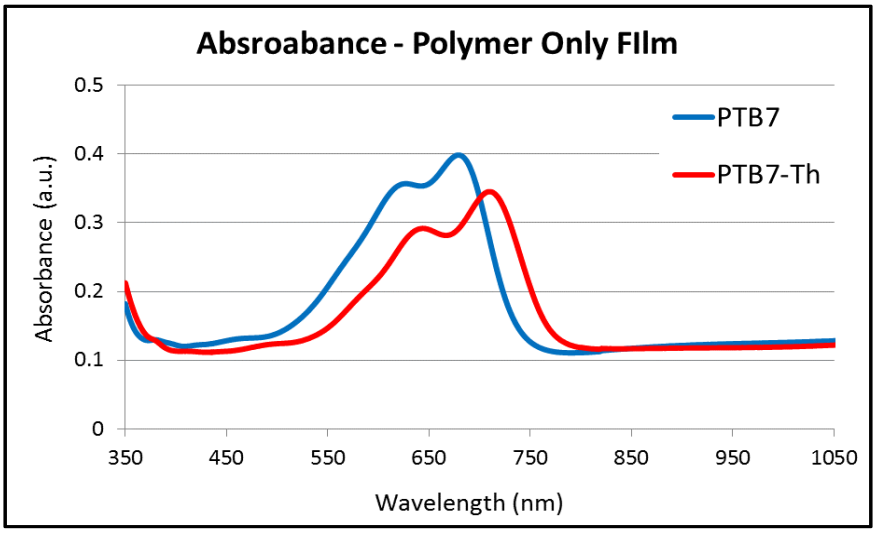

Fig. 4.9: Comparison of absorbance in PTB7 and PTB7-Th polymer only films as measured by Cary spectrometer.

Next p-i-n devices were made from these polymers in ITO/PEDOT/bulk heterojunction/Ca/Al architecture. Active layer was deposited by spin coating 1:1.5 weight ratio of polymer: $PC_{70}BM$ (hereon, in this chapter $PC_{70}BM$ is simply referred as PCBM) solution, 25 mg/ml in DCB with 3% DIO. 80-90nm film thickness was obtained by spin coating at 1000 rpm. Dried films were annealed at 110 °C for 30 mins. Details of fabrication recipe can be found in chapter 3.

UV-Vis absorption studies were also performed on bulk heterojunction device. The absorption spectrum showed the peaks corresponding to both PCBM and the polymer. PCBM absorption is centered around 350-450 nm, whereas both the polymers showed a marginal red shift

in absorption of 5 nm compared to neat polymer film. Similar to polymer only film, PTB7-Th absorbs roughly 20 nm further compared to PTB7.

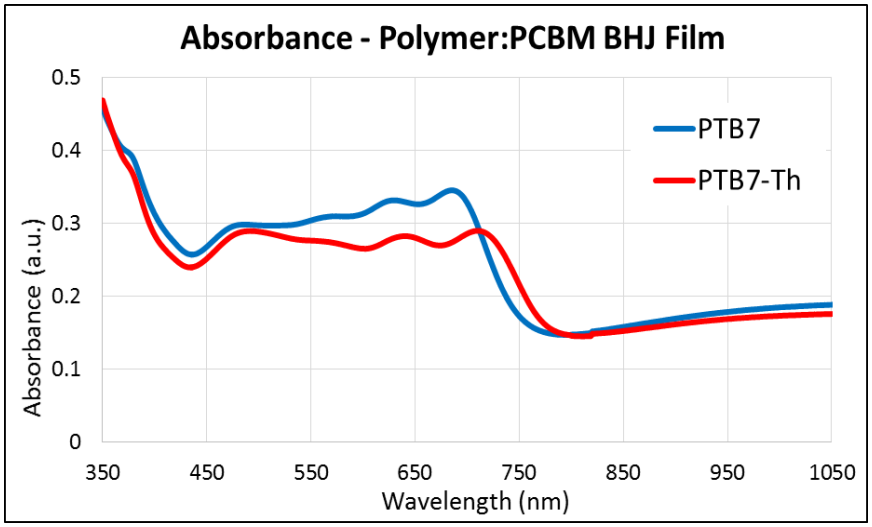

Fig. 4.10: Comparison of Absorbance for PTB7: PCBM and PTB7-Th: PCBM bulk heterojunction films as measured by Cary spectrometer.

Light IV was measured on both devices using ELH lamp (Calibrated to 1 Sun-100 mw/cm2). IV measured on 110 °C/30 min annealed device is shown in Fig. 4.11 and photovoltaic parameters are mentioned in the Table 4.2.

PTB7-Th has lower HOMO than PTB7 interface bandgap between PTB7-Th:$PC_{70}BM$ would be higher, which results in higher V_{oc} in PTB7-Th than PTB7. Note that, V_{oc} obtained are higher than the values reported in literature because of the thermal annealing step. Thermal annealing enhances the V_{oc} of the solar cell and might lead to small decrease in I_{sc} if device is being annealed at higher temperature than the optimum temperature. Previous work in our lab suggested that at 110 °C anneal there is little decrease in I_{sc}. However, I_{sc} obtained in these batches are slightly lower than literature reports and also the one obtained in our lab earlier. Lower performance of these devices can be due to multiple reasons, like quality of polymer, condition of

glovebox etc. Repeated attempts to get higher performance did not succeed and it was decided to proceed with these devices as such.

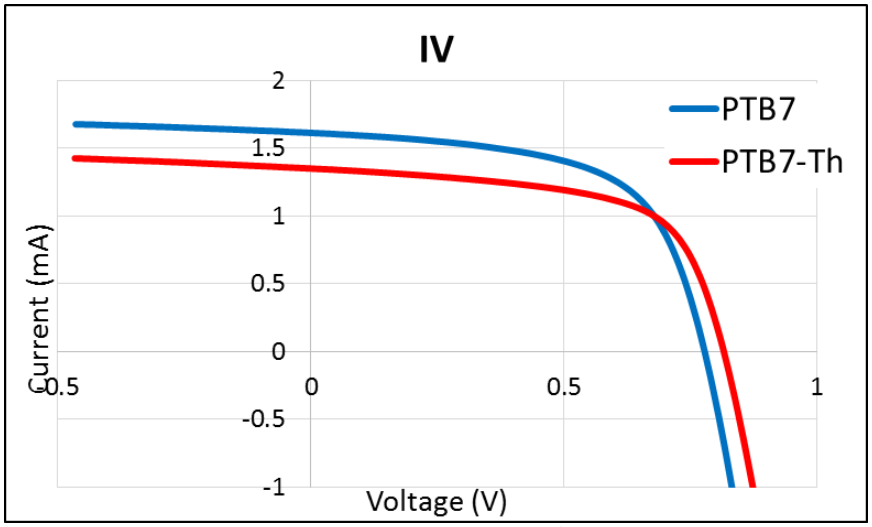

Fig. 4.11: Comparison of IV measured under 100mW/cm^2 solar spectrum for PTB7: PCBM and PTB7-Th: PCBM solar cells.

Table 4.2: Standard IV values on PTB7 and PTB7-Th devices.

Polymer	V_{oc} (V)	I_{sc} (mA)	FF	PCE
PTB7	0.778	1.61	61.13	7.23
PTB7-Th	0.816	1.35	62.58	6.51

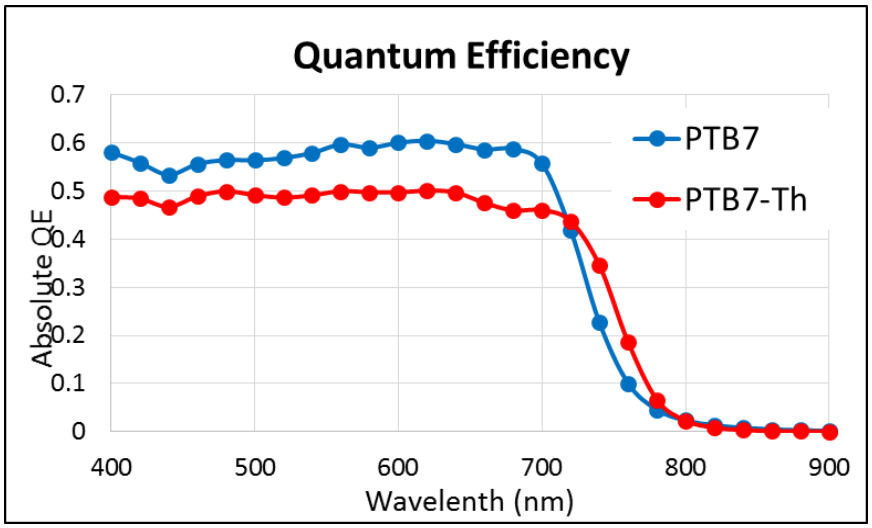

Fig. 4.12: Comparison of Absolute Quantum Efficiency measured for PTB7-PCBM and PTB7-Th: PCBM solar cells.

Quantum efficiency was measured on these devices using custom made photocurrent spectroscope (details in chapter 3). Integrated current from QE was within 10 % of current measured from ELH lamp. Again, PTB7-Th gives photocurrent from higher wavelengths for its higher absorbance in consonance with the already mentioned absorbance spectrum.

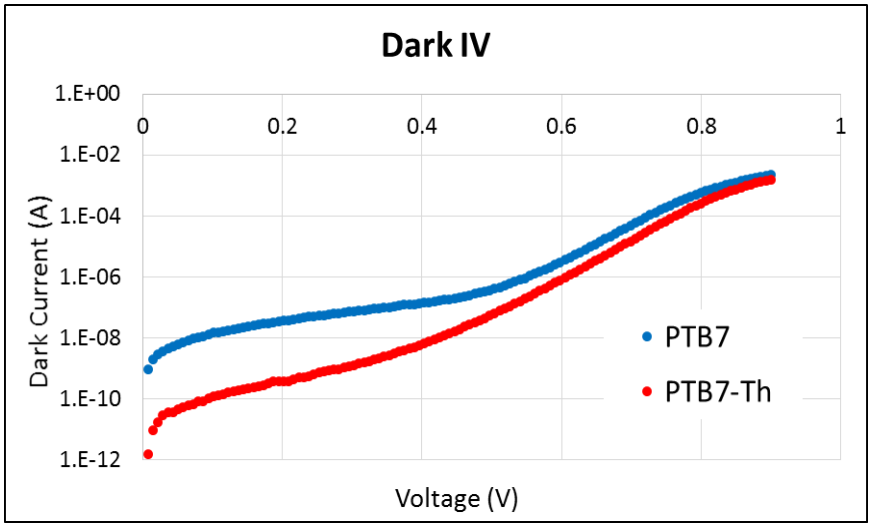

Fig. 4.13: Comparison of Dark IV measured for PTB7: PCBM and PTB7-Th: PCBM solar cell.

As mentioned in chapter 3, dark IV can be used to estimate defect density and also V_{oc} of the device. Unfortunately, many devices in these experiment had high shunt resistance and thus dark IV measurements cannot be analyzed properly. It can be seen that dark IV of PTB7 (shown below) has higher shunt resistance, and thus ideality factor (n) extracted for the low voltage region for the PTB7 gives values greater than 2.

Table 4.3: Dark IV parameters calculated from Dark IV measured on PTB7: PCBM and PTB7-Th: PCBM solar cell.

Polymer	I_{01}	n_2	I_{02}	n_2
PTB7	1.27E-09	3.68	2.27E-14	1.25
PTB7-Th	2.82E-12	2.02	2.62E-15	1.20

Dopant densities were also calculated by measuring CV at 10 Hz for both PTB7 and PTB7-Th devices. As it can be seen in the linear region of the CV in the figure below, that both devices have roughly similar dopant densities. Extracted values of dopant densities for PTB7 and PTB7-Th device were respectively 5.86 x 10^{16} /cm^3 and 5.23 x 10^{16} /cm^3. Density of states with respect to HOMO level of polymer was calculated using CF measurement. As it can be seen from following figure, both PTB7 and PTB7-Th have very similar defects in the bandgap.

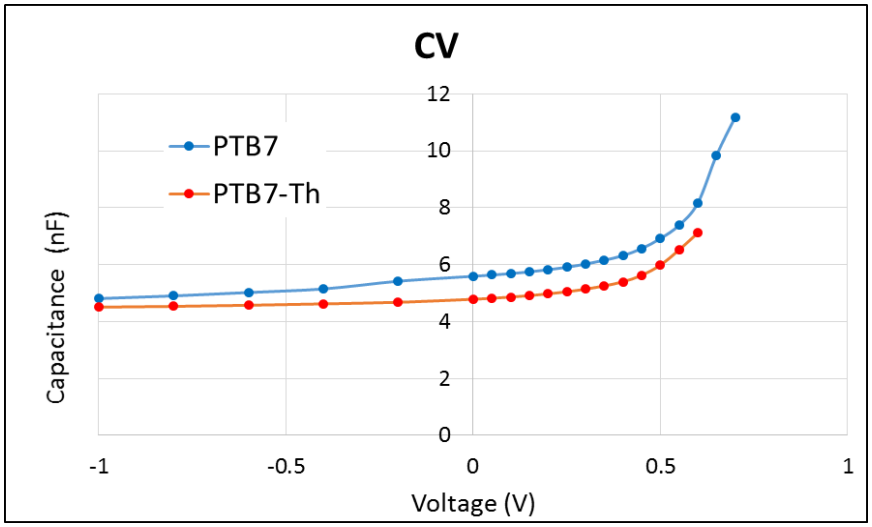

Fig. 4.14: Comparison of Capacitance vs Voltage measured for PTB7: PCBM and PTB7-Th: PCBM solar cells.

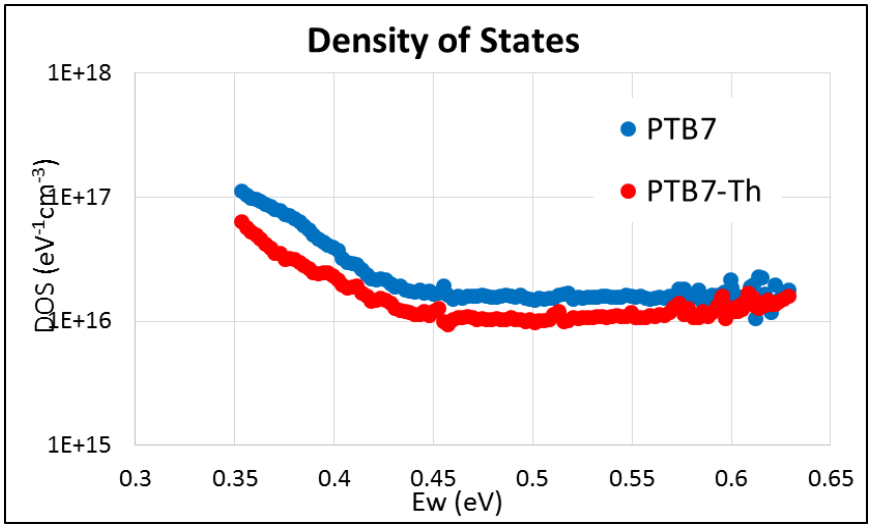

Fig. 4.15: Comparison of Density of States calculated for PTB7: PCBM and PTB7-Th: PCBM solar cells from capacitance spectroscopy.

Urbach energy for the polymer: PCBM bulk heterojunction can be calculated from photocurrent spectroscopy at energies lower than bandgap. Urbach energy for the tail states near HOMO level can be calculated by extracting the slope for normalized photocurrent below interface bandgap or around 1.3-1.4 eV (details in chapter 3). Both polymers Urbach energy for tails near HOMO from the slope of the subgap QE are found to be 33 and 35 meV.

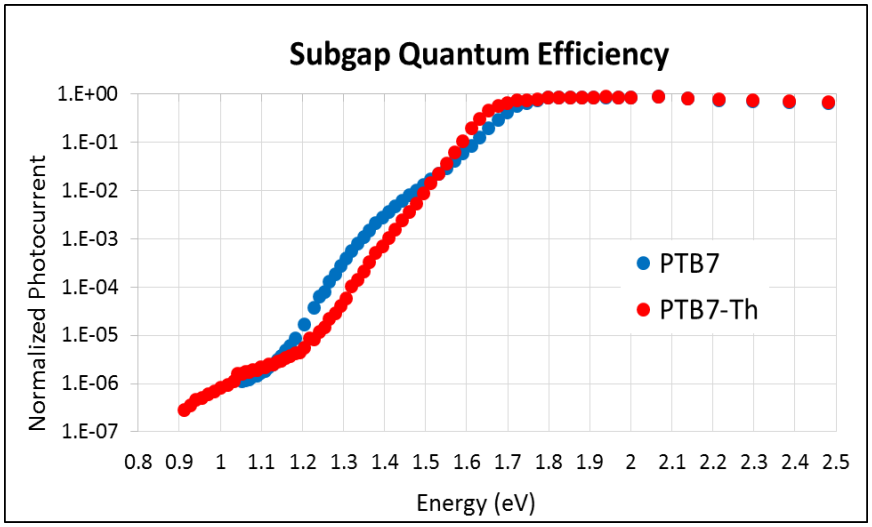

Fig.4.16: Comparison of Normalized Photocurrent measured for energy values below bandgap for PTB7: PCBM and PTB7-Th: PCBM solar cell.

All the date shown here, suggests that both PTB7 and PTB7-Th show very similar photovoltaic properties. PTB7-Th has slightly higher V_{oc} than PTB7 because of lower HOMO level. This also translates into further absorbance as already noticed. But overall power conversion efficiencies for devices made from both polymers are similar. Both devices show very similar dopant density and density of states. Similar Urbach energy again confirms the similarity of defect state profile in these polymers. Unfortunately dark IV could not be analyzed for high shunt resistance, which would have provided another verification for similar SRH recombination and hence trap density.

4.4: Light induced changes in film properties

Before going to device degradation, first effect of light exposure on film properties were measured. Polymer only and polymer: PCBM bulk heterojunction films of both polymers were exposed in 4X (400 mW/cm^2) ABET AM 1.5 solar simulated light for 1 day in the inert atmosphere of pure N_2 in environmental chamber (details mentioned in chapter 3). As it can be seen from fig. 4.17 below, there is no significant change in the absorbance of the polymer only or of polymer: PCBM bulk heterojunctions. Similar results have been reported before by our and other groups for different polymers. It should be noted that, if the lid of the environmental chamber is not tightly screwed, some air might leak in which would result in photo-bleaching of the film.

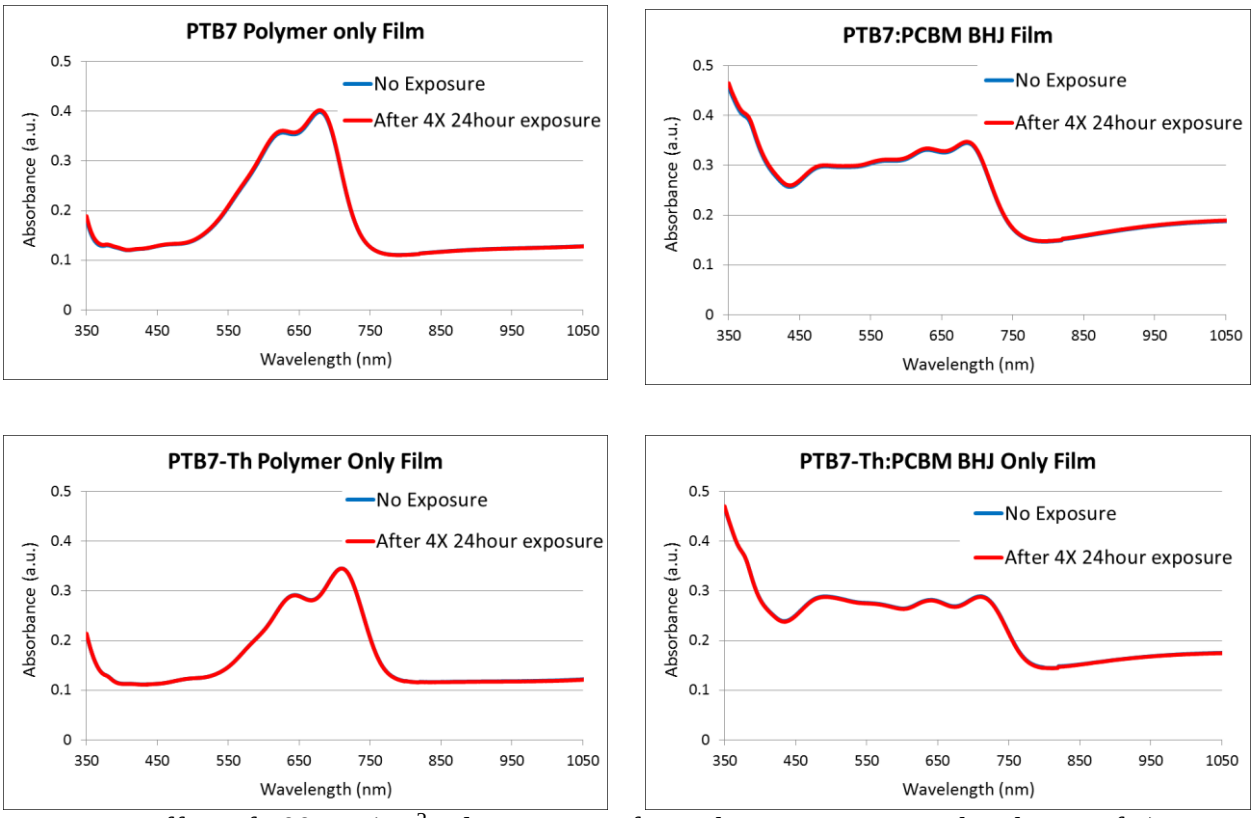

Fig. 4.17: Effect of 400mW/cm^2 solar spectrum for 24 hour exposure on absorbance of 1) PTB7 polymer only film 2) PTB7: PCBM bulk heterojunction 3) PTB-Th polymer only film and 4) PTB7-Th: PCBM bulk heterojunction.

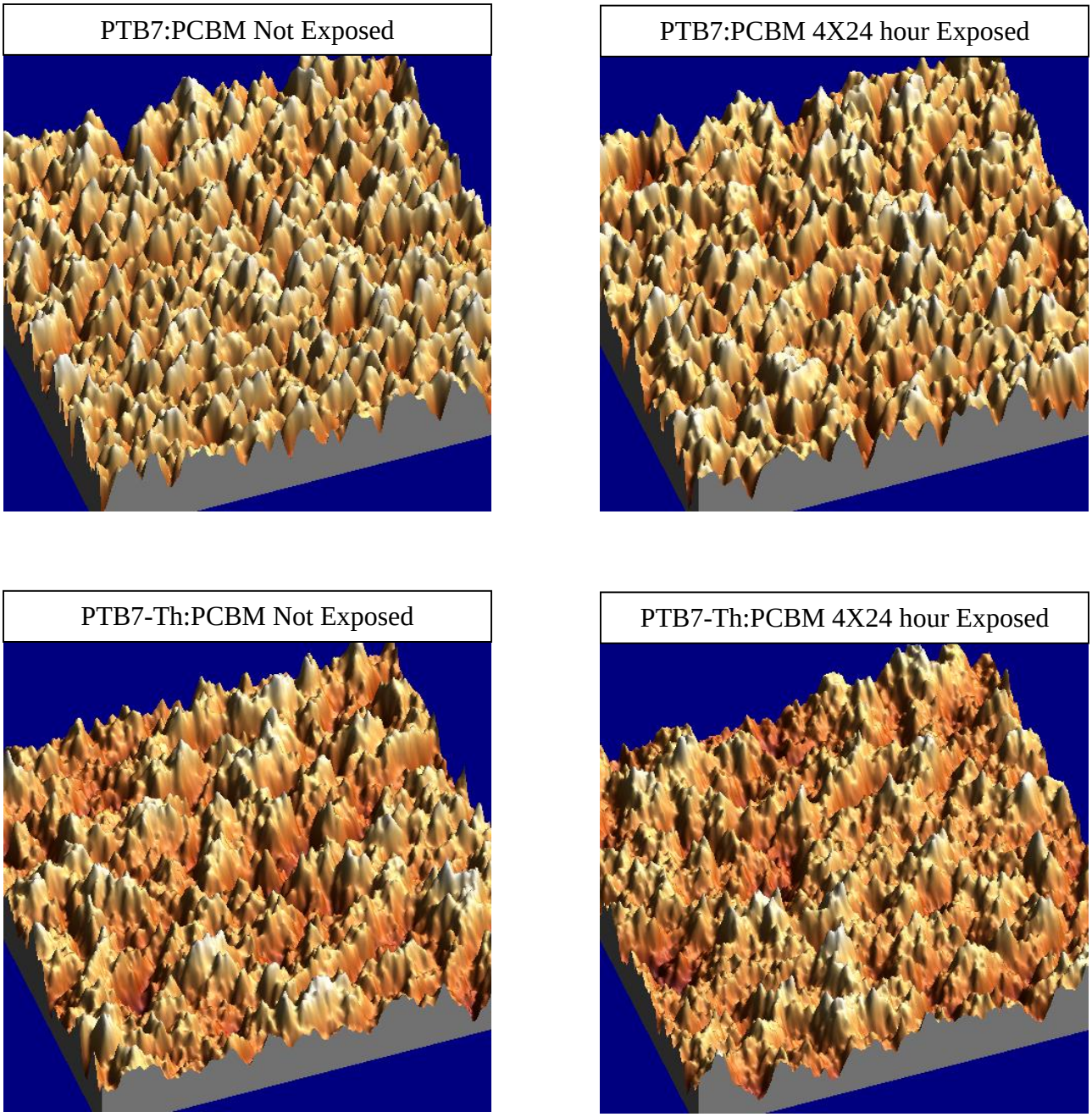

Fig. 4.18: Atomic Force Microscopy scan images for polymer: PCBM bulk heterojunctions before and after 4000mW/cm^2 solar spectrum exposure for 24 hours.

Film topography was measured using AFM on polymer: PCBM bulk heterojunction. Film topography would tell us if light exposure is resulting in further crystallization or phase separation between polymer and PCBM regions. However, as it can be seen from fig. 4.18, there is no significant change in film crystallization or phase separation because of 4X 24 hours light

exposure. No change in sharpness of the peak in absorbance also confirms that crystallization of the film is not affected by the light exposure.

Nanoscale software was used to calculate surface roughness values on these films. There is no significant change in surface roughness of the bulk heterojunction film before and after light exposure.

Table 4.4: Surface roughness calculated on the non-exposed and 400mW/cm^2 solar spectrum exposed for 24 hours polymer: PCBM films.

Surface Roughness (nm)		
	Non Exposed	Exposed
PTB7: PCBM	2.922	2.925
PTB7-Th: PCBM	3.699	3.903

Table 4.5: SCLC Hole mobilities measured on polymer and polymer: PCBM films before and after 400mW/cm^2 exposure for 24 hours.

SCLC Hole Mobility				
	PTB7	PTB7-Th	PTB7: PCBM70	PTB7-Th: PCBM70
Not Exposed	1.07E-04	1.71E-04	3.55E-04	4.10E-04
After Exposed	9.50E-05	1.10E-04	2.27E-04	3.44E-04

SCLC hole mobility values were also measured before and after exposure. Values are reported in the table below. In polymer only films, for both polymers there is very little degradation in hole mobility values before and after exposure. Hole only device was also made for polymer: PCBM bulk heterojunction to check if addition of PCBM leads to any significant change in mobility. Device was made in same architecture of ITO/PEDOT/polymer: PCBM/MoOx/Al. Note that mobility values measured in the case of bulk heterojunction are not accurate as the actual pathlength of the holes is not known in bulk heterojunction. However, qualitatively it can be said that, for both polymers there is very little degradation in hole mobilities before and after 4X 24 hour exposure.

4.5: Light induced changes in device performance

One dot in the 7.2% and 6.5% efficient devices, mentioned in section 4.2, were exposed to 400mW/cm^2 (4X) ABET AM 1.5 solar simulated source for 96 hours. Fig shows IV for both these cells before and after exposure. Both PTB7 and PTB7-Th cells showed degradation in device properties after light exposure. V_{oc} decreased more in PTB7, otherwise I_{sc}, FF and overall PTb7-Th degraded more than PTB7 as the DFT calculations suggest.

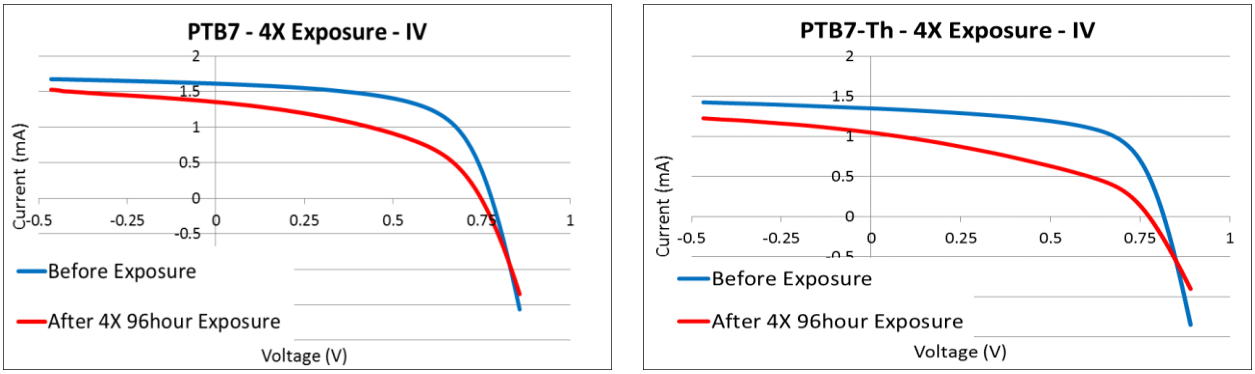

Fig. 4.19: Comparison of degradation in IV of PTB7: PCBM and PTB7-Th: PCBM solar cells after 400mW/cm^2 solar spectrum exposure for 96 hours.

Table 4.6: IV parameters for degradation of PTB7: PCBM and PTB7-Th: PCBM solar cells after 400mW/cm^2 exposure for 96 hours

Effect of 4X 96hour Photo-exposure								
	PTB7				PTB7-Th			
	V_{oc}(V)	I_{sc} (mA)	FF	PCE	V_{oc} (V)	Isc (mA)	FF	PCE
Before Exposure	0.78	1.61	61	7.23	0.82	1.35	63	6.51
After Exposure	0.73	1.35	46	4.26	0.78	0.90	39	2.61
Change (%)	6	16	25	41	5	33	37	60

The environmental chamber had in-situ Hioki LCR meter connected to it. CV was measured on both devices before and after exposure. In some devices, after exposure device became very shunty. Thus Q values were very low for 10 Hz measurement and hence here 100 Hz CV measurement data is shown. Dopant density calculated from these CV gives values of 6.06 x 10^{16} /cm^3 and 5.52 x 10^{16} /cm^3 for PTB7 device before and after exposure, whereas the PTB7-Th

device gave dopant densities of 4.75 x 10^{16} /cm^3 and 3.75 x 10^{16} /cm^3 before and after exposure. It can be calculated that in PTB7-Th device dopant density increased more than that in PTB7. It can be said that more increase in defect density would lead to more increase in SRH recombination and hence more degradation.

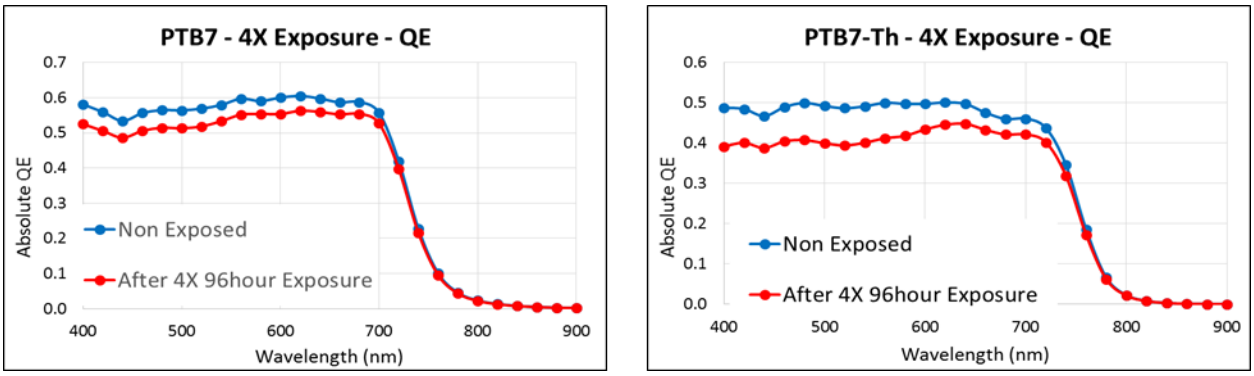

Fig. 4.20: Comparison of Absolute Quantum Efficiency before and after degradation of PTB7: PCBM and PTB7-Th: PCBM solar cells after 400mW/cm^2 exposure for 96 hours.

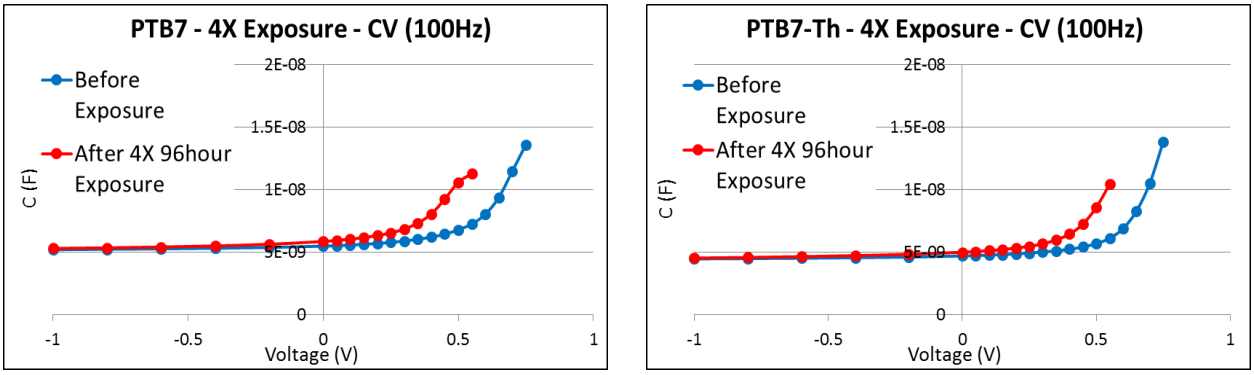

Fig.4.21: Comparison of CV measurement before and after degradation of PTB7: PCBM and PTB7-Th: PCBM solar cells after 400mW/cm^2 exposure for 96 hours.

Capacitance spectroscopy was also done before and after exposure. Density of states inside bandgap was estimated from capacitance spectroscopy. Fig. 4.22 shows density of states for both PTB7 and PTB7-Th before and after exposure. Data above 0.55 eV is noisy, but if we calculate increase in defect density at 0.55 eV, for PTB7 increase is 4 times, whereas for PTB7-Th increase is 4.5 times. Again supporting that increase in defect density is more in PTB7-Th device resulting in more photo-induced degradation.

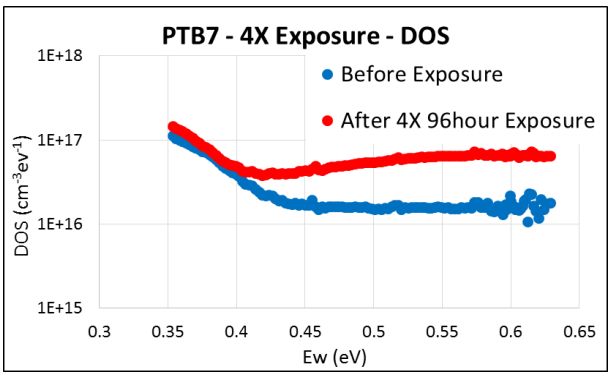

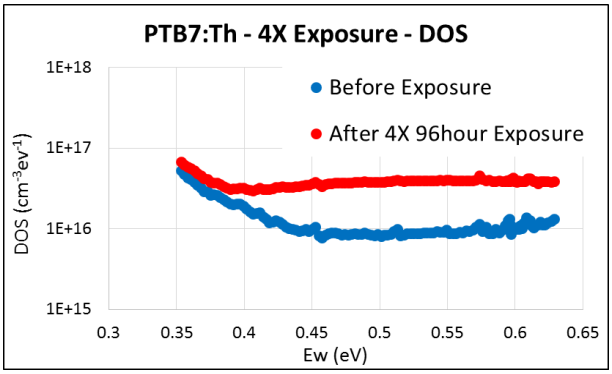

Fig. 4.22: Comparison of Density of States measured before and after degradation of PTB7: PCBM and PTB7-Th: PCBM solar cells after 400mW/cm^2 exposure for 96 hours.

4.6: Conclusion

In conclusion, in this work, two high efficiency polymers PTB7 and PTB7-Th were compared. Both polymers are based on benzodithiophene (BDT) based units. Both these polymers have low bandgap and thus deeper absorption, ideal LUMO level and high hole mobilities, ideal properties for donor material in organic bulk heterojunction photovoltaics. Optical/electrical properties such as absorbance, mobility etc of these two polymers are similar with PTB7-Th having 20nm deeper absorption and larger interface bandgap with $PC_{70}BM$. Devices made with $PC_{70}BM$ and these two polymers also show similar photovoltaic properties with efficiencies of about 7% in ITO/PEDOT/polymer: $PC_{70}BM$ BHJ/Ca/Al architecture. PTB7-Th has slightly higher V_{oc} for higher interface bandgap, but I_{sc} was found to be higher in PTB7. Defects in both polymer: PCBM system are similar with dopant density being 5.86 x 10^{16} /cm^3 and 5.23 x 10^{16} /cm^3 respectively for PTB7 and PTB7-Th. Unfortunately, dark IV data could not be analyzed as devices fabricated low shunt resistance.

Polymer only film and polymer: PCBM bulk heterojunction films did not show any significant change in absorbance when exposed to light in inert atmosphere. Hole mobility in both polymers showed a little degradation with exposure to light.

In terms of photovoltaic devices, it was found that devices made from PTB7-Th degraded faster than the ones made from PTB7. Dopant density and density of states calculations also suggest that in PTB7Th, increase in defects is more than that in PTB7. More defects lead to increased SRH recombination and hence reduced photovoltaic performance. Increase in recombination would decrease V_{oc}, I_{sc} and also FF. I_{sc} and FF data matched with the increase in defects, however V_{oc} data showed inconsistency, in this experiment V_{oc} decreased more for PTB7-Th.

Lower degradation in PTB7 matches with DFT calculations which suggests that α C-H bond is stronger in PTB7 than PTB7-Th. Though calculations suggest we used energies above 4eV, for degradation it can be expected that similar to Street's hypothesis [3], enough energy can be provided by 1) multiple photon excitations 2) energy released when hydrogen moves onto conjugation ring. DFT calculations also suggested that C-O bond in PTB7 has lower strength (3.5eV). Reason for breaking of C-H bond (which is a hypothesis) over C-O bond is not yet understood completely. However data from multiple devices show that PTB7 based cells are more stable than PTB7-Th based cells.

4.7: References

1. Bhattacharya, J., *Understanding the physics of degradation of polymer solar cells* (2013). *Graduate Theses and Dissertations.* Paper 13475.

2. Bhattacharya, J., et al., *Photo-induced changes in fundamental properties of organic solar cells.* Applied Physics Letters, 2012. **100**(19).

3. Street, R.A. and D.M. Davies, *Kinetics of light induced defect creation in organic solar cells.* Applied Physics Letters, 2013. **102**(4).

4. Street, R.A., J.E. Northrup, and B.S. Krusor, *Radiation induced recombination centers in organic solar cells.* Physical Review B, 2012. **85**(20).

5. Jorgensen, M., et al., *Stability of Polymer Solar Cells.* Advanced Materials, 2012. **24**(5): p. 580-612.

6. Peters, C.H., et al., *High Efficiency Polymer Solar Cells with Long Operating Lifetimes.* Advanced Energy Materials, 2011. **1**(4): p. 491-494.

7. Heumueller, T., et al., *Reducing burn-in voltage loss in polymer solar cells by increasing the polymer crystallinity.* Energy & Environmental Science, 2014. **7**(9): p. 2974-2980.

8. Dou, L.T., et al., *25th Anniversary Article: A Decade of Organic/Polymeric Photovoltaic Research.* Advanced Materials, 2013. **25**(46): p. 6642-6671.

9. Li, G., R. Zhu, and Y. Yang, *Polymer solar cells.* Nat Photon, 2012. **6**(3): p. 153-161.

10. Grossiord, N., et al., *Degradation mechanisms in organic photovoltaic devices.* Organic Electronics, 2012. **13**(3): p. 432-456.

11. Northrup, J.E., *Radiation Induced Hydrogen Rearrangement in Poly(3-alkylthiophene).* Applied Physics Express, 2013. **6**(12).

12. Manceau, M., et al., *Effects of long-term UV-visible light irradiation in the absence of oxygen on P3HT and P3HT:PCBM blend.* Solar Energy Materials and Solar Cells, 2010. **94**(10): p. 1572-1577.

13. Peters, C.H., et al., *The Mechanism of Burn-in Loss in a High Efficiency Polymer Solar Cell.* Advanced Materials, 2012. **24**(5): p. 663-+.

14. Data, V.L., et al., *Stability Of Organic Solar Cells.* 2012 Ieee International Reliability Physics Symposium (Irps), 2012.

15. Reese, M.O., et al., *Pathways for the degradation of organic photovoltaic P3HT : PCBM based devices.* Solar Energy Materials and Solar Cells, 2008. **92**(7): p. 746-752.

16. Reese, M.O., et al., *Photoinduced Degradation of Polymer and Polymer-Fullerene Active Layers: Experiment and Theory.* Advanced Functional Materials, 2010. **20**(20): p. 3476-3483.

17. Wu, H., et al., *Side chain modification: an effective approach to modulate the energy level of benzodithiophene based polymers for high-performance solar cells.* Journal of Materials Chemistry A, 2015. **3**(35): p. 18115-18126.

18. Cho, N., et al., *High-Dielectric Constant Side-Chain Polymers Show Reduced Non-Geminate Recombination in Heterojunction Solar Cells.* Advanced Energy Materials, 2014. **4**(10).

19. Zhang, S.Q., et al., *Side Chain Selection for Designing Highly Efficient Photovoltaic Polymers with 2D-Conjugated Structure.* Macromolecules, 2014. **47**(14): p. 4653-4659.

20. Wang, Y., et al., *Significant Enhancement of Polymer Solar Cell Performance via Side-Chain Engineering and Simple Solvent Treatment.* Chemistry of Materials, 2013. **25**(15): p. 3196-3204.

21. Cui, C. and W.-Y. Wong, *Effects of Alkylthio and Alkoxy Side Chains in Polymer Donor Materials for Organic Solar Cells.* Macromolecular Rapid Communications, 2016. **37**(4): p. 287-302.

22. de Villers, B.J.T., et al., *Removal of Residual Diiodooctane Improves Photostability of High-Performance Organic Solar Cell Polymers.* Chemistry of Materials, 2016. **28**(3): p. 876-884.

23. Manceau, M., et al., *Photochemical stability of [small pi]-conjugated polymers for polymer solar cells: a rule of thumb.* Journal of Materials Chemistry, 2011. **21**(12): p. 4132-4141.

24. Staebler, D.L. *Optically induced conductivity changes in amorphous silicon: A historical perspective*. in *Symposium on Amorphous and Microcrystalline Silicon Technology*. 1997. San Francisco, Ca.

25. Staebler, D.L. and C.R. Wronski, *Reversible conductivity changes in discharge-produced amorphous Si.* Applied Physics Letters, 1977. **31**(4): p. 292-294.

26. Staebler, D.L., *Stability of amorphous-silicon solar cells.* IEEE Transactions on Reliability, 1982. **31**(3): p. 281-284.

27. Dalal, V.L., et al., *Growth of high-quality amorphous-silicon films with significantly improved stability.* Applied Physics Letters, 1994. **64**(14): p. 1862-1864.

28. Biswas, R., B.C. Pan, and Y.Y. Ye, *Metastability of amorphous silicon from silicon network rebonding.* Physical Review Letters, 2002. **88**(20).

29. Branz, H.M. *Hydrogen diffusion in the hydrogen collision model of amorphous silicon metastability*. in *Symposium on Amorphous and Heterogeneous Silicon Thin Film - Fundamentals to Devices-1999 Held at the 1999 MRS Spring Meeting*. 1999. San Francisco, Ca.

30. Manceau, M., et al., *The mechanism of photo- and thermooxidation of poly(3-hexylthiophene) (P3HT) reconsidered.* Polymer Degradation and Stability, 2009. **94**(6): p. 898-907.

31. Abdou, M.S.A. and S. Holdcroft, *Mechanisms of photodegradation of poly(3-alkylthiophenes) in solution.* Macromolecules, 1993. **26**(11): p. 2954-2962.

32. Xia, Y., et al., *Alternating Narrow Band Gap Copolymers Derived from Indeno 1,2-b fluorene and Thiophene-cored-thieno 3,4-b pyrazine Derivatives-Synthesis, Characterization and Comparative Studies of Photochemical Stability.* Journal of Polymer Science Part a-Polymer Chemistry, 2011. **49**(13): p. 2969-2979.

33. Ye, L., et al., *Highly Efficient 2D-Conjugated Benzodithiophene-Based Photovoltaic Polymer with Linear Alkylthio Side Chain.* Chemistry of Materials, 2014. **26**(12): p. 3603-3605.

34. Lu, L.Y. and L.P. Yu, *Understanding Low Bandgap Polymer PTB7 and Optimizing Polymer Solar Cells Based on It.* Advanced Materials, 2014. **26**(26): p. 4413-4430.

35. Liao, S.H., et al., *Single Junction Inverted Polymer Solar Cell Reaching Power Conversion Efficiency 10.31% by Employing Dual-Doped Zinc Oxide Nano-Film as Cathode Interlayer.* Scientific Reports, 2014. **4**.

36. Duan, C., et al., *Conjugated zwitterionic polyelectrolyte-based interface modification materials for high performance polymer optoelectronic devices.* Chemical Science, 2013. **4**(3): p. 1298-1307.

37. Das, S., et al., *Correlating high power conversion efficiency of PTB7: PC71 BM inverted organic solar cells with nanoscale structures.* Nanoscale, 2015. **7**(38): p. 15576-15583.

38. Bundgaard, E. and F.C. Krebs, *Low band gap polymers for organic photovoltaics.* Solar Energy Materials and Solar Cells, 2007. **91**(11): p. 954-985.

39. Liu, C., et al., *Low bandgap semiconducting polymers for polymeric photovoltaics.* Chemical Society Reviews, 2016.

40. Liang, Y., et al., *For the Bright Future-Bulk Heterojunction Polymer Solar Cells with Power Conversion Efficiency of 7.4%.* Advanced Materials, 2010. **22**(20): p. E135-+.

41. Jiang, T., et al., *Random terpolymer with a cost-effective monomer and comparable efficiency to PTB7-Th for bulk-heterojunction polymer solar cells.* Polymer Chemistry, 2016. **7**(4): p. 926-932.

42. Shah, S. and R. Biswas, *Atomic Pathways Underlying Light-Induced Changes in Organic Solar Cell Materials.* Journal of Physical Chemistry C, 2015. **119**(35): p. 20265-20271.

CHAPTER 5

UNDERSTANDING THE PHOTOSTABILITY OF PEROVSKITE SOLAR CELL

5.1: Introduction

Perovskite solar cells have rapidly become a very promising technology for next generation photovoltaics. Power conversion efficiency of perovskite solar cells rose from less than 3% to more than 21% in mere 7 years [1-10]. Its efficiency is already comparable to that of the best thin film photovoltaics, and is only slightly lower than the commercially most commonly used crystalline silicon photovoltaics, with an easier and cheaper fabrication process [11].

With comparable efficiencies, the most important question for perovskite technology is, are the perovskite solar cells stable? Are they stable under various ambients? And more fundamentally, are they intrinsically stable under light exposure?

Perovskite solar cells have been reported to degrade rapidly in the presence of moisture [12-17]. Oxygen in presence of light has been shown recently to degrade perovskite solar cells [18]. With the understanding that encapsulation can solve the problem of ambient degradation almost completely, in this work we emphasized on the more fundamental question. Are the perovskite solar cells intrinsically photo-stable?

5.2: Literation review of perovskite solar cell photostability

Perovskite material has been reported to degrade very rapidly under moisture. Moisture rapidly degrades perovskite into PbI_2. Heterojunction layers in the complete device, like the hole

transporting layers Spiro-MeOTAD, P3HT, PTAA or electron transporting layers such as ZnO, PCBM and in some cases extra buffering layers like Al_2O_3, Cr_2O_3 can act as a protective shield for moisture and reduce the degradations [17, 19-21].

Perovskite layer is also known to be not so thermally stable [14, 22]. At around 100^oC, MAI perovskite starts to disintegrate to PbI_2 and MAI. FAI perovskite is more stable, but it also starts to disintegrate at around 125^oC. Over-layers can help in preventing this disintegration also. If the over layer blocks MAI vapors from escaping out, it would react with the PbI_2 forming the perovskite again.

Most of the work on stability of perovskites was focused on moisture or thermal stability, however as mentioned above, here we will only go over the reports on photo-stability of perovskite solar cells. There are many reports on light exposure without any encapsulation. However those reports are not included in this review as moisture component is also coming into play and it would be difficult to separate intrinsic instability from ambient instability. In this review the effects of light exposure on devices either encapsulated or kept in inert atmosphere are reported. We have also mentioned details of fabrication as they can have significant impact on the stability.

Bruschka et al. [4] in 2013 reported photostability results on encapsulated n-i-p device on their sequential liquid route to make the perovskite. In this device, PbI_2 was spin-coated on the top of mesoporous TiO_2 on FTO substrate in DMF. After drying, the sample was dipped in MAI in isopropanol solution, which converts PbI_2 to $CH_3NH_3PbI_3$ perovskite immediately. Isopropanol solvent is orthogonal to both PbI_2 and perovskite and thus it won't dissolve PbI_2 or the perovskite. Device was completed with spin-coating of spiro-MeOTAD hole transport layer and evaporation of gold contact. 15% efficiency cells with V_{oc} of 0.99 V, J_{sc} of 20 mA/cm^2, FF of 73% were achieved. These cells after encapsulation in Argon were exposed to 1 Sun intense white light LED

array for 500 hours at maximum power point. It is to be noted that there was no UV component in this LED array. No change was observed in J_{sc}, whereas V_{oc} and FF degraded similarly, leading to less than 20% decrease in PCE (Fig. 5.1 (a)). V_{oc} and FF degradation was linked to decrease in shunt resistance, and for no decrease in J_{sc} authors suggested that there was no photo-degradation in the perovskite material.

Leijtens et al. [23] in 2013 reported that replacing mesoporous TiO_2 with mesoporous Al_2O_3 improved photo-stability of the perovskite solar cell. They also showed that degradation in TiO_2 devices is mostly caused by UV component of solar spectrum. In this paper, perovskites were made by single solvent approach, where 3:1 molar ratio solution of $PbCl_3$: MAI in DMF was spin-coated on the top of mesoporous TiO_2 or Al_2O_3. Device architecture was n-i-p in FTO/compact-TIO_2/mesoporous-TiO_2 (Al_2O_3)/perovskite/spiro-MeOTAD/Au. These devices were encapsulated rudimentarily and exposed to 76.5 mW/cm^2 solar spectrum under open circuit conditions. In devices with mesoporous TiO_2 the efficiency decreased within few hours, when UV light was not filtered. V_{oc}, I_{sc} and FF decreased rapidly (Fig 5.1 (b)). It was suggested that upon UV light excitation holes in valence band recombine with adsorbed oxygen causing desorption and leaving positively charged trap states. Deep trapping at these oxygen vacancies in the TiO_2 leads to enhanced recombination and thus degradation. When UV filter was used devices showed stable V_{oc}, almost stable I_{sc} and some decrease in FF. Note this result (which is only for 5 hours) doesn't exactly match with the result shown in sequentially grown devices by Burschka et al. [4]. In devices with mesoporous Al_2O_3 current was almost stable for 500 hours, whereas voltage and FF dropped (Fig 5.2 (a)). It was suggested that the decrease in V_{oc} and FF was because of the oxygen desorption at the remaining TiO_2 or de-doping of spiro-MeOTAD.

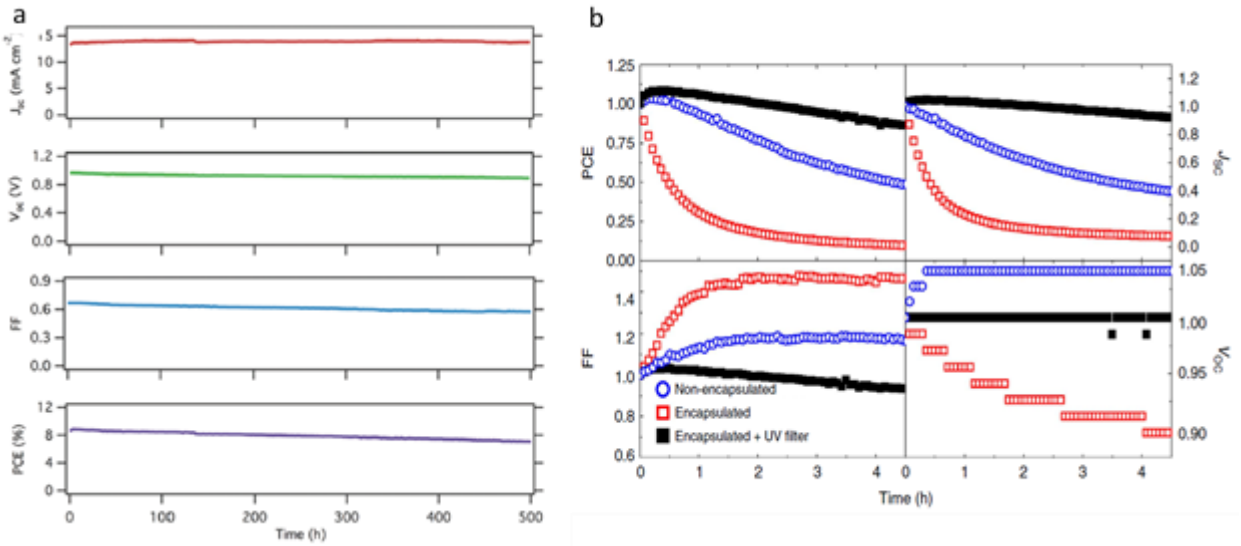

Fig. 5.1: In-situ exposure measurements reported by (a) Burschka et al. on encapsulated mesoporous-TiO_2/perovskite/spiro under LED light [4]and (b) Leijtens et al. on rudimentarily encapsulated meso-TiO_2/perovskite/spiro under 76.5mW/cm^2 solar spectrum in open circuit [23].

.Wojciechowski et al. [24] compared stability of perovskite on TiO_2 with that on C-60. On top of FTO substrate, compact TiO_2 or C-60 was deposited. Perovskite was then deposited on these planar layers in hybrid sequential route. PbI_2 was evaporated followed by spin-coating of MAI. Back contacts were made by spiro and gold. After encapsulation, 8.2% (TiO_2) and 10.4% (C-60) cells were exposed to AM 1.5 spectrum for 500 hours under maximum power point condition (Fig. 5.2 (b)). In a TiO_2 device I_{sc} decreased by more than half after initial increase, which could be due to desorption of oxygen. C-60 device, however showed quite stable I_{sc} over 500 hours of stability testing with less than 10% decrease. However, in C-60 device V_{oc} and FF decreased drastically leading to 45% decrease in PCE which might be because of gradual shunting and changes in spiro conductivity.

Ono et al. [25] also showed better stability with mesoporous Al_2O_3 than planar TiO_2 which was still better than mesoporous TiO_2. In this work, modified sequential liquid deposition process was used to deposit perovskite on FTO substrate coated by planar TiO_2 by itself or followed by

mesoporous TIO_2 or mesoporous Al_2O_3. Spiro-MeOTAD was deposited using chloroform for better ambient stability followed by gold evaporation. Mesoporous Al_2O_3 devices were 6.5% efficient, whereas mesoporous TiO_2 gave high efficiency of 12%. These devices were tested for stability under dry N_2 atmosphere at 65-70^oC under AM 1.5 solar spectrum at maximum power point (Fig. 5.3). Despite low efficiency mesoporous Al_2O_3, showed better stability than planar TiO_2 and mesoporous TiO_2. In mesoporous Al_2O_3 devices all V_{oc}, I_{sc} and FF were almost stable for 100 hours of exposure. In TiO_2 devices I_{sc} decreased significantly, whereas V_{oc} was almost stable.

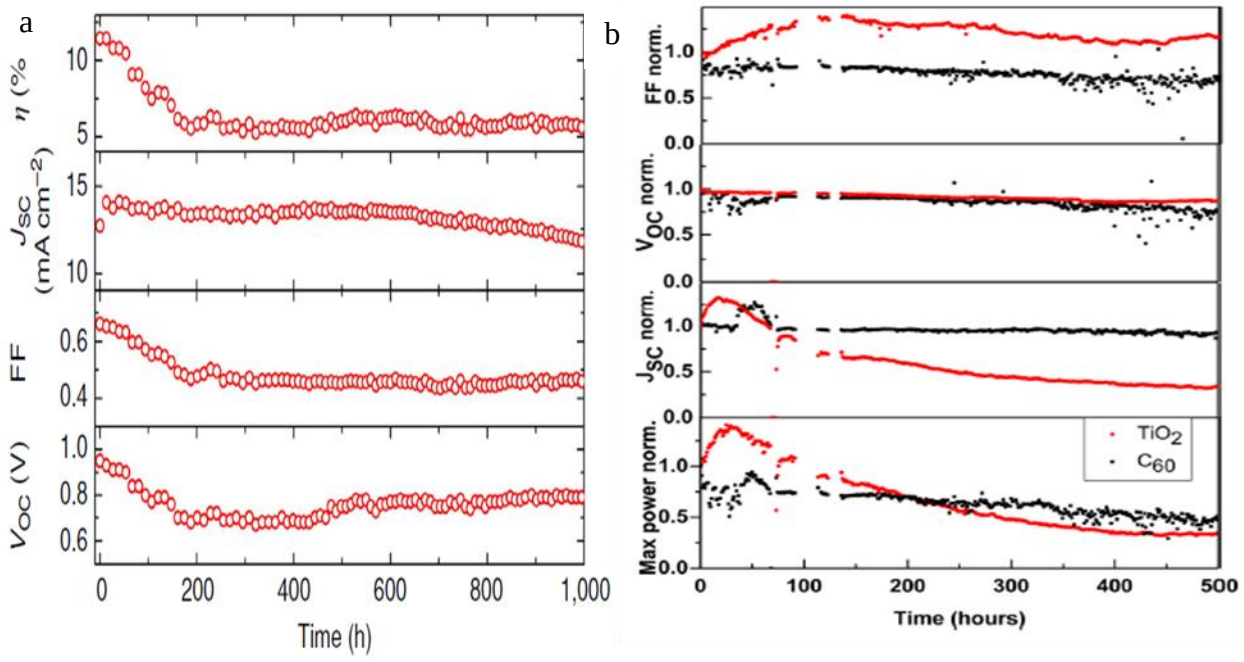

Fig 5.2: In-situ exposure measurements reported by (a) Leijtens et al. on rudimentarily encapsulated meso-Al_2O_3/perovskite/spiro under 76.5mW/cm^2 solar spectrum in open circuit [23] and (b) Wojciechowski et al. on encapsulated planar TiO_2 or C-60/perovskite/spiro at max-power point [24].

Apart from the work focusing more on electron transport layer, there are some reports on the effect of hole transport layer. Again many of the reports study the effect of both the light and ambient together. Guarnera et al. [26] showed that shunting through hole transport layer is also a

mechanism of degradation in perovskite solar cells. In this work, perovskites were formed on top of FTO/compact-TiO_2/mesoporous Al_2O_3 by single step 3:1 $PbCl_3$: MAI solution spin-coating. Back contact was made depositing spiro-MeOTAD, gold directly on the top of perovskite followed by thin layer of Al_2O_3 referred to as buffered hole transporting material. About 10% efficiency was achieved in both the cases. After encapsulation the devices were exposed to 100mW/cm^2 solar spectrum in open circuit condition. During the exposure, V_{oc} and I_{sc} both showed a much stable performance in the device with buffered hole transporting material. FF showed a similar decrease in both the cases. The measured dark IV showed that in the device made using buffered hole transporting material, increase in shunt resistance was far lower than that with only spiro. It was suggested that with light exposure metal diffuses inside perovskite layer increasing the shunt paths, and Al_2O_3 buffer layer avoids metal diffusion inside perovskite.

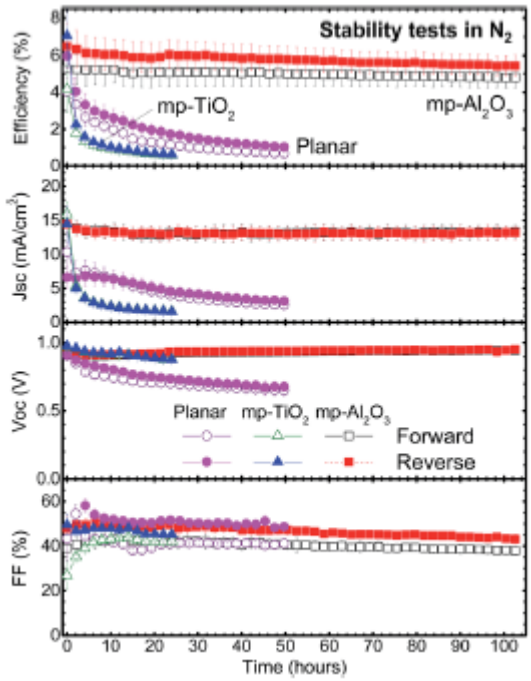

Fig. 5.3: In-situ exposure measurements reported by Ono et al. on planar-TiO_2 vs meso-TiO_2 vs meso-Al_2O_3/perovskite/spiro in dry-N_2 under AM 1.5 at max power point [25].

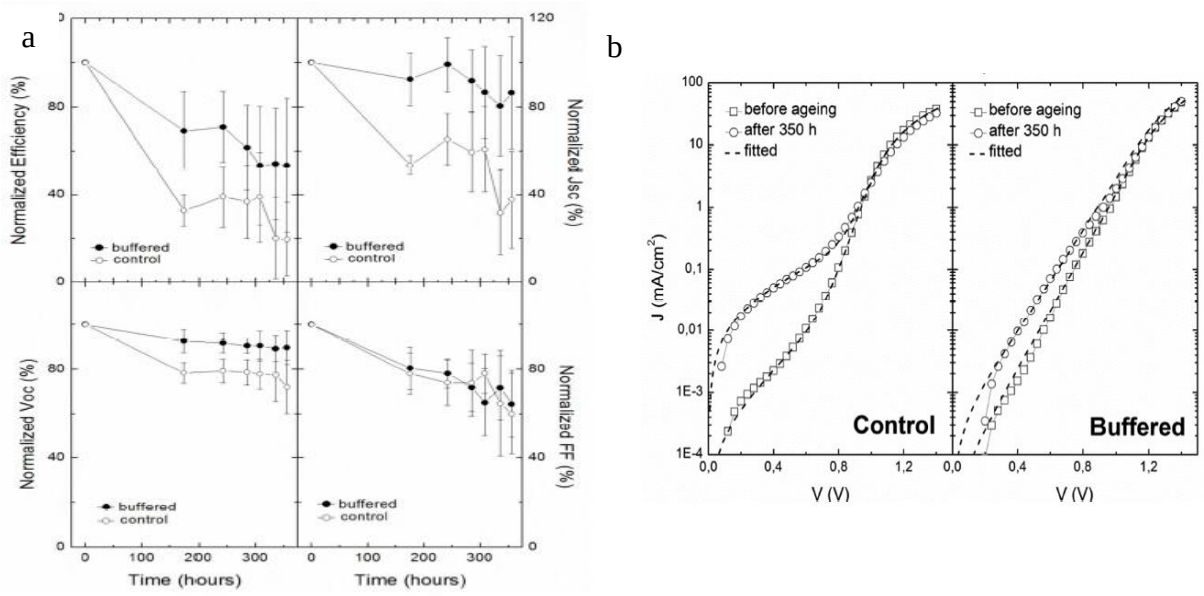

Fig. 5.4: In-situ exposure measurements and before and after exposure Dark IV measurements reported by Guarnera et al. on encapsulated meso-Al_2O_3/perovskite/Al_2O_3-spiro vs spiro under 100mW/cm^2 in open circuit condition [26].

Mei et al. [27] and Li et al. [28] showed a very stable perovskite solar cell under white LED light (without UV component). These perovskites were formed on top mesoporous TiO_2 with ZrO_2 scaffold. Back contact was made of a 10 µm thick graphite. PbI_2, MAI and 5-ammoniumvaleric acid (5-AVA) iodide was dropped from the back carbon contact which resulted in infiltration of $(5\text{-AVA})_x(MA)_{1-x}PbI_3$ perovskite in all three layers. Around 12% efficiency was reported in these perovskite solar cells. This hole-conductor free perovskite, fully printable perovskite device structure showed stable performance in white LED light (spectrum up to 450 nm). Even in outdoor exposure at hot and shiny Jeddah, Saudi Arabia the device retained much of its efficiency during 7 day exposure.

In all these photo-degradation reports on n-i-p devices, the degradation mechanism was identified for degradation of either electron transport layer or from metal diffusion at the hole transport layer and thus unfortunately intrinsic stability of perovskite solar cell could not be evaluated. The triple layer perovskite cell showed a very stable performance, thus suggesting that

there was no intrinsic degradation in perovskite active layer. However, that being only one-point data, more work should be done to completely understand the intrinsic degradation, if any, in a perovskite solar cell.

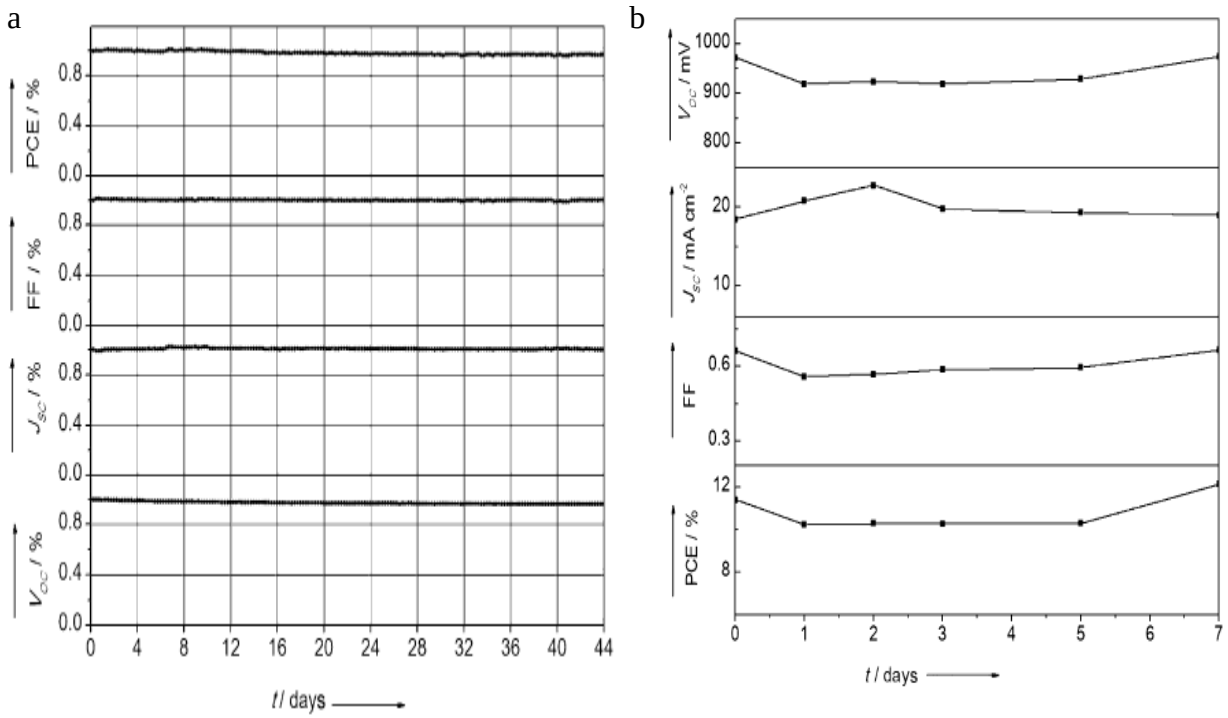

Fig. 5.5: In-situ exposure measurements reported on hole conductor free TiO_2/ZrO_2-perovskite/Graphite by (a) Mei et al.in white LED light (spectrum up to450nm) [27] and (b) Li et al.in outdoor sun light in Jeddah, Saudi Arabia [28].

Bag et al. [29] studied the kinetics of photo-degradation in p-i-n perovskite solar cell. These cells were prepared in ITO/PEDOT/perovskite/PCBM/Ca/Al architecture. Perovskite was prepared by two-step liquid deposition. First PbI_2 layer was spin-coated followed by spincoating of MAI or FAI or a mixture of MAI and FAI. The FAI only perovskite gave the highest efficiency of 8.9% whereas other two perovskites, MAI and MAI: FAI mixture, gave the best efficiencies of 13.6% and 13.3% respectively. Photo-degradation was also studied for MAI perovskite and MAI: FAI mixture perovskite. Device with mixed cation showed much stable behavior than only MAI perovskite. Perovskite with only MAI was exposed to different conditions 1) white LED exposure

(without IR component) 2) AM 1.5 exposure with IR filter 3) AM 1.5 exposure with air cooling 4) AM 1.5 exposure. The white LED exposure caused the least degradation, AM 1.5 with IR filter degraded more than white LED exposure, but less than AM 1.5 with air cooling. AM 1.5 without any cooling degraded the most. It was suggested that apart from light, degradation was thermally activated and thus device degraded more with temperature.

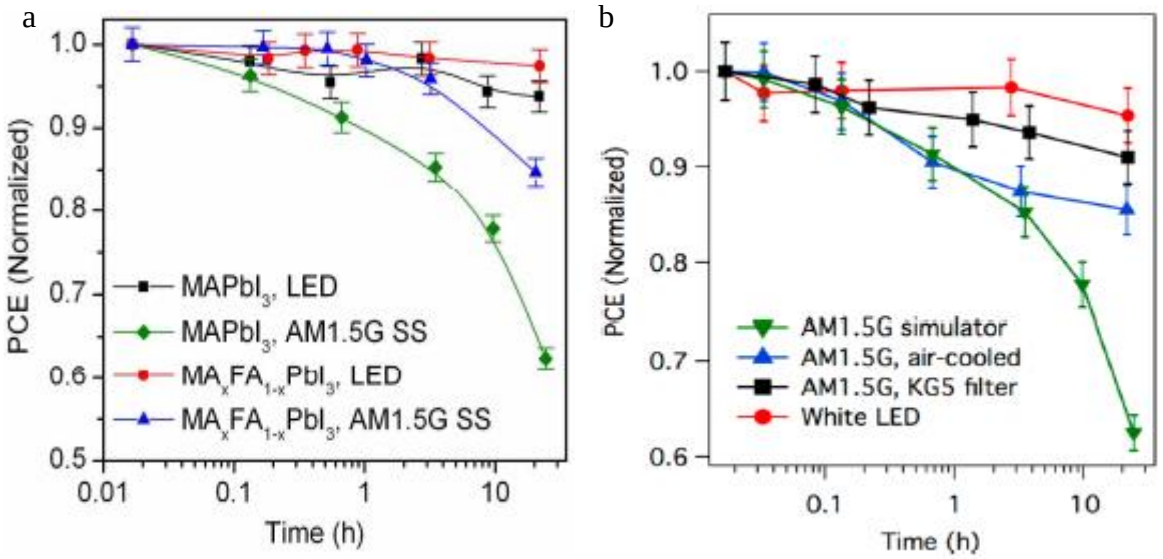

Fig 5.6: In-situ exposure measurements reported by Bag et al. on (a) PEDOT/perovskite with different cation/PCBM under white LED or solar simulator and on (b) PEDOT/MAI Perovskite/PCBM in different light/cooling conditions [29].

device condition	J_{SC} (mA·cm^{-2})	V_{OC} (V)	FF (%)	η (%)	R_s (Ω·cm^2)	R_{sh} (kΩ·cm^2)
Sample 1, as prepared	18.85	0.865	70.2	11.45	5.8	0.857
After 70 h in light	8.66	0.929	58.1	4.68	11.8	0.328
After 15 min in dark	12.67	0.851	62.8	6.78	9.2	0.330

Fig. 5.7: Degradation and recovery when kept in dark reported by Bag et al. on PEDOT/perovskite/PCBM device when exposed under solar simulator [29].

In the same paper, it was also reported that when illuminated devices were kept in dark, the device recovered. From the Fig. 5.7, it can be seen that, during degradation, I_{sc} and FF decreased significantly (54% and 17%) where as there is increase in V_{oc} (7%). After small time in dark, I_{sc} recovered back by 21%, FF by 7%, whereas V_{oc} dropped below initial V_{oc}. This result was

very different from other results, especially the recovery in the device performance was very intriguing.

Around all this work, the anomalous nature in perovskite solar cells is also discovered and is under intense research for complete understating.

5.3: Anomalous behavior in perovskite solar cell

5.3.1: IV hysteresis

Rapid progress in perovskite solar cell efficiencies has resulted in a race to achieve higher efficiencies. In such a competitive atmosphere, it took some time to notice fundamental anomalies in the behavior of perovskite solar cells. One very unfortunate thing that has happened is that observations which are not common to classical photovoltaics or which are not easy to understand are mostly downplayed. However, some anomalies have now been accepted by the community and the research is underway to completely understand the reasons behind the anomaly and the techniques to solve the problem.

One anomaly is hysteresis in light IV measurement. This phenomenon has been widely reported and is now under thorough research [30-48]. Hysteresis observed in perovskites is 1) dependent on the previous bias conditions before the sweep 2) sweep direction and 3) sweep rate and also 4) voltage range. This kind of hysteresis can be called rate-dependent hysteresis.

Fig. 5.8(a) shows different IV values obtained for a perovskite solar cell when measured in different directions and with different sweep rates [30]. Here devices were made in n-i-p architecture on three different substrates 1) planar TiO_2 2) mesoporous TiO_2 3) mesoporous Al_2O_3. Devices made on mesoporous TiO_2 showed lower hysteresis which decreased with increase in thickness of mesoporous layer. Kim et al. [33] also showed similar results that hysteresis decreases

with increase in thickness of mesoporous TiO_2 layer or decrease in perovskite capping layer thickness. For mesoporous Al_2O_3 device also hysteresis is present and is more evident than that on mesoporous TiO_2. In all these three devices, hysteresis was more pronounced when the sweep rate was decreased. Higher hysteresis in perovskite solar cells with a thick perovskite capping agent (as in case of Snaith et al. [30]) and without any capping agent but with very thin perovskite layer covering mesoporous TiO_2 (as in case of Dualeh et al. [47]) and also the reduced hysteresis with thicker mesoporous layer, suggests that hysteresis depends on fabrication conditions or more specifically pathlength that charge carriers need to travel before reaching the transport layers.

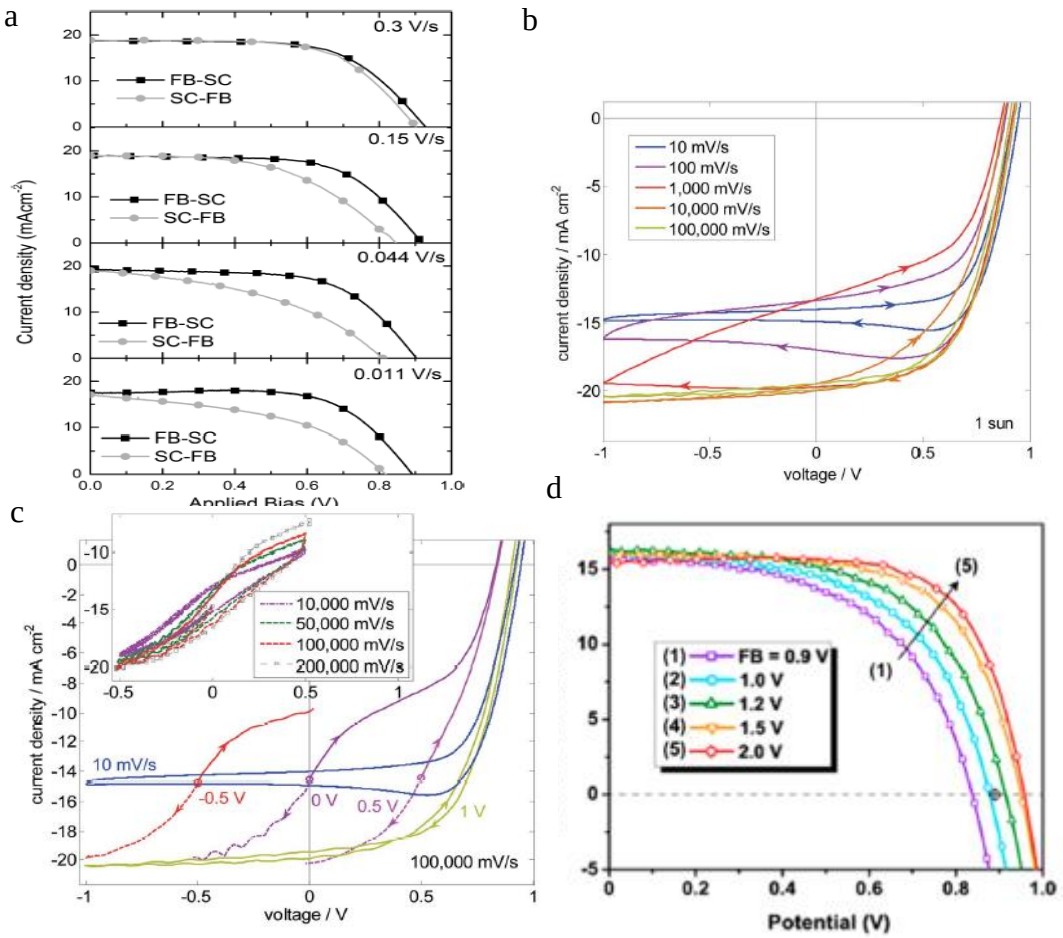

Fig 5.8: Hysteresis reported when IV is swept at (a) different directions [30] (b) different sweep rates [31] (c) different pre-biasing conditions [31] (d) different starting voltage [48].

Fig. 5.8(a) and Fig. 5.8 (b) show huge hysteresis when IV is swept at different rates. Devices in Fig. 5.8 (b) [31] were also n-i-p devices made using sequential liquid deposition on top of mesoporous TiO_2 scaffold.

Fig. 5. 8(a) and (b) suggest that device efficiency is higher when IV is swept from high to low bias than when it is swept from low to high bias. It also shows that device efficiency for low to high bias sweep further decreases when sweep rate is decreased, whereas device efficiency for high to low sweep is same, or increases slightly when sweep rate is decreased. It should be noted that Dualeh et al. [47] suggested opposite result to the one reported by Snaith et al. [30] that for low to high bias sweep efficiency increases with decrease in sweep rate, and for high to low it decreases with decrease in sweep rate, which is being considered an exception so far.

Fig. 5.8 (c) shows very different IV values have been obtained depending on the pre-biasing condition of the device [31]. In this experiment, same device as mentioned in Fig. 5.8(b) was pre-biased at -0.5, 0, 0.5 and 1 V for 30 seconds, and the IV was swept very fast. Sweep rate was chosen fast so as to avoid any hysteresis during sweep or any non-electronic slower effects. It has been noted that very fast sweep rates (more than 10,000mV/s in case of these devices) should also be avoided as they would induce electronic displacement current due to limited RC time constant of device and measurement circuit. Results from different pre-biasing conditions show if device is pre-biased at higher bias before sweep, device shows higher efficiency than when it is pre-biased at lower temperature

Fig. 5.8 (d) shows different IV measurements when voltage range of the sweep is changed [48]. This IV was also measured on TiO_2/perovskite/spiro device. The authors of this paper have done a good job of mentioning things in detail. It is mentioned that the device was preconditioned at high positive bias under illumination for 2 seconds before measuring IV from high to low bias.

This result suggests that the device would give higher efficiency if high to low IV sweep is started from a higher value.

To pinpoint origin of hysteresis, n-i-p devices were made without TiO_2 and hole transport layer (directly on top of FTO, and direct connection with gold) [30]. This device showed severe hysteresis, suggesting that hysteresis is not only because of transport layers. Also an increase in severity suggested that hysteresis depends on the contact layers or more specifically the contact resistance between perovskite and charge transfer layers.

Ip et al. [46] and Tao et al. [49] showed that adding a thin layer of PCBM on the top of planar TiO_2 reduced the hysteresis in the device (Fig. 5.9). Wojciechowski et al. [24] showed reduced hysteresis by replacing TiO_2 by C-60. Better electron extraction in PCBM, C-60 is thought to be the reason for reduced hysteresis.

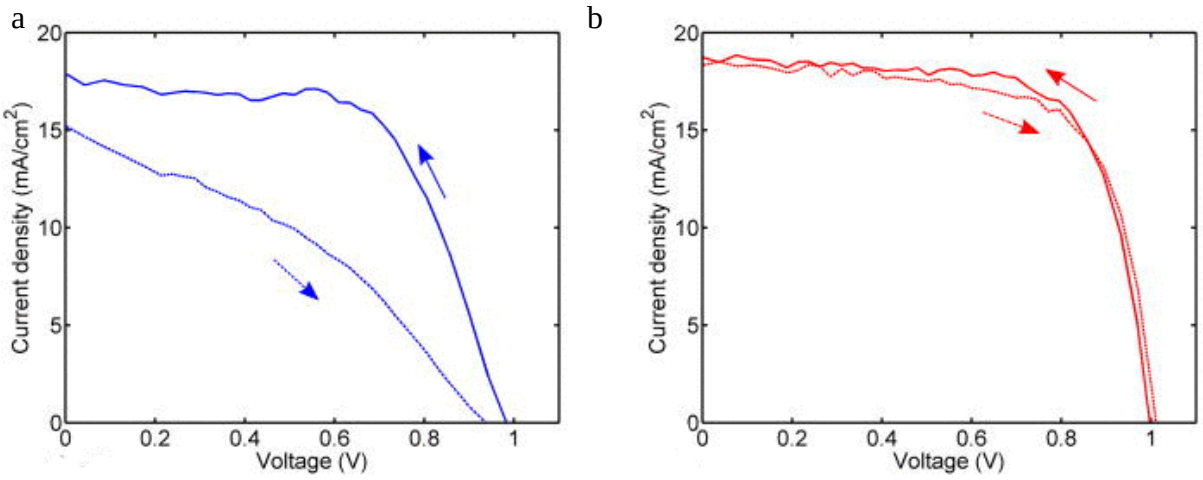

Fig 5.9: Hysteresis in IV measurements reported by Ip et al. on perovskite solar cells when (a) TiO_2 vs (b) PCBM is used as electron transport layer [46].

Kim et al. [33] showed that hysteresis also depends on the quality of the perovskite film. Perovskite films grown on top of mesoporous TiO_2 in three different sequential liquid fabrication conditions gave different grain sizes of perovskite films. It was shown that perovskite film with lower grain size has worst hysteresis (Fig. 5.10).

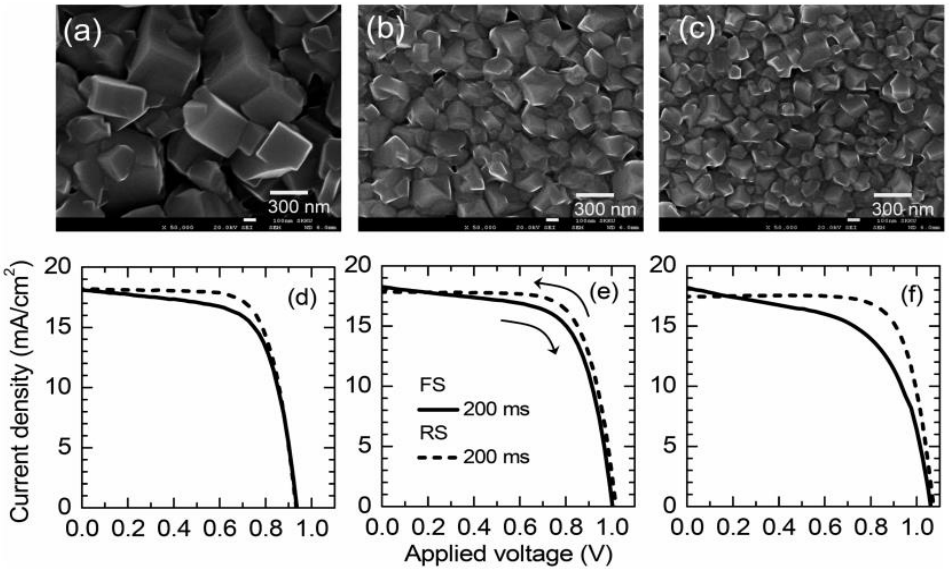

Fig. 5.10: Hysteresis in IV measurements reported by Kim et al. on different grain sized perovskites grown in TiO_2/perovskite/spiro architecture [33].

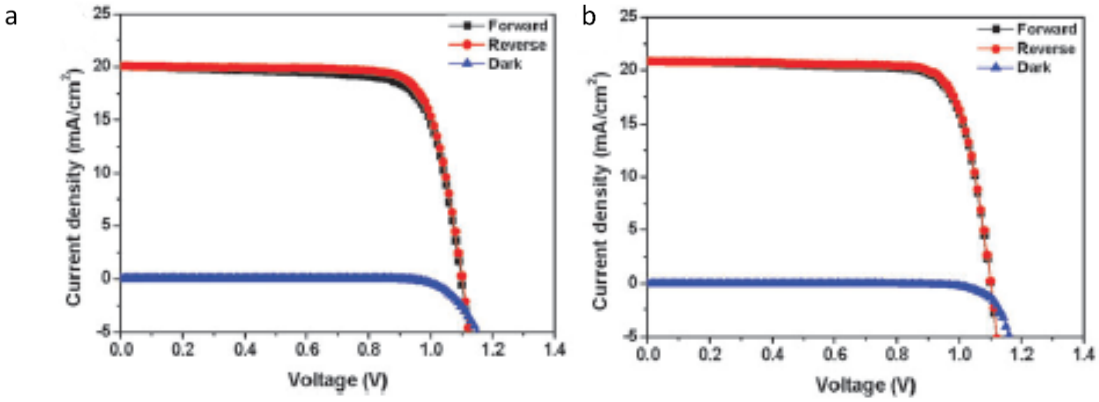

Fig 5.11: Hysteresis in IV measurements reported by Heo et al. on (a) PEDOT/perovskite/PCBM p-i-n architecture vs (b) planar-TiO_2/perovskite /PTAA n-i-p architecture [39].

Devices made in p-i-n architecture have usually shown much lower hysteresis than the n-i-p ones. Heo et al. [39] reported ITO/PEDOT/perovskite/PCBM/Au and FTO/planar-TiO_2/perovskite /PTAA/Au devices, where a dense perovskite was deposited in a single solution step using HI as an additive in the solution. Hysteresis was measured by measuring IV with a sweep rate of 10mV/200ms. The planar-TiO_2 device here showed far lesser hysteresis than the

other reports on device made on planar-TiO_2, which was ascribed to the denseness of perovskite. It was suggested that for the poor electron extraction in TiO_2, electron and hole extraction fluxes would not balance and that would result in hysteresis. It was also mentioned that in mesoporous devices, because of increased surface area, electron and hole flux would balance better than for the planar device. p-i-n device showed much lower hysteresis and it was suggested that the higher electron extraction in PCBM and thus balanced electron and hole flux results in lower hysteresis (Fig. 5.11).

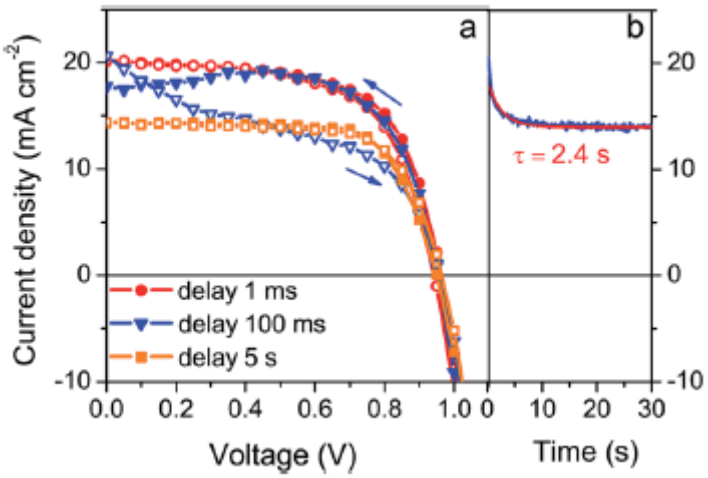

Fig. 5.12: Hysteresis in IV measurements when measured at different sweep rates reported by Unger et al. [32].

Unger et al. [32] reported dependence of hysteresis on scan rate. Hysteresis was measured on mesoporous TiO_2 based solar cells, which are reported to have higher hysteresis. This device showed significant hysteresis when sweep rate was 500mV/s (delay = 100ms). However, the same device did not show any hysteresis when measured at very fast rate of 20V/s (delay=5s) or at very low rate (delay=10mV/s).

All these results on hysteresis can be summarized as shown in the Fig. 5.13.

1) (a) High to low sweep gives higher efficiency than low to high sweep.
   (b) Slowing down sweep rate increases efficiency for high to low sweep, whereas it decreases efficiency for low to high sweep.
   (c) Pre-biasing at higher bias gives higher efficiency.
   (d) For high to low sweep rate, efficiency is higher when starting voltage is higher.

2) (a) n-i-p device show higher hysteresis than p-i-n device
   (b) planar n-i-p devices show higher hysteresis than mesoporous n-i-p devices
   (c) planar n-i-p device with TiO_2 contact show higher hysteresis than planar n-i-p device with C-60 or PCBM as electron extraction layer

3) (a) Perovskite film with smaller grains show higher hysteresis

4) Amount of hysteresis can depend on the sweep rate. One might not see hysteresis at very fast or extremely slow sweep rates. And the value of sweep rate where such changes are observed changes from device to device.

Fig. 5.13: Summary of reported hysteresis in perovskite solar cells.

5.3.2: Dark IV Hysteresis

Apart from hysteresis in IV measured under light, we in our lab have observed hysteresis even in dark IV. IV was measured with absolute certainty of zero light leakage. Fig. 5.14 shows results of dark IV measured in different scan directions and different starting points for a single step liquid-deposited p-i-n device on the top of NiO_x. When dark IV was measured from zero voltage to high bias, the resultant dark IV curve looked similar to the classical double diode curve. However, when dark IV was measured from high bias to low bias, the device current direction change point shifted towards higher voltage, suggesting that there is some leakage current at absolute zero, which flows in the reverse direction. When dark IV was started from a value lower

than zero bias, surprisingly absolute minimal current point in the dark IV shifted towards the left to the negative bias values.

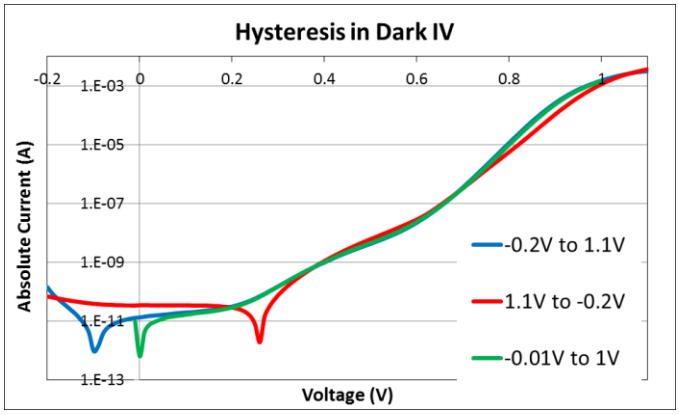

Fig 5.14: Hysteresis in Dark IV measured on NiO_x/perovskite/PCBM device at our lab.

5.3.3 External field / photovoltage induced poling in device

Another interesting anomaly that was observed in the perovskites was the switching behavior of symmetric contact devices. Xiao et al. [50] reported photocurrent switching mechanism in perovskites. Here the perovskite layer was sandwiched between two similar work function contacts. Xiao et al. used ITO/PEDOT/perovskite/Au architecture. The device was scanned from negative to positive bias and from positive to negative bias in the presence of light. Even without any charge selective contacts, the device showed solar cell IV-like behavior with respectable V_{oc} and I_{sc}. Surprisingly however, when the device was scanned from negative bias to positive bias, negative V_{oc} and negative I_{sc} was observed. In Fig. 5.15 (a) from Xiao et al., IV was scanned between +2.5V and -2.5V at 0.14V/s. V_{oc} was measured just after positive and negative poling of the device and similar results were found for more than 750 opposite poling. It was also found that once the device is poled in one direction, that poling was stable when device is kept in dark, unless opposite field is applied on the device. It was also observed that for larger grain size, it was difficult to switch the device than for the small-grain device.

Zhao et al. [34] showed similar results for ITO/PEDOT/perovskite/MoOx/Al devices.

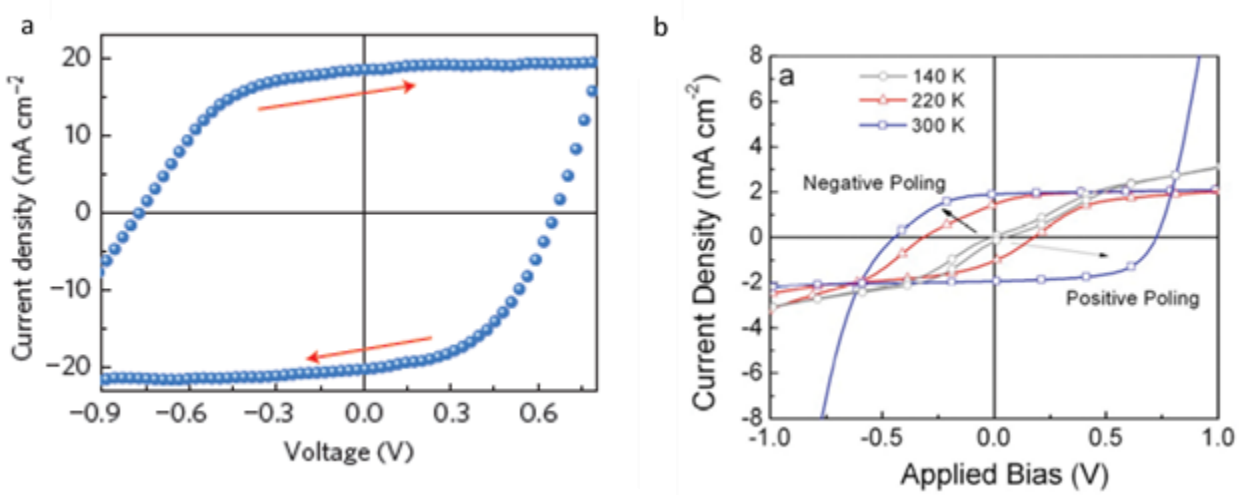

Fig 5.15: (a) Field induced poling behavior in non-selective contact PEDOT /perovskite/Au device when swept from +2.5V to -2.5V and from -2.5V to +2.5V [50] (b) Effect of temperature on Field induced poling on non-selective PEDOT/perovskite/Au device after poling at ± 1.5V for 60 sec [51].

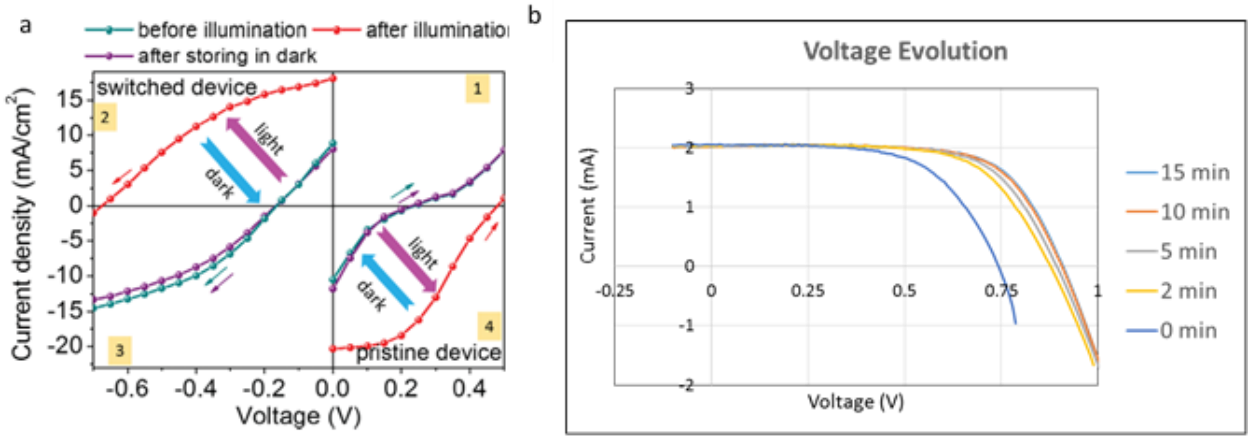

Fig 5.16: (a) IV measured on pristine and negative bias switched non-selective contact PEDOT/perovskite/Au device, before illumination, after illumination and storing in dark [52] (b) voltage evolution with open circuit exposure on TiO_2/perovskite/P3HT device as measured in our lab.

Leijtens et al. [51] also showed similar results on FTP/PEDOT/perovskite/Au devices. In this paper, it was shown that the effect of field induced poling goes down at lower temperatures. At room temperature the poling effect is significant, however at 140K, poling effect is very minimal.

Another interesting result is the self-poling of the perovskite solar cell. In our lab for a long time, we have observed, especially for n-i-p solar cell made on top of planar TiO_2 by sequential

vapor deposition, that V_{oc} and FF of the device increases drastically with light soaking under open circuit conditions. Unger et al. [32] have also reported that light soaking in high positive bias helps in removing the S shape and thus helps in achieving better fill factor. They also showed that if the device is light soaked under negative bias condition, the S shape behavior increases. Recent paper by Deng et al. [52] showed an increase in V_{oc} of the ITO/PEDOT/perovskite/Au device with exposure to light under open circuit.

5.4: Origin of hysteresis in bulk of perovskite: Ionic motion

Based on the hysteresis summary, when a bias is applied a temporary asymmetry is being developed in the device. The developed asymmetry is different for different biases. Such an asymmetry would explain hysteresis depending on the pre-bias conditions. Results of field-induced poling in symmetric contacts is a strong support for this phenomena. Now, when this asymmetry is in the time scale of sweep time; sweep direction, sweep rate and sweep starting value, it would be expected to create different amount of asymmetry and thus the hysteresis because of sweep direction, sweep rate and sweep starting value. Various mechanisms can be considered to be the origin for creating such an asymmetry.

Large interface states in perovskite-transport layer interface, which could act as charge trapping sites can be considered as one of the reasons of hysteresis. The charge trapping can increase or decrease the recombination and thus affect charge collection. Larger hysteresis in planar TiO_2 based devices and reduced hysteresis when TiO_2 was modified by PCBM supported this theory. However, results on reversible poling cannot be explained by the charge trapping. Also it has been observed that time scales for the trapping process are in the order of milliseconds, which is much faster than the time scale of IV hysteresis. Thus it was thought that hysteresis also depends

on more complex phenomena relating to the bulk of perovskite. Apart from charge trapping, hysteretic effects might also originate from the bulk of perovskite. For a perovskite hysteretic effect, initially there were two schools of thoughts 1) Ferroelectricity in perovskite and 2) Excess ions in perovskite.

Both these thoughts consider that perovskite can be polarized, which would create the asymmetry. One explanation is that polarization could be due to ferroelectricity. This ferroelectricity could arise from the classical off-centering of ions in bias ferroelectricity or from rotation of MAI within the unit cell. Because of the rotational freedom of the dipolar MAI molecule, it can align itself depending on the bias. This polarization could have an influence making the charge collection either more or less favorable at the contacts and thus result in hysteresis. There are some reports of observation of ferroelectric-like properties in perovskite solar cells [53],[54]. In piezoelectric force microscopy, polarized domains were observed and it was shown that depending on the scan direction and bias, phase contract magnitude was changed [54].

However recent reports by Beilsten-Edmunds et al. [55] suggest that although it is possible to observe ferroelectricity in piezoelectric force microscopy in addition to the polarization loops , the frequency dependence of poling at room temperature is uncharacteristic of ferroelectricity. Ferroelectric polarization should be frequency independent, whereas polarization observed in perovskites showed strong increase in magnitude with slower pulsing. The results reported in piezoelectric force microscopy might be due to piezoelectric behavior or electrochemical phenomena [56]. Meloni et al. [57] recently compared theoretically expected hysteresis from ferroelectricity to the experimental data, and their results suggested that it is unlikely that ferroelectricity is the origin of hysteresis. Leijtens et al. [51] showed that field-induced poling is prominent at room temperature and decreases significantly at lower temperature. This again goes

against the ferroelectric nature; as ferroelectric behavior is expected to enhance at lower temperatures where thermal disorder is lower.

Ionic motion can be thought of as the origin of asymmetry and hence hysteresis in these devices. Excess ions, as interstitial defects (iodide or methylammonium) may be present and predominantly labile throughout the film. Under operating conditions, the interstitial ions would be able to migrate to either side of the film, which could advantageously screen space charge buildup, aiding charge collection under working conditions. Some anomalies reported above do point to the ionic motion as possible reason for hysteresis. However, before explaining the anomalies we will first report origin of ionic motion.

It has been reported back in 1980s that lead halides, and also cesium lead halide perovskites are conductors of ions with very low activation energy [58]. Recently there are many reports which calculate activation energy for conduction of different ions in organic lead halide perovskites, mostly methylammonium lead iodide [36], [38], [41], [57]. Interstitial migration has not been observed in inorganic perovskites for the lack of interstitial spaces [41]. Similarly, even in the case of methyl ammonium lead iodide perovskite the vacancy mediated migration is thought to be dominant and is considered in all these reports. Activation energies calculated for $MAPbI_3$ are reported in the table 5.1. There are some discrepancies in all these reports, and the numbers do not exactly match. The difference in reported activation energies is probably because of different considerations of motion path and varied theoretical assumptions. However, broadly it was reported that I^- ions can migrate in a perovskite crystal through iodine vacancy ($V^{\bullet}_I$) mediation with a very low activation energy. Even though the numbers for $V^{/}_{MA}$ vacancies activation energy vary in these different calculations, activation energy for $V^{/}_{MA}$ reported in various reports can be achieved in the operation of perovskite solar cell. All reports suggest very high activation energy

for $V^{//}_{Pb}$ vacancies and it seems very difficult that $V^{//}_{Pb}$ moves in the operation/measurement condition of perovskite solar cells. Egger et al. [59] calculated the activation energy for H^+ ion migration (interstitial migration) to be 0.29 eV, which can also be a possible mechanism of ionic motion.

Table 5.1: Theoretically calculated activation energy for most preferred path for different vacancy motion in $MAPbI_3$ perovskite.

Lowest Activation Energy for ionic motion in $MAPbI_3$ perovskite (in eV)			
$V^{\bullet}_{I}$	$V^{/}_{MA}$	$V^{//}_{Pb}$	Report
0.58	0.84	2.31	Eames et al.[41]
0.08	0.46	0.80	Azpiroz et al.[36]
0.32	0.57	-	Haruyama et al.[38]
0.28	0.7	1.39	Meloni et al.[57]

Reaction	ΔH_S [eV per defect]	K_c	n [cm^{-3}]
$nil \rightarrow V^{/}_{MA} + V^{//}_{Pb} + 3V^{\bullet}_{I} + MAPbI_3$	0.14	0.41	2×10^{19}
$nil \rightarrow V^{/}_{MA} + V^{\bullet}_{I} + MAI$	0.08	3.82	2×10^{20}
$nil \rightarrow V^{//}_{Pb} + 2V^{\bullet}_{I} + PbI2$	0.22	0.02	8×10^{17}

Fig. 5.17: Calculated reaction energies, equilibrium constants and concentrations of Schottky defects in perovskite [60].

All these calculations consider ionic vacancies for the moving ions. Walsh et al. [60] theoretically calculated if there would be any vacancies at operating conditions. His calculations suggest that activation energy for formation of Schottky defects in perovskite is only 0.14 eV and at room temperature there would be as much as ~0.4% or ~10^{19} vacancies. It was suggested that these vacancies result in very shallow states. Buin et al. [61], Tahara et al. [62], Yin et al. [63] did suggest the presence of shallow defect states in perovskite. Formation of these ionic defects was suggested to be the reason for self-regulation and hence low carrier density of electrons and holes in the material.

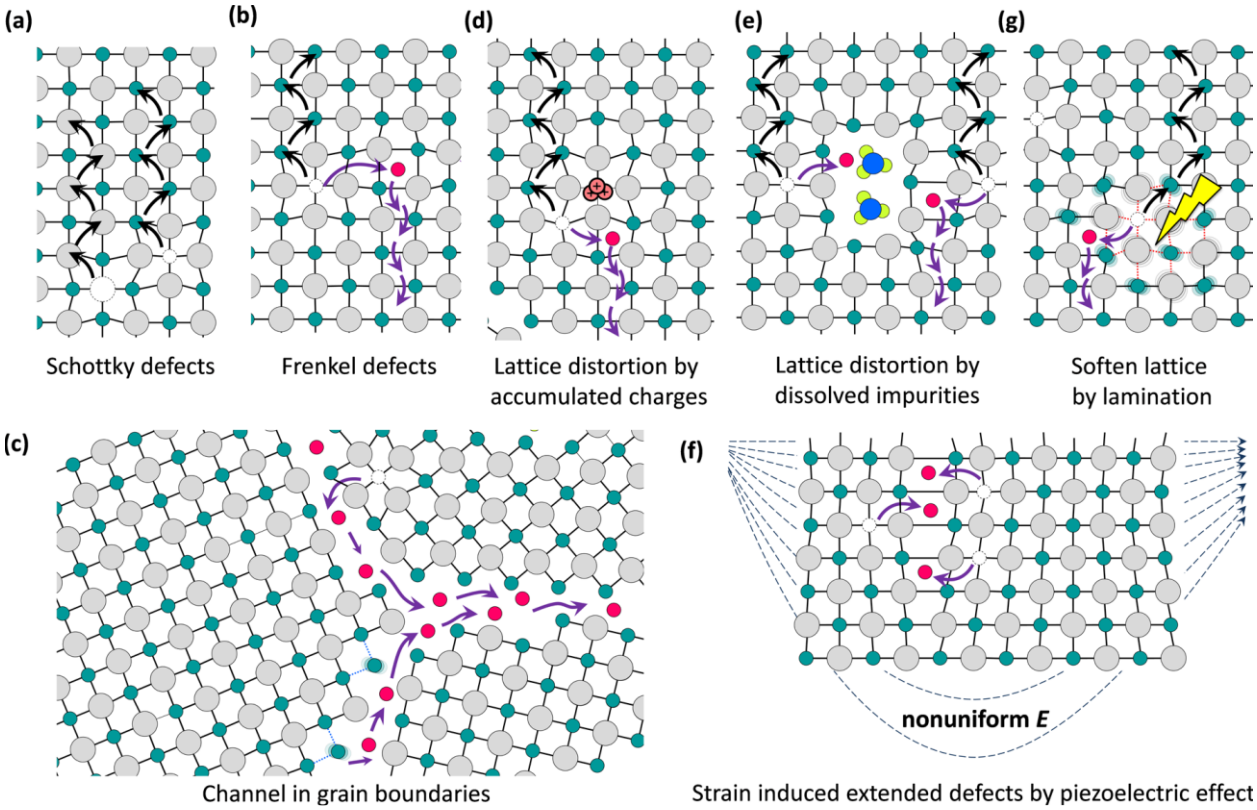

Fig 5.18: Illustration of different possible ionic motion pathways [64].

This discussion and most of the theoretical work done so far only considered motion of ions from shallow point or Schottky defects. However, there are multiple other pathways through which ions might move. Fig. 5.18 from Yuan et al. [64] explains all the possible pathways for ions. Xiao et al. [50] reported that in a field-induced poling, it was easier to switch the device with a smaller grain, which might indicate that grain boundary might be one of the channels for ionic motion. Yuan et al. [65] suggested that there might be two different rates for an ionic motion, which might mean that there are different types of ions that are moving or there are multiple possible pathways. Calculations done by Gottesman et al. [66] suggest that under light and bias, perovskite layer softens up and such a softness might also support ionic motion. If the softening is only because of light or because of voltage or both is an important question which needs to be answered.

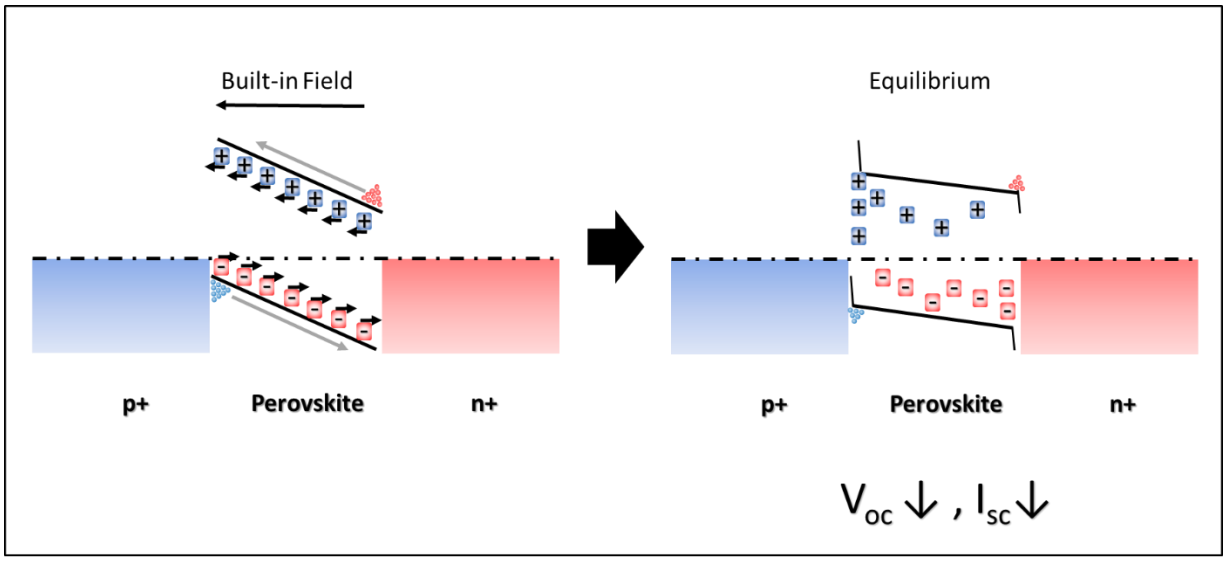

Fig 5.19: Proposed motion of ions and its effect on energy band diagram and device performance when perovskite device with free ions is connected in short.

All the observations noted above suggest that perovskite material might have ions which have low enough activation energies for migration. And thus, ionic motion might be possible in the perovskite active layer. Location and velocity of the ions would depend on the past and present applied bias. The location and velocity of ions might affect the effective built-in electric field, charge carrier density etc. inside the active layer. Such a change in built-in electric field and carrier density would cause the asymmetry which can explain most of the anomalies reported so far in the perovskite literature.

When the perovskite is sandwiched between p^+ and n^+ layer as shown in Fig. 5.19, the difference in workfunction of p^+ and n^+ would result in the built-in electric field inside perovskite active layer. This built-in field would force ions in the perovskite layer to migrate. Positive ions would move towards p^+ interface, whereas negative ions would move towards n^+ interface. Ionic motion would achieve equilibrium when the effect of built-in electric field matches the effect of field built by the diffusion of ions. Note that the exact amount of migration of ions at the steady state would depend on the number of free ions in the perovskite layer and the number of channels

for ionic motion. Even if there are no free ions to start with, the built-in field might be strong enough to break the bonds to create ions. In this case, the minimum field required to create ions would also add up in the equilibrium calculations. Note that, the positive and negative ions might have different mobilities and thus the displacement/velocity of oppositely charged ions might not be symmetric.

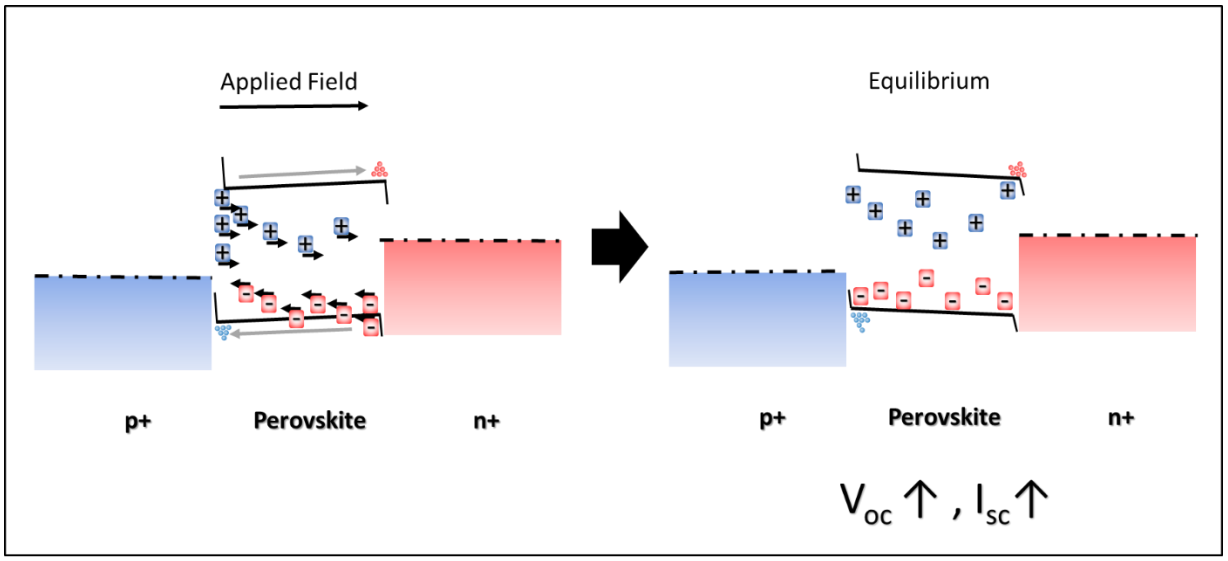

Fig. 5.20: Proposed motion of ions and its effect of energy band diagram and device performance when forward bias is applied to perovskite device with free ions which was initially kept at short circuit.

Now the application of positive bias, either in pre-biasing or during the sweep from high to low, would create an electric field in the perovskite active layer from p^+ to n^+ direction. Ions (and also electronic charges) would move away from interfaces. Ions moving back to their original location would in-turn increase the effective built-in field inside the perovskite active layer and thus V_{oc}. Migration of ions would depend on how long and how high the forward bias is applied, or the pre-biasing voltage, the sweep rate when sweeping, and the starting voltage for the sweep. Hence after 1) positive pre-biasing, and during 2) high to low sweep, 3) especially during slow sweep, devices give higher V_{oc}. Light induced poling, observed by Deng et al. [52] can also be

explained by this model. During exposure of a device in open circuit conditions, the device is essentially at high forward bias equal to instantaneous V_{oc}, which in-turn would increase the V_{oc}.

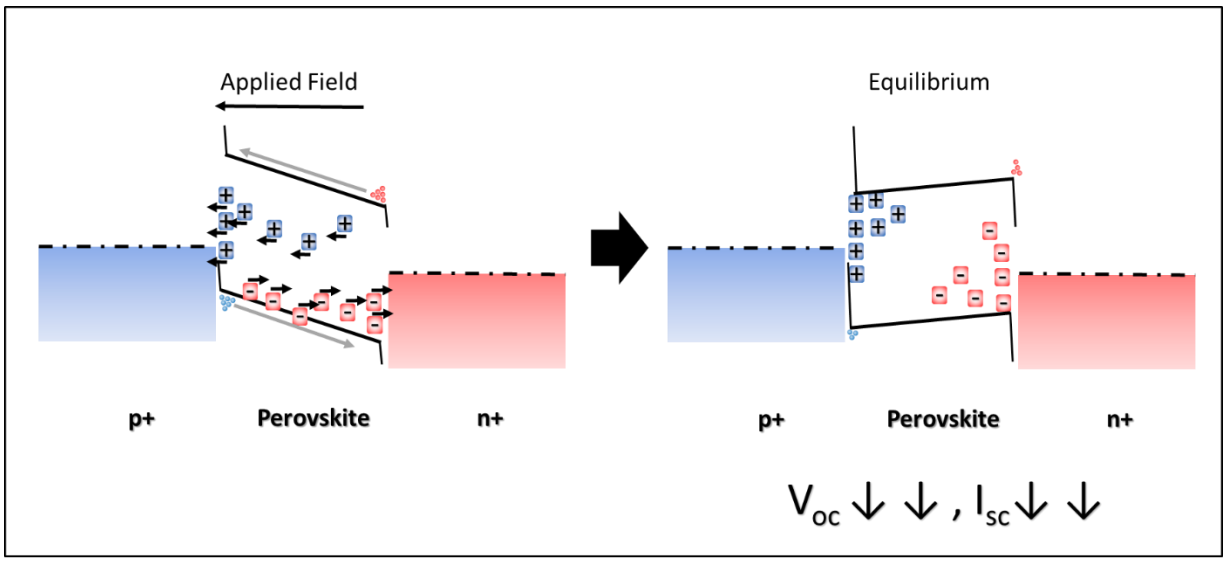

Fig 5.21: Proposed motion of ions and its effect of energy band diagram and device performance when reverse bias is applied to perovskite device with free ions which was initially kept at short circuit.

When a negative bias is applied, ions would move further towards the interface. This would bend energy levels even further. As shown in Fig. 5.21 such an increase in energy level would reduce the effective built-in field to a great extent. Reduction in the effective built-in field would reduce both V_{oc} and I_{sc}. Thus, when the device is pre-biased to a negative bias or device is swept from negative bias to positive bias, especially very slowly, IV measurements would show lower V_{oc} and I_{sc}.

Field induced poling, or switchable effect in non-selective contacts, observed by Xiao et al. [50] and Zhao et al. [34] can also be explained by this model. In non-selective contacts, there is no built-in electric field to start with and when device is poled positively (or negatively) ions would move to interfaces, effectively creating a built-in field in the direction opposite to the poling. This creation of built-in field would make it possible to measure V_{oc} and also collect charges giving

$I_{sc.}$ Ionic motion would be a thermally activated process and thus hysteresis observed in non-selective contacts would decrease with decrease in temperature as is reported by Leijtens et al. [51].

Hysteresis in the dark IV can also be explained in using this model. When IV is scanned from high to low, instantaneous velocity of the ions would be towards the interface (positive ions to p^+-i interface and negative ions to i-n^+ interface). This ionic motion, as explained before, would also be accompanied by opposite electronic motion, so that the electrons (holes) would also move towards p^+ (n^+), thus creating a negative current inside the perovskite active layer. Similarly, there will be a positive current inside active layer when dark IV is swept from low to high. Some of this current, which only accompanies the ionic motion, might leak out of the contacts giving a negative (positive) outside current when the dark IV is swept from high to low (low to high). For negative (positive) leakage current, the entire dark IV curve will shift down (up) in the current axis and thus voltage value where current changes direction will shift right (left) in voltage axis.

5.5: Results on NiO_x/perovskite/PCBM solar cell

With this theory / model of ionic migration in mind, we will move to explain results observed in this work. To start with, a typical device was thoroughly measured, and the IV, Dark IV, QE and CV of a typical device have been reported in Section 5.5.1. In Section 5.5.2 typical degradation and post degradation measurements have been reported. It was observed after photodegradation the device completely recovers. In Section 5.5.3 we show that recovery after exposure is thermally assisted and the device recovers very quickly when annealed to a higher temperature. In Section 5.5.4, the effect of device fabrication condition on degradation is analyzed. It can be seen that the device annealed to higher temperature or device solvent annealed results in

a higher grain size. In addition, the observed degradation is much lower in larger grain perovskite films. In Section 5.5.5, the effect of intensity on light degradation is analyzed. It can be seen at intense light, the device degrades much faster. Kindly note that in this section only observations will be reported, whereas the model to explain these observations will be built in Section 5.6

5.5.1: Typical device results

In this work, PIN perovskite solar cells were made by fast crystallization of Lewis base adduct perovskite solution with NiO_x and PCBM as transport layers. Details of the fabrication are reported in Chapter 3. Very briefly, NiO_x was deposited by e-beam evaporation on cleaned ITO slide. PbI_2:MAI:DMSO solution in DMF was used to deposit the perovskite. CB which acts as an anti-solvent for perovskite, extracts only DMF, and thus crystallizes the perovskite quickly when added on spinning perovskite solution. PCBM was deposited on the top of perovskite by spin-coating. Finally, back contact was evaporated using Al.

Such devices typically showed power conversion efficiencies ~11-13 %. These devices showed V_{oc} around 0.9 V, I_{sc} around 2 mA (device area = 0.106 cm^2), and FF around 67 %. Fig. 5.23 shows the IV measured under 1X on one of the best devices from high bias to low bias. Kindly note that, open circuit exposure might affect the IV measurements, and thus light illumination was closed using a shutter while making the contacts, and IV was measured immediately after opening the shutter. To avoid movement of ions during IV measurements, IV was measured very quickly at a sweep rate of around 100 mV/s. Fig. 5.22 also shows an IV measured from low bias to high bias. Very small hysteresis can be observed in these measurements.

Typical Dark IV of such a device is shown in Fig. 5.23. This dark IV fits n=2 and n=1 regions quite well with I_0 of in the order of ~10^{-13} A and ~10^{-18} A respectively. Note that, the dark

IV was measured after keeping device in dark for around 5 minutes to let carriers generated in the room-light relax. To avoid any hysteretic effects, dark IV was also measured very quickly.

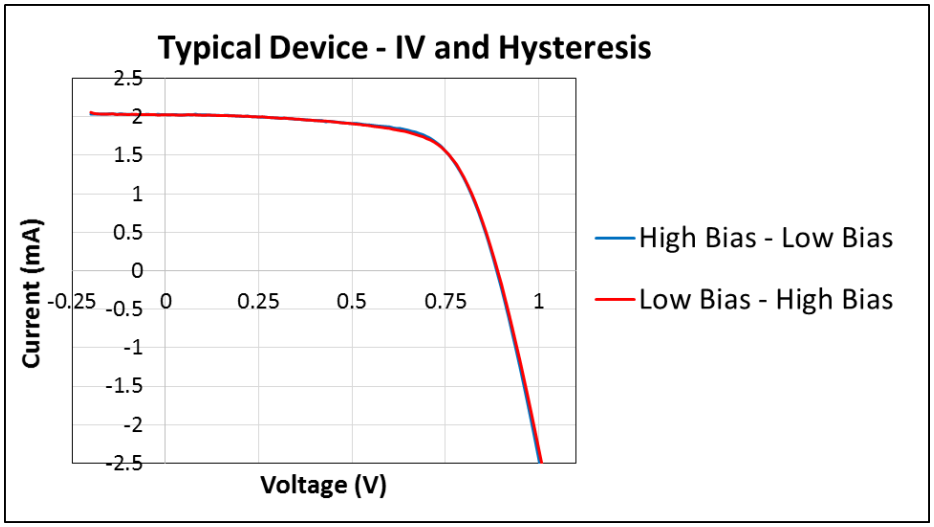

Fig. 5.22: IV measured for Typical ITO/NiO_x/perovskite/PCBM/Al device.

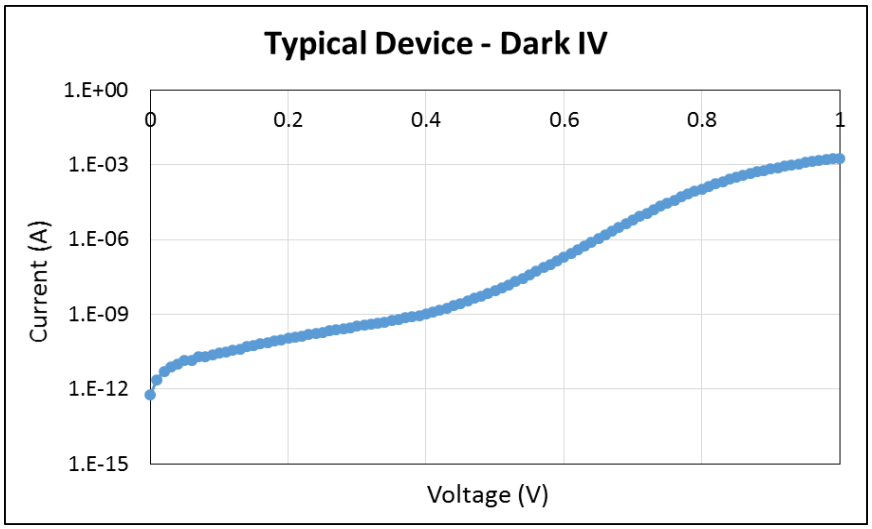

Fig. 5.23: Dark IV measured for Typical ITO/NiO_x/perovskite/PCBM/Al device.

Quantum Efficiency of a typical device is shown in Fig 5.24. It can be seen that the perovskite device absorbs till around 800 nm. The bandgap can be estimated from the $(QE*energy)^2$ vs energy plot, which comes around 1.6 eV.

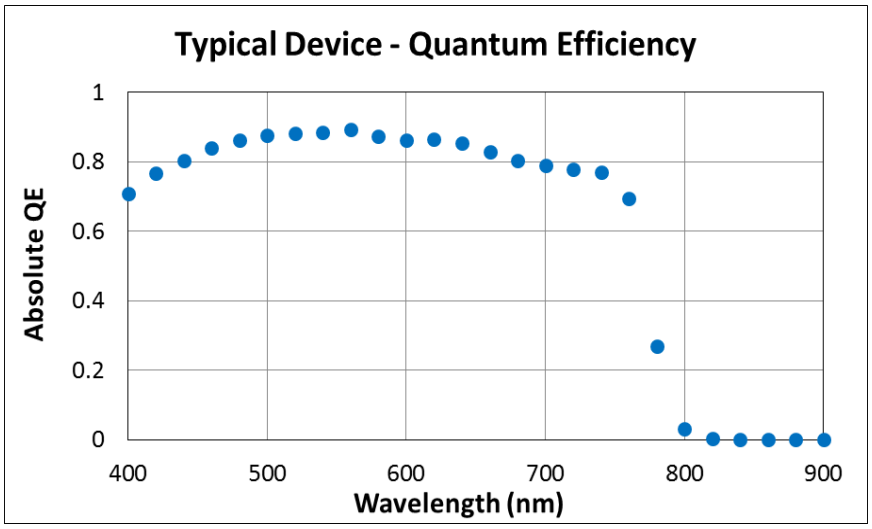

Fig. 5.24: Quantum efficiency measured on typical ITO/NiO_x/perovskite/PCBM/Al device.

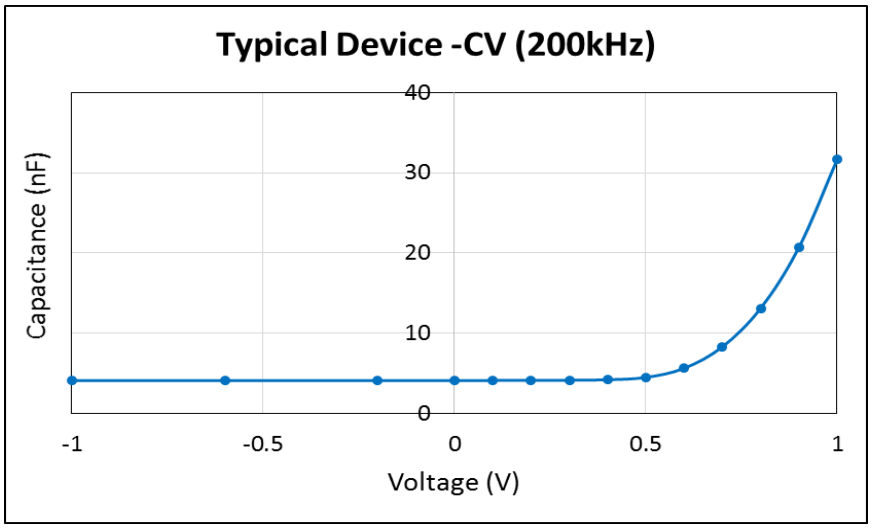

Fig. 5.25: C_pV measurement on typical ITO/NiO_x/perovskite/PCBM/Al device at 200 kHz.

Fig. 5.25 shows CV measurement on typical device. High frequency of 200 kHz was used for measurement here which would give us a better picture of depletion. This is because at high frequency very few traps would respond to the measurement. As per Appendix I, at high frequency, parallel equivalent model was used for capacitance calculation in LCR meter. From CV, it can be seen that the device is completely depleted, rather the depletion width is higher than the perovskite thickness. Kindly note that CV measurement also needs to be done very quickly in order to avoid

effect of hysteresis. This measurement was done manually using a video camera at a sweep rate of around 100mV/s.

5.5.2: Typical behavior during and after light exposure

Such a NiO_x/perovskite/PCBM device was exposed to 100 mW/cm^2 AM 1.5 solar spectrum simulated using ABET 10500 solar simulator (referred as 1X). In all experiments here devices were kept under open circuit conditions during light exposure as open circuit condition is closest to the maximum power point or the operational condition.

Fig. 5.26 shows the effect of 1X light exposure on IV parameters of the perovskite solar cell for 4 days. V_{oc} showed an initial increase and then saturated during the exposure. Whereas I_{sc} was found to decrease drastically initially and then slowly saturated during exposure. FF remained almost constant during the exposure.

CV was also measured on the device during exposure. Note that the standard measurement of CV is done under dark conditions to avoid the effect of any light generated current. However, it was found that closing the shutter to the measure CV (and dark IV) affected the degradation (this point will be presented in more detail in subsequent parts). To understand in=situ change in capacitance, CV was measured under light during exposure as shown in Fig. 5.27. From comparison of Fig 5.25 and 5.27 (before exposure black curve) it can be seen that under 1X exposure, the value of capacitance increased from the dark value and the concentration of charges responding to the CV measurement increased. It can be seen that with exposure, value of capacitance decreased initially quickly and gradually saturated.

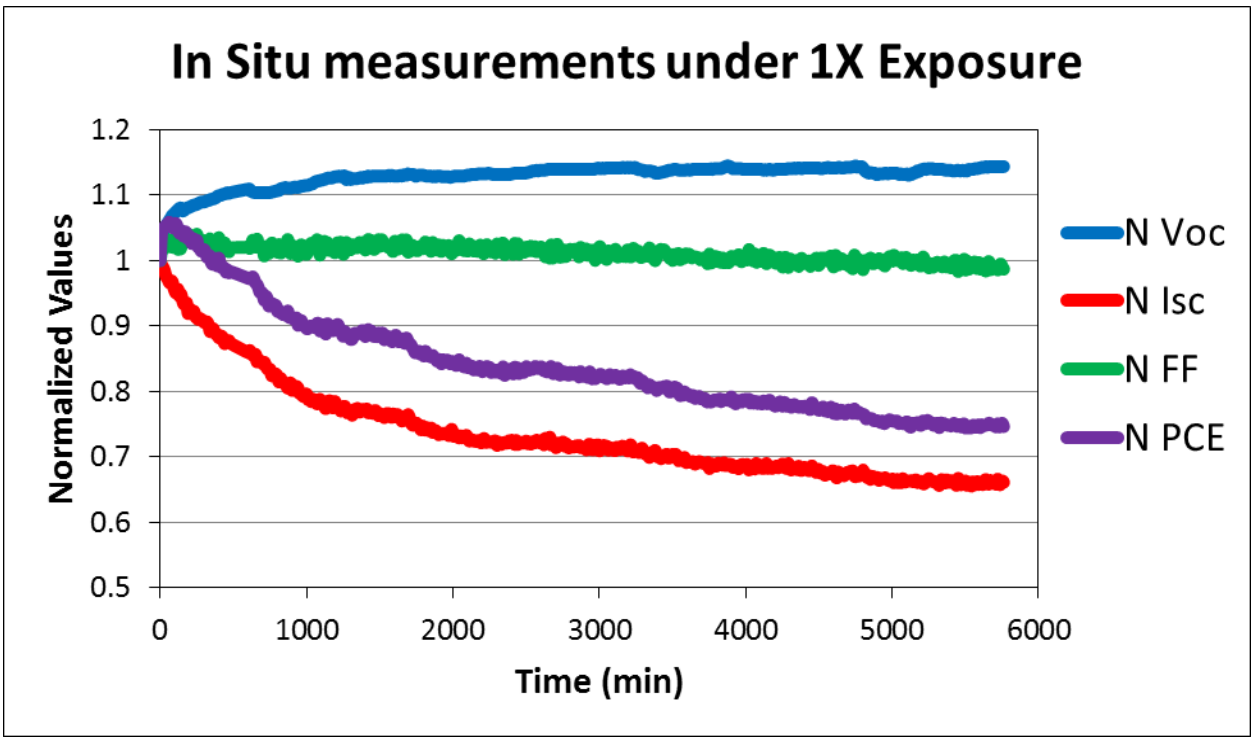

Fig. 5.26: Typical Effect of light exposure in open circuit condition on IV parameters of solar cell.

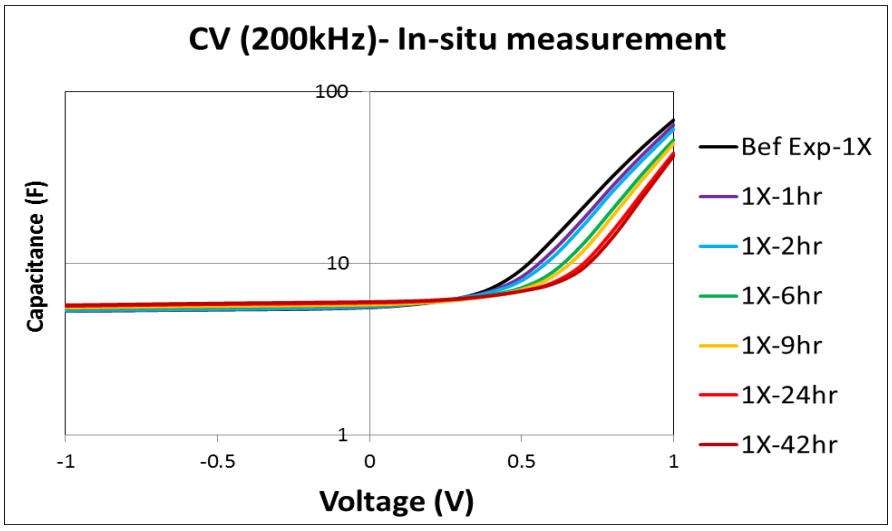

Fig. 5.27: In-situ CV measured in 1X illumination.

When the device was measured after stopping the exposure, very intriguing results were observed. Fig. 5.28 and Table 5.2 report the measured IV and IV parameters for time intervals after stopping the 1X exposure. It can be seen that the I_{sc} which decreased during the exposure is recovered very quickly and then remains constant. Whereas the V_{oc} which initially increased

during exposure decreases to a value even lower than the one before exposure, but then very slowly recovers to the value observed before exposure, showing a complete recovery.

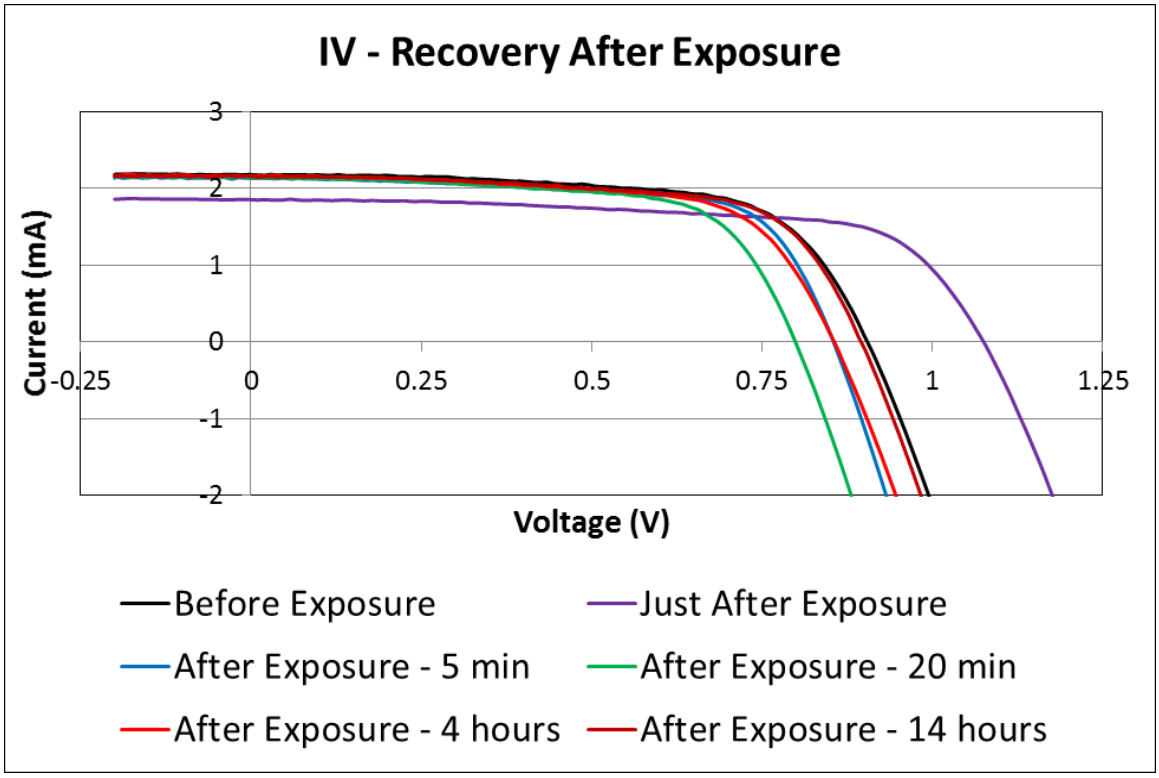

Fig. 5.28: IV measured before exposure, after exposure, during recovery and after recovery.

Table 5.2: IV parameters measured in degradation and recovery.

Degradation and Recovery in IV				
	V_{oc}(V)	I_{sc}(mA)	FF	PCE
Before Exposure	0.901	2.179	66.37	12.29
Just After Exposure	1.078	1.854	67.29	12.68
After Exposure - 5 min	0.856	2.131	68.83	11.84
After Exposure - 10 min	0.831	2.137	68.07	11.40
After Exposure - 20 min	0.800	2.136	66.42	10.71
After Exposure - 60 min	0.808	2.169	64.27	10.63
After Exposure - 2 hour	0.827	2.144	65.22	10.90
After Exposure - 4 hour	0.858	2.165	65.36	11.45
After Exposure - 14 hour	0.891	2.156	67.16	12.17

Hysteresis was also measured at all these time scales. Table 5.3 reports the IV parameters measured in different sweep directions during exposure and recovery. For all these time scales I_{sc} and FF values are pretty close, whereas the different amounts of hysteresis can be observed in V_{oc} values. This hysteresis is very small before exposure and also just after the exposure. However, it increases significantly in few minutes after exposure and then slowly recovers as V_{oc} is also recovered.

Table 5.3.: Hysteresis in IV measured during exposure and recovery.

Hysteresis in IV Measurements During Exposure and Recovery					
	Sweep Direction	V_{oc}(V)	I_{sc}(mA)	FF	PCE
Before Exposure	High to Low	0.901	2.179	66.37	12.29
	Low to High	0.910	2.170	66.68	12.42
Just After Exposure	High to Low	1.078	1.854	67.29	12.68
	Low to High	1.054	1.845	69.12	12.68
After Exposure - 20min	High to Low	0.800	2.136	66.42	10.71
	Low to High	0.853	2.097	66.96	11.30
During Recovery	High to Low	0.827	2.144	65.22	10.90
	Low to High	0.843	2.118	66.05	11.13
After Recovery	High to Low	0.891	2.156	67.16	12.17
	Low to High	0.899	2.136	68.55	12.42

Note that, CV, Density of States (DOS), dark IV could not be measured immediately after the exposure as closing the shutter and putting dark box on the device took some time. At every time scale, precisely the same order was followed in doing the measurements. First CVs were measured, then DOS, then Dark IV and then IV. This entire order took around 25-30 minutes. However same time was ascribed to different measurements. That is all the measurements done after closing the shutter in 25 minutes will be named *After Exposure* measurements. Note that, in IV, *Just After Exposure* and *After Exposure* titled measurements were actually 25 minutes apart. Also these 25 minutes were not considered in the times reported. Thus if 2 measurements were done before '*After Exposure*-After 60 min' titled measurement, it was done actually 60+50 minutes after closing the shutter. This naming convention will be used here on.

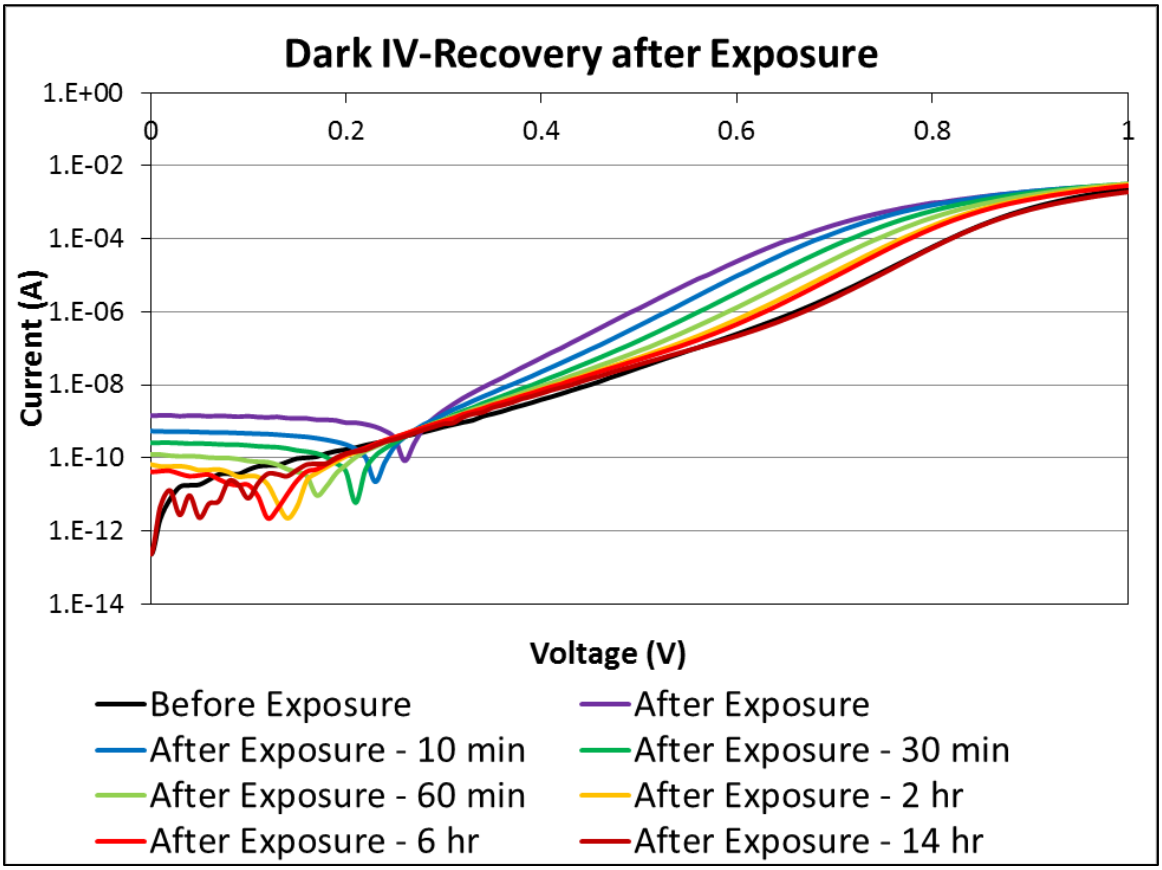

Fig. 5.29: Dark IV measured during exposure and recovery.

Fig. 5.29 shows dark IV measurements. After exposure, I_0 value increased drastically, which made the dark IV go to series resistance-limited region much early. Another very interesting change was observed in the dark IV. Dark IV is always plotted in log scale by taking the absolute value of current. Thus, in such a plot, voltage at which the current changes from negative to positive is usually shown by a dip. Dark IV measured before exposure had that dip at around zero bias suggesting that dark IV is negative in negative voltages and positive in positive voltages. However, the dark IV measured after exposure showed a dip at higher positive voltage values. This suggests that there is some negative current flowing in the device even in dark at zero bias. As device recovered this negative current also decreased indicating the complete device recovery.

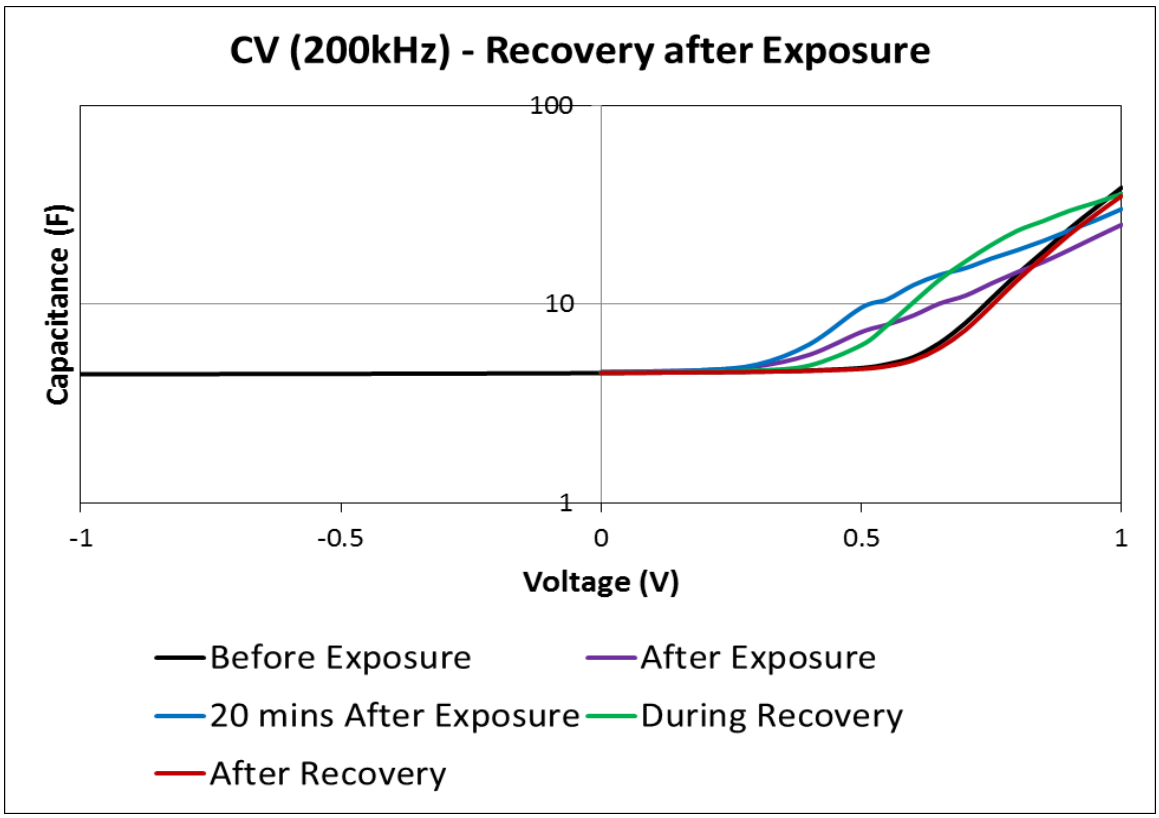

Fig. 5.30: CV measured during exposure and recovery.

Fig. 5.30 and Fig. 5.31 shows CV measured manually in exposure and recovery in semi-log scale. In CV measurement shown in Fig. 5.31, capacitance value was written down after changing bias manually and thus took significantly longer time. It can be seen that before exposure and after recovery, an increase in capacitance at higher voltage shows a uniform slope. However, in CV measurements during the recovery, rate increase in capacitance strongly decreased at high voltages thus showing a strange behavior. It can be seen that in Fig 5.31 the rate of capacitance increase is uniform even during the recovery measurements. In this case, CV was actually measured very quickly using a video camera, where voltage values were changed quickly and capacitance values were written down from the video recording. Disappearance of change in CV slope when measured very quickly suggests hysteretic behavior.

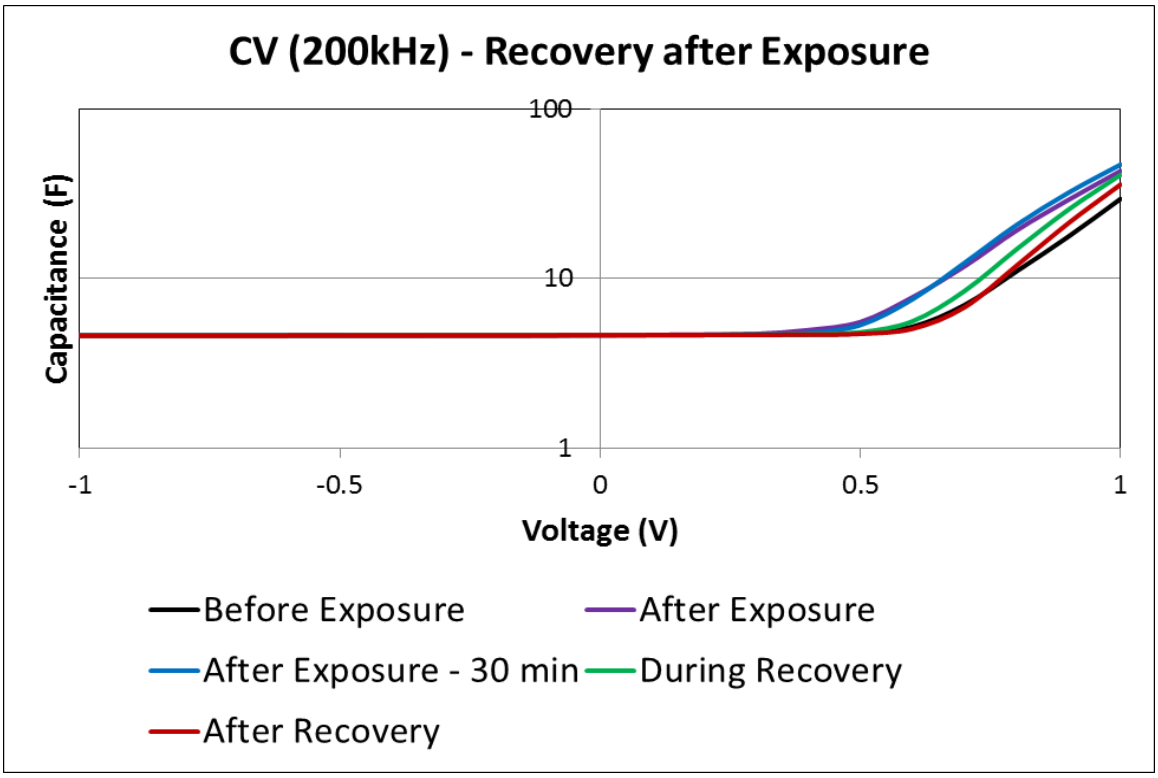

Fig. 5.31: CV measured during exposure and recovery, very quickly.

These CV measurements suggest that after exposure the capacitance value increases. Again kindly note that, this after exposure measurement corresponds to IV measured 30 minutes after closing the shutter and thus voltage of the device has decreased below the *Before Exposure* value. Thus after exposure, when V_{oc} decreases, C increases; which matches the decrease in C, when V_{oc} is increased during the exposure. As the device recovered, or as the V_{oc} increased, C value decreased as is evident from these figures. CV measurement matches the measured IV, even in terms of hysteresis seen in the non-uniformity of the CV slope. *Before Exposure* and *After Complete Recovery* device shows very little hysteresis in both IV and CV, whereas hysteresis is significant during recovery after exposure.

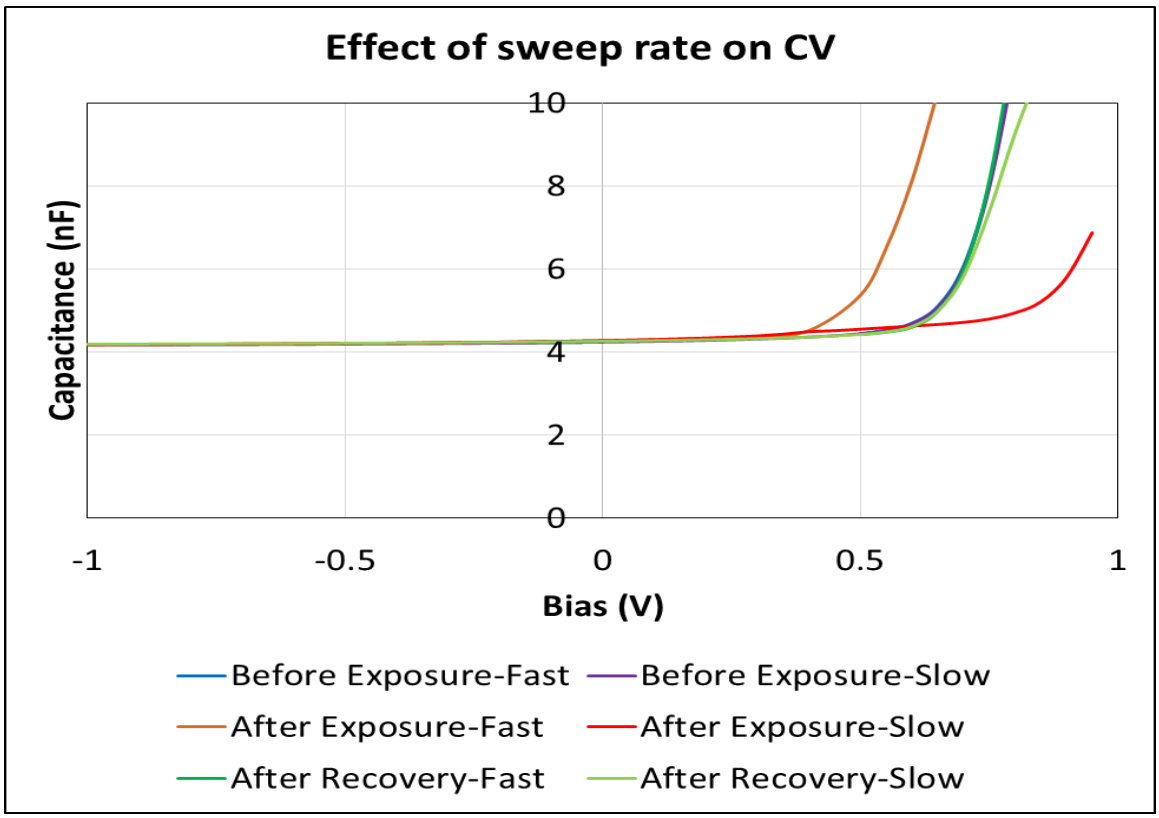

Fig. 5.32: Effect of Sweep rate of CV measurement before exposure, after exposure and after recovery.

Decrease in the slope of CV at high voltage values when CV is measured slowly suggested that at voltage values capacitance value is decreasing. CV was measured very slowly, by letting capacitance saturate (saturation defined as change in C less than 1pF/sec). At high voltage capacitance took 20-40 minutes to saturate. The resulting CV measurements are shown in Fig. 5.32. This plot is plotted in normal scale for the sake of ease of understanding. It can be clearly seen that before exposure and after recovery, fast and slow CV values do not show any hysteresis. After exposure CV values show a huge sweep rate hysteresis in capacitance, capacitance value is higher than that of the one before exposure when measured quickly, whereas when measured slowly, capacitance value is even lower than the one before exposure.

The density of states inside the bandgap was also calculated by measuring the capacitance at different frequencies (CF). Fig. 5.33 shows DOS measured on perovskite solar cell during

exposure and recovery. DOS is slightly shifting to deeper energy, however, as the number of states remain same, change in DOS can be assumed to be negligible.

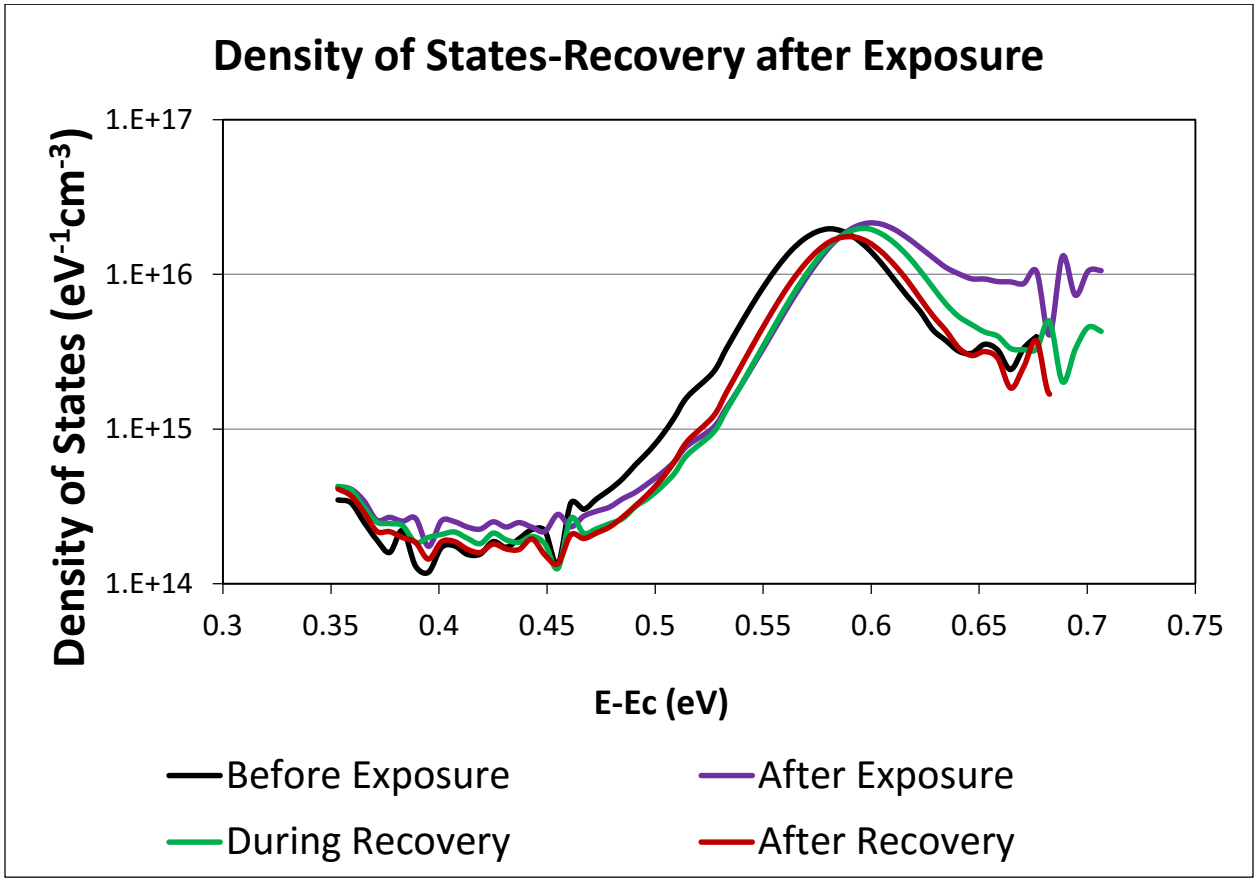

Fig. 5.33: DOS measured during exposure and recovery.

5.5.3: Effect of temperature on recovery

In Section 5.5.2, it was shown that perovskite solar cell degradation can be completely recovered. Complete recovery at room temperature (RT) in 15 hours prompted us to check if the recovery can be enhanced at higher temperatures. For this, three dots were exposed at 1X for 96 hours.

Fig. 5.34 shows changes in V_{oc}, I_{sc}, FF and PCE for these three dots. It can be seen that degradation in these three dots is very similar and thus they can be compared for recovery at different temperatures. Table 5.4 report IV parameters before exposure, just after exposure and

during recovery. As V_{oc} recovery determines recovery time, Fig. 5.35 shows the plot of V_{oc} vs time during recovery. In this plot, to get a complete picture, before exposure and just after exposure, V_{oc} values are also plotted at -400 min and -50 min for simplicity. In all three dots device degraded equally during exposure. I_{sc} completely recovered immediately in all three dots. However, V_{oc} which took 15 hours to recover at RT (measured to be around 25^0C) was recovered completely in just 30 minutes at 50^0C and 10 minutes at 75^0C.

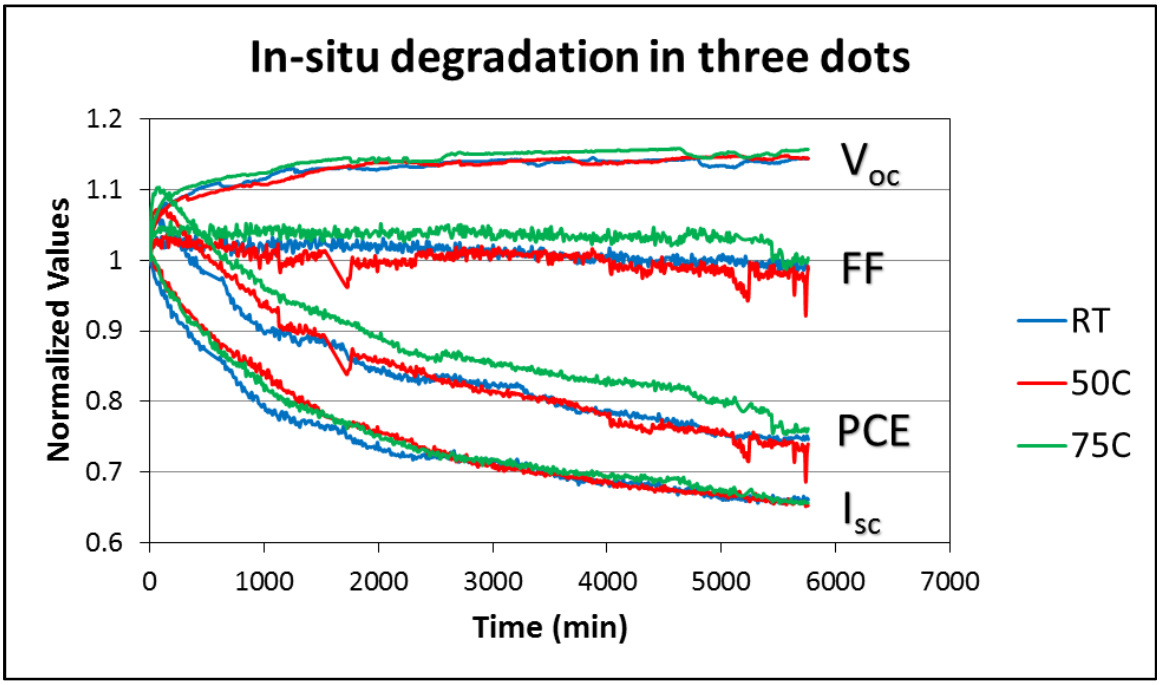

Fig. 5.34: In-situ IV parameters in three dots exposed 1X for 96 hours in open circuit condition.

These results of faster recovery at higher temperature suggest that device recovery is thermally assisted. There must be some thermal mechanism which is responsible for device recovery.

In these three dots, dark IV and CV showed similar change during degradation as reported in Section 5.5.2. Dark IV and CV also recovered completely with V_{oc} recovery. DOS did not show any significant change with exposure or with recovery at different temperatures.

This experiment was repeated thrice and same results were obtained.

Table 5.4: IV parameters for device recovery measured at different temperatures

Accelerated Recovery at higher temperatures									
	RT Recovery			50C Recovery			75C Recovery		
	V_{oc}	I_{sc}	FF	V_{oc}	I_{sc}	FF	V_{oc}	I_{sc}	FF
Before Exposure	0.91	2.11	66.36	0.90	2.18	65.98	0.90	2.25	63.97
Just After Exposure	1.04	1.41	66.27	1.03	1.42	65.54	1.04	1.45	64.89
After Exposure	0.80	2.01	65.20	0.82	2.06	65.31	0.80	2.06	63.63
After 10 min Recovery	0.81	2.09	64.34	0.87	2.11	64.79	0.91	2.12	64.35
After 30 min Recovery	0.84	2.10	65.31	0.90	2.09	63.95			
After 1 hr Recovery	0.86	2.09	66.73						
After 2 hr Recovery	0.88	2.10	66.22						
After 6 hr Recovery	0.90	2.07	65.66						
After 14 hr Recovery	0.91	2.08	66.91						

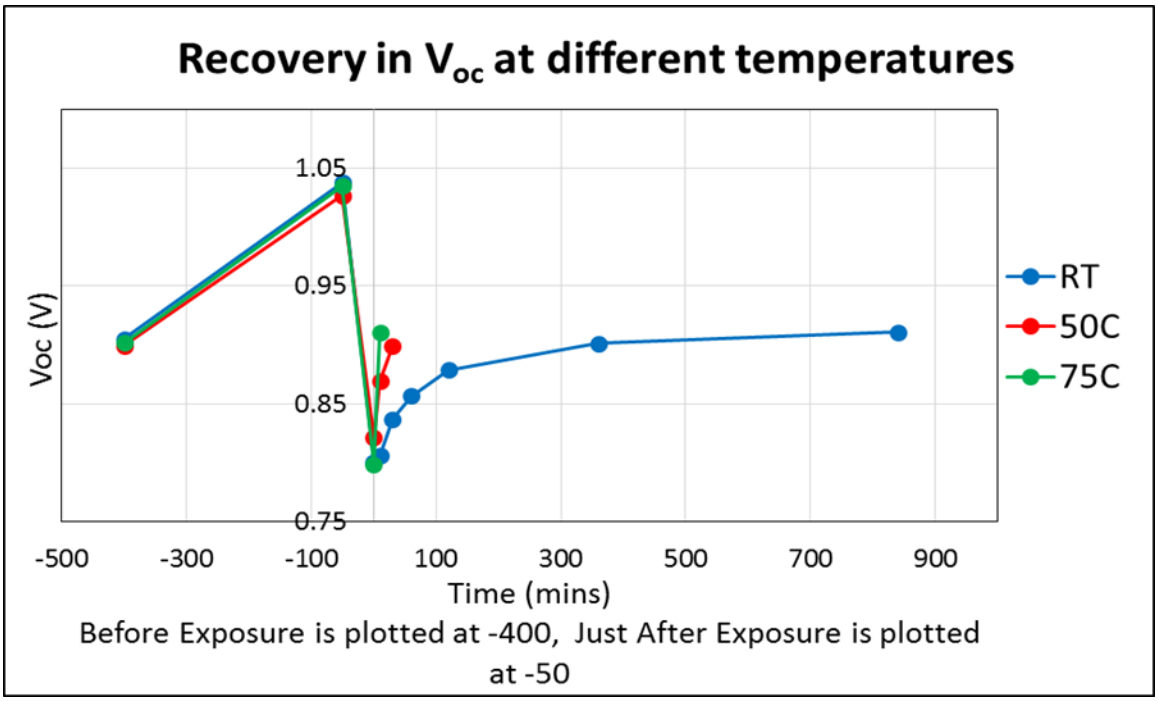

Fig 5.35: Change in V_{oc} during recovery at different temperatures after exposure.

5.5.4: Effect of light intensity on degradation

Degradation kinetics were checked for effect of light intensity. Three dots from a same device, all of which showed very similar behavior before exposure IV, were exposed at 0.25X, 1X

and 4X in the open circuit conditions. Difference in V_{oc} for 4 times increase in intensity was about 50mV.

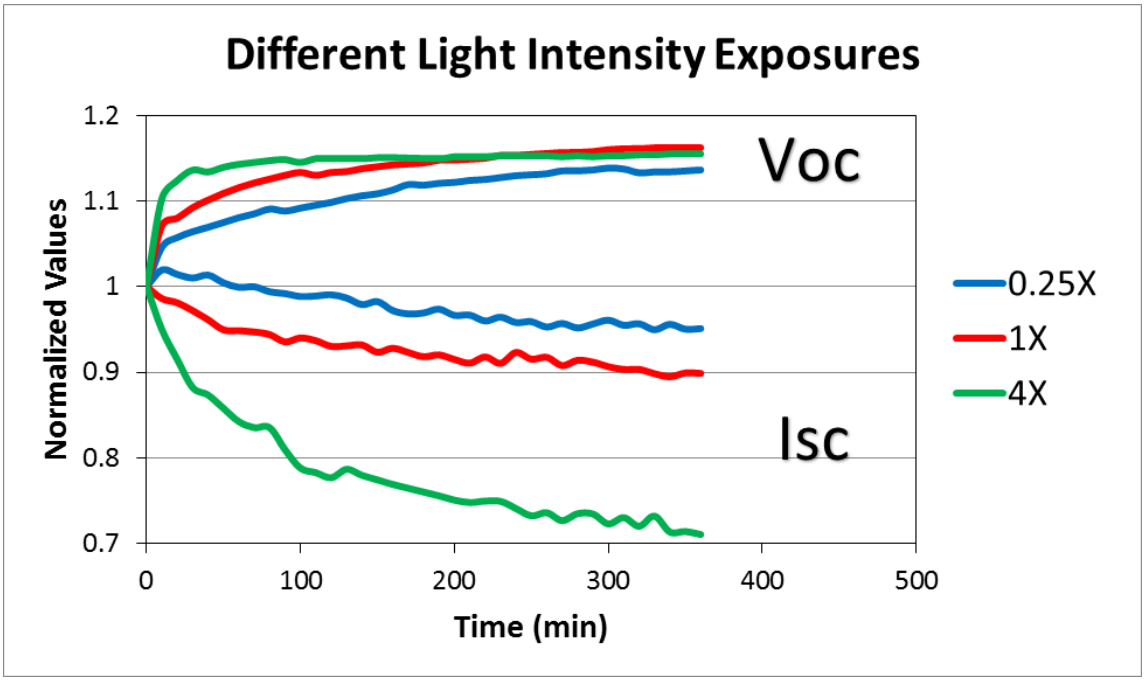

Fig. 5.36: Degradation at different intensities of light.

Table 5.5: IV parameters for degradation at different light intensities.

Degradation at different light intensities								
					Change (%)			
	Voc (V)	Isc (mA)	FF	PCE	Voc (V)	Isc (mA)	FF	PCE
Before 0.25X Exposure	0.91	1.97	64.31	10.84				
Just After 0.25X Exposure	1.03	1.86	68.97	12.43	14	-6	7	15
After 0.25X Exposure	0.83	2.02	64.88	10.28	-8	3	1	-5
Before 1X Exposure	0.89	1.93	65.10	10.56				
Just After 1X Exposure	1.05	1.73	69.49	11.90	17	-10	7	12
After 1X Exposure	0.78	1.98	62.78	9.12	-13	3	-4	-13
Before 4X Exposure	0.89	1.93	65.34	10.56				
Just After 4X Exposure	1.04	1.41	68.94	9.52	17	-26	6	-10
After 4X Exposure	0.73	1.83	58.95	7.42	-17	-5	-10	-29

In-situ V_{oc} and I_{sc} are plotted in the Fig. 5.36. It can be seen that due to intense light, the current degraded much more. The increase in V_{oc} due to different light intensities after 6 hours was almost the same, but that is because of the early saturation of V_{oc} increase. If V_{oc} increase is

closely observed for the start of the exposure, it can be seen that the intense light increased V_{oc} much faster. Table 5.5 gives IV parameters before exposure, just after exposure and also after exposure. Overall change in device efficiency also showed the same trend, that is, in the intense light PCE degraded the most. Another important result can be observed from the table, that the decrease in V_{oc} after exposure also followed the trend. 4X exposed device showed more decrease in V_{oc} than 1X, which showed higher decrease than 0.25X. Hysteresis also showed a similar trend.

5.5.5: Effect of perovskite film quality on degradation

The effect of perovskite film quality on degradation kinetics was also checked. Standard fabrication conditions give perovskite film with a grain size of about 200 nm. During the device optimization work, it was observed that if after formation, perovskite film is annealed at 100^0C in the presence of small quantities (2µL) of DMSO solution for 15 minutes, grain size of the film drastically improves from 200 nm to almost 1 µm as is shown in Fig. 5.37.

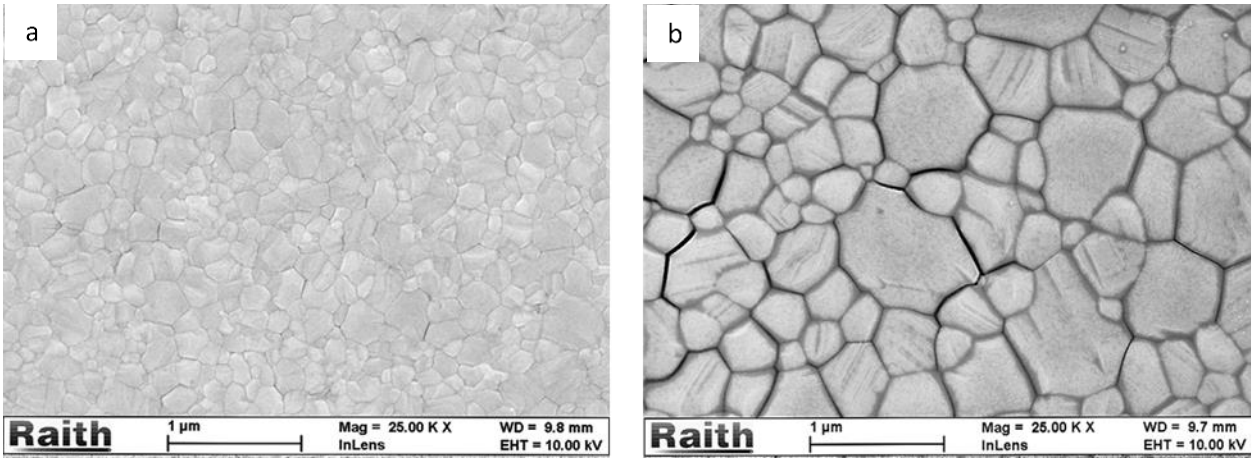

Fig. 5.37: Effect of solvent annealing on perovskite grain size (a) pristine film (b) film solvent annealed in 2µL DMSO at 100^0C for 15 mins.

Unfortunately for device optimization, increase in grain size did not improve the device performance (Fig. 5.38). But that is better for comparison of stability studies. Now we have a

device with similar V_{oc} and I_{sc} but different grain sizes and thus the effect of grain size on stability can be pointed out.

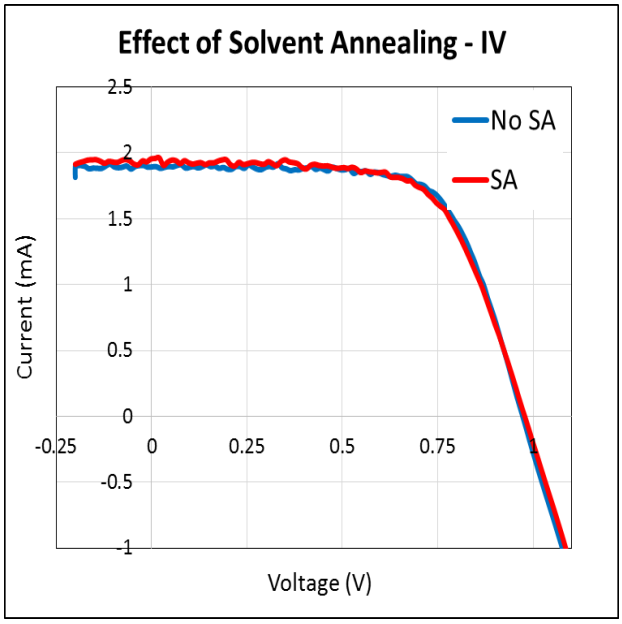

Fig. 5.38: Device performance for solvent pristine (No SA) and annealed film (SA).

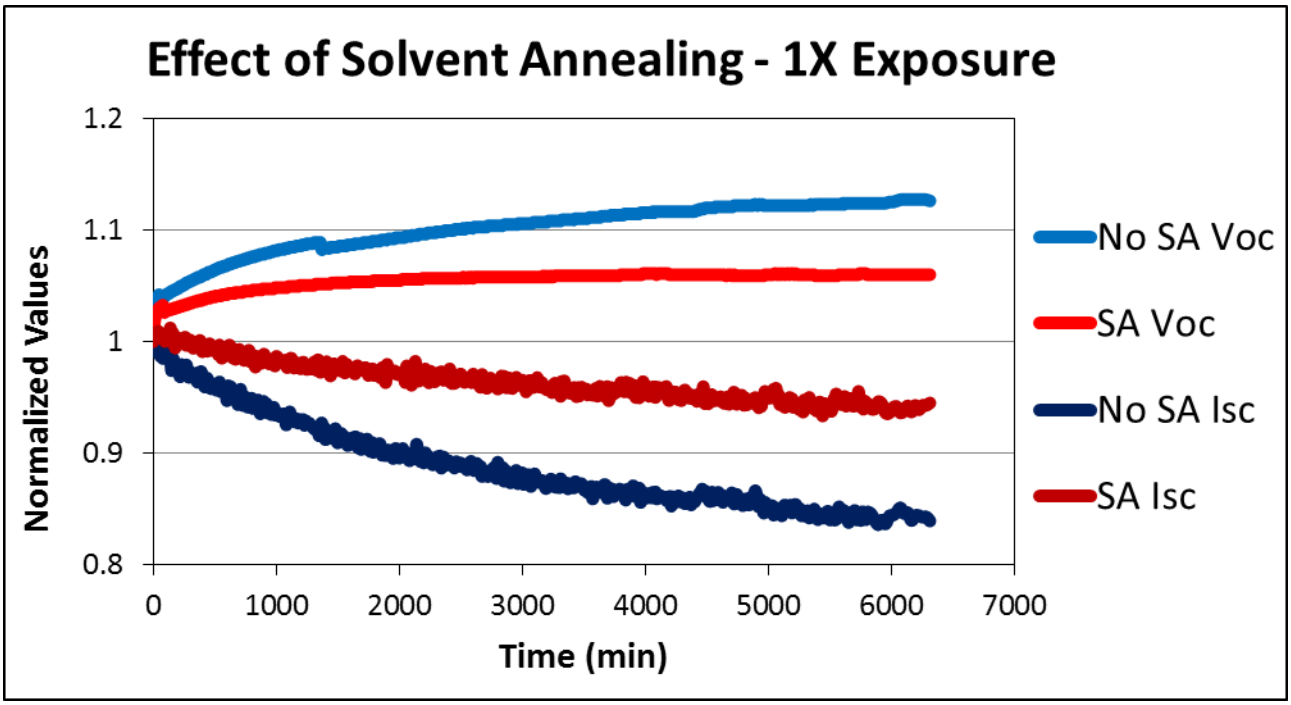

Fig 5.39: In-situ measurements for device with pristine film (No SA) and film with solvent annealing (SA).

Fig. 5.39 suggests that solvent annealing has a significant effect on device degradation kinetics. A device with solvent annealed film degraded significantly slower than the device without solvent annealed film. Three batches of devices showed similar trend in the rate of degradation.

Similar pattern in grain size and degradation was observed when perovskite film annealing condition was changed. Annealing the perovskite to a higher temperature of 140^0C instead of 100^0C for a short time yielded devices with higher grain size and significantly slower degradation

These results suggest that the grain boundaries assist degradation or degradation pathway is through grain boundaries.

5.5.6: Effect of bias applied on degradation

Exposures were done at same light intensity but at different bias levels, to check the effect of bias and also current on the degradation kinetics. As it can be seen from Fig. 5.40 and Fig. 5.41, very interesting results are observed when device is exposed in 1X at different bias values.

I_{sc} of the device decreased much faster when device is kept at constant bias of 1.1 V, than when device is kept at open circuit. Kindly note that, V_{oc} of the device was 0.9 V to start with and then it increased to 1.05 V during degradation. Decrease in current, when is exposed at 0.9 V is lower than that at open circuit condition. Devices degraded at bias values lower than 0.9 V showed no significant decrease in I_{sc}. Devices were even exposed at short circuit and at -1.1 V, which also showed no significant change in I_{sc}. Kindly note that, at 1.1 V, 1X, device has positive current, at open circuit voltage, device has 0 current, whereas at 0.9 V and lower device has negative current, such that all photogenerated careers are collected somewhere around 0.7 V and lower.

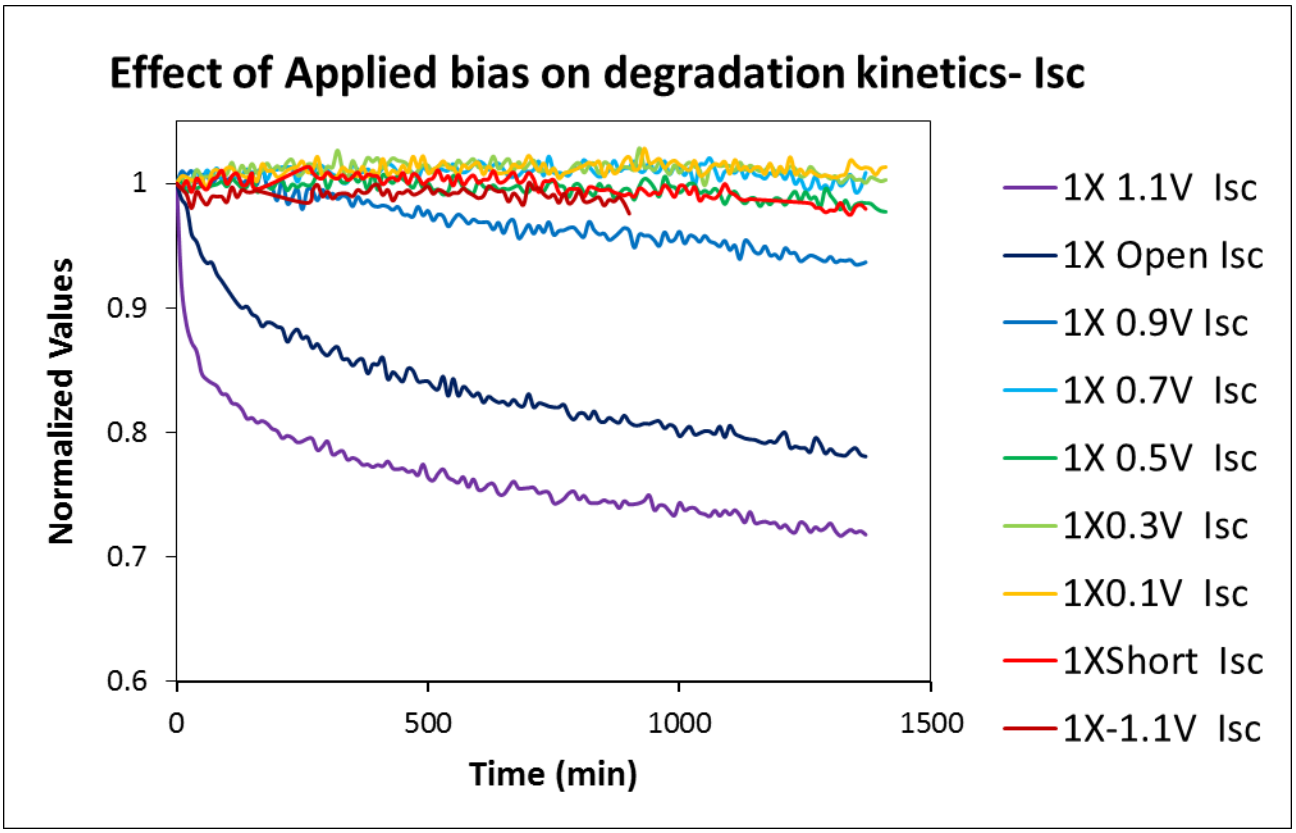

Fig. 5.40: In-situ I_{sc} values for devices exposed to different bias values at 1X light intensity.

5.6: Model

In Section 5.5, the effect of light exposure in open circuit conditions and post exposure recovery on NiO_x-based PIN perovskite solar cell was reported in different conditions. Perovskite solar cells showed seemingly anomalous effect of light exposure. During light exposure V_{oc} of the device improved, whereas I_{sc} decreased. This change in V_{oc} and I_{sc} was found to be reversible. In Section 5.4 it was suggested that ionic motion inside the perovskite bulk can be used to explain the observations of hysteresis and other anomalous behaviors observed in perovskite solar cell. In this section, a model has been suggested based on ionic motion inside the perovskite bulk, to explain the seemingly anomalous observations of light-induced changes in perovskite solar cell.

5.6.1: Summary of Observations

Before moving on to report the model, in this subsection, firstly all observations regarding the effect of photoexposure are summarized. Fig. 5.39 summarizes all results for a typical device.

Photo-degradation measurements on Perovskite Solar Cells

	V_{oc}	I_{sc}	C	Hysteresis	I_0	Dark IV switch V
During Exposure	↑	↓	↓	~		
After Exposure	↓↓	↑	↑↑	↑	↑	↑
During Recovery	↑	~	↓	↓	↓	↓

Fig. 5.41: Summary of effect of photoexposure on perovskite solar cell.

In a standard NiO_x/perovskite/PCBM device; during exposure, V_{oc} of the device increases and then saturates. Whereas, I_{sc} of the device decreases and then slowly saturates. Capacitance measured under light shows a decrease in value with light exposure.

After stopping light illumination, decreased I_{sc} of the device recovers quickly to the initial value. Increased V_{oc} on the other hand, decreases to a value lower than the initial value. During this decrease of V_{oc}, decreased capacitance also shows an increase to a value higher than initial value.

Decrease in V_{oc} / increase in capacitance stops after some time and then slowly starts to recover. After exposure, hysteresis in the V_{oc} and from the measurement of CV for the device has increased. Reverse saturation current has also gone up. Another intriguing observation was that the device in dark has a negative current at zero bias. As V_{oc} and capacitance of the device recover, hysteresis, I_0 and negative current at zero bias in the dark also recover slowly but completely.

The recovery was observed to be temperature dependent. At higher temperatures the device recovered much quickly.

The rate of increase of V_{oc}, the decrease of I_{sc} during exposure and also decrease in V_{oc} after exposure was found to be intensity dependent. At higher intensity, the device degraded much faster.

The rate of increase of V_{oc}, decrease of I_{sc} or simply degradation rate was found to be dependent on the perovskite film quality. Film with larger grain size showed slower degradation.

5.6.2 Model to explain photodegradation in perovskite solar cells

We propose a model to explain observation in the photodegradation of perovskite solar cell reported above.

Ionic motion inside perovskite bulk has been widely considered as the reason for the anomalous hysteresis in IV measurements in perovskite solar cells. This model is also based on the ionic motion. Perovskite has ions which can move in the bulk of the perovskite. It is assumed that electron and hole transport layers will block these ions and will not have any reactivity to these ions. However, ions can be neutralized by recombining with electron (or hole) at the interface of the transport layer.

5.6.2.1: Before exposure

We assume that ions are present and mobile in the perovskite film at room temperature. When device is fabricated, equalization of fermi level will create built-in field inside perovskite layer. Ions will move in this built-in field such that positive ions (MA^+) will move towards p^+ interface and negative ions (I^-) towards n^+ interface (Fig.5.40). This movement of ions will create an ionic field in the direction opposite to the built-in field. This will result in reduction in effective

built-in field. Reduction in effective built-in field would naturally reduce V_{oc} of the device. Reduction in effective built-in field will also decrease depletion width and thus will increase capacitance of the device.

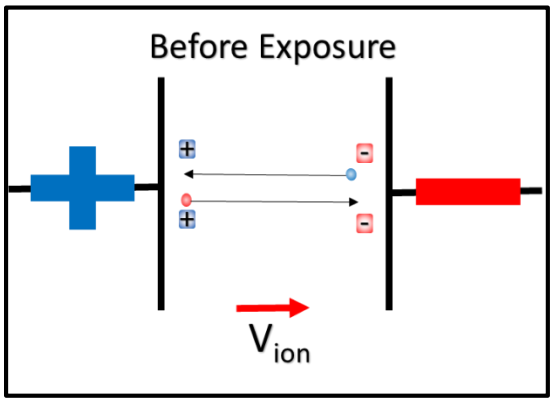

Fig.5.42: Proposed location of ions and thus generated Ionic field in the as fabricated device.

5.6.2.2: During exposure

Now when device is exposed under open circuit voltage, we are in a way applying positive bias equal to V_{oc} on the device. This will reduce V_{bi} almost to zero when ions would tend to move bulk of the perovskite in the V_{ion} field (Fig. 5.41). This movement of ions will reduce V_{ion} almost to zero and thus V_{bi} of the device (in short circuit) would increase back. This increase in V_{bi} would result in increase in V_{oc} and also decrease in capacitance. The process of ion movement to the bulk will continue until all ions are moved to center and will then saturate. Thus V_{oc} increases and then saturates.

We propose that the light under open circuit condition, will generate more ions in the bulk of the perovskite in the bulk of the perovskite. As ions are generated in the bulk uniformly it would not affect field and thus would not have any effect on V_{oc}. However these ions can recombine with electrons moving towards n^+ and holes moving towards p^+. This increase in ion concentration, both from movement of thermally generated ions and light generated ions will reduce I_{sc} of the device. It seems that light generation of ions continue for a much longer duration than movement of

thermally generated ions and thus I_{sc} decreases for a longer time than increase saturation time for V_{oc}, however even the light generation of ions will saturate after a while and thus I_{sc} decreases saturates but slowly than V_{oc}.

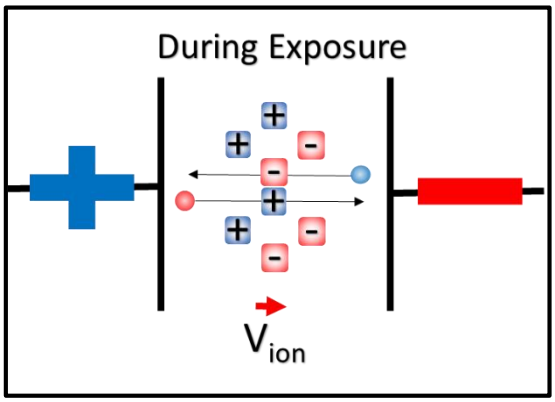

Fig.5.43: Proposed location and number of ions during and just after open circuit light exposure.

It should be noted that, generation of ions in presence of light can either be a direct process, i.e. photon is absorbed leading to excitation of ions, or it can be through the recombination of photogenerated electrons and holes. Energy released during recombination of electrons and holes can be sufficient to excite ion. Results on different bias exposures, suggest that generation of ions is most probably due to recombination of electron and holes. When all photo excited charge careers are collected, or when there is minimal recombination in the perovskite bulk layer, there is very little change in I_{sc} of the device. Whereas, decrease in I_{sc} increases as recombination in the perovskite bulk, or positive current in the device increases.

Rate of increase in V_{oc} will depend on applied photovoltage and thus intensity of the light, thus intense light will raise V_{oc} much quickly. However as increase in V_{oc} only depend on the initial thermally generated ions, saturation V_{oc} will be same for all intensity exposures.

Whereas, decrease in I_{sc} will depend on the number of excess ions generated by light. Thus intense light will reduce I_{sc} to a greater number.

5.6.2.3: After exposure

Now when light illumination is stopped, the photovoltage application on the device is removed and device will again see complete V_{bi}. In this V_{bi}, ions will move to respective interfaces. As ions move to interface, ionic field will increase. This will reduce effective V_{bi}. And thus V_{oc} will decrease and C will increase. As now apart from thermally generated ions we also have light generated ions, ionic field will be more than what comes only from thermally generated ions. And thus V_{oc} will decrease to a value lower than initial value. This drop in V_{oc} will depend on number of ions and thus in the case of intense light, V_{oc} will decrease more.

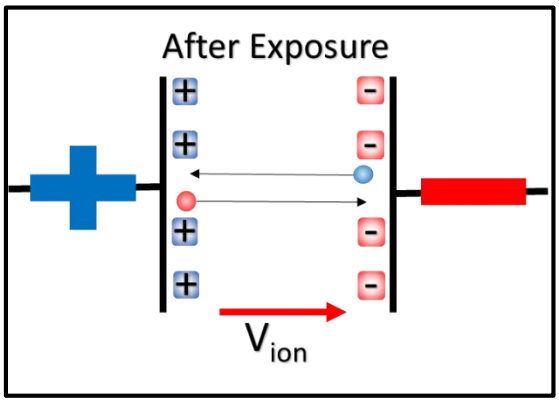

Fig.5.44: Proposed location and number of ions after exposure.

Note that now we have positive ions at p^+ interface thus electrons which are moving to n^+ will not see positive ions in its path and electron-ion recombination will decrease. Reduction in recombination will recover I_{sc} of the device. Decrease in V_{oc} for same I_{sc} would necessitate increase in I_0 which was observed in dark IV measurements.

Increased ions after exposure, would support increased hysteresis in the device after exposure.

5.6.2.4: During recovery

These ions at interface will be slowly neutralized with electrons (or holes) in transport layer. This neutralization will involve electron injection at p^+ side and hole injection in n^+ side.

This will result in a negative current which will be there even at zero bias in dark and thus dark IV will switch to higher positive voltages.

All these changes are because of light generated ions. As light generated ions slowly neutralize, number of ions at interface will decrease. Which will reduce ionic field and thus increase and recover V_{bi} to before exposure value. Recovery of V_{bi} will result in recovery of V_{oc} and Capacitance. Since no new ions are generated in perovskite bulk, I_{sc} of the device will stay same. Recovery of V_{oc} for same I_{sc} will result in recovery of I_o. As light generated excess ions are recovered, negative current in dark IV will also recover.

This recovery process will be thermally assisted as there would be more electrons and hole to neutralize ions at higher temperature. Thus annealing to higher temperature will recover device quickly.

The motion of ions might be grain boundary assisted and thus the degradation can be reduced by increasing grain size of the device.

5.7: Conclusion

In conclusion, in this chapter, we tried to understand the photostability of the perovskite solar cells. Before starting on photostability, first reported findings and suggested mechanisms of hysteresis and other anomalies in perovskite solar cells were discussed. A model was proposed based on ionic formation and ionic migration inside perovskite bulk, which are not widely accepted phenomena. This model could explain all reported anomalies in the perovskite solar cells.

Perovskite solar cells were fabricated in PIN ITO/NiO_x/perovskite/PCBM/Al architecture. Perovskite main layer was deposited by fast crystallization of Lewis base adduct solution, which

consistently yielded devices with power conversion efficiency of around 12%. This device was exposed in full solar spectrum under open circuit conditions and its photostability was studied.

It was observed that with exposure, V_{oc} of the device increases where I_{sc} decreased. V_{oc} increase saturated comparatively faster, whereas I_{sc} was saturated very slowly. Very intriguing results were observed in exposed device after stopping the exposure. Decreased I_{sc} increased and recovered very quickly whereas increased V_{oc} decreased to a value lower than that of before exposure and then it slowly increased and recovered.

The ionic motion model proposed for hysteresis, was then extended by considering light generation of ions. According to this model, after device formation, in the presence of built-in field, thermally generated ions migrate such that the positive ions move towards p^+ interface (negative towards n^+). This motion of the ions reduces effective V_{bi} and thus V_{oc} of the device to start with.

When the device is illuminated under open circuit conditions, as electric field in the bulk of device is reduced, ions move back to the bulk perovskite. This motion reduces the decrease in V_{bi} and thus results in increase in V_{oc}. During exposure, light also generates more ions in the bulk of the device thus increasing ionic concentration in the bulk even more. These increased ions recombine with the electrons and holes and thus reduce I_{sc} of the device.

When illumination is stopped in built-in field, excess ions move back to the interface thus decreasing V_{oc} to a value lower than the initial value. Reduction in ionic density in the bulk recovers I_{sc} of the device. The excess ions slowly neutralize with electrons/holes in transport layers which recovers ionic density to before the exposure level. As ionic location is completely recovered, V_{oc} of the device also gets completely recovered. At higher temperatures, the number of electrons/hole in the transport layer would be higher leading to faster neutralization. The model

also successfully described the effect of light intensity exposure on the device degradation and recovery.

Finally in this work, a model was proposed based on ionic motion, blocking at transport layers and light generation of ions, which successfully described all the observed photodegradation phenomena in PIN perovskite solar cells.

5.8: References

1. Kojima, A., et al., *Organometal Halide Perovskites as Visible-Light Sensitizers for Photovoltaic Cells.* Journal of the American Chemical Society, 2009. **131**(17): p. 6050-+.

2. Im, J.-H., et al., *6.5% efficient perovskite quantum-dot-sensitized solar cell.* Nanoscale, 2011. **3**(10): p. 4088-4093.

3. Kim, H.-S., et al., *Lead Iodide Perovskite Sensitized All-Solid-State Submicron Thin Film Mesoscopic Solar Cell with Efficiency Exceeding 9%.* Scientific Reports, 2012. **2**.

4. Burschka, J., et al., *Sequential deposition as a route to high-performance perovskite-sensitized solar cells.* Nature, 2013. **499**(7458): p. 316-+.

5. Zhou, H.P., et al., *Interface engineering of highly efficient perovskite solar cells.* Science, 2014. **345**(6196): p. 542-546.

6. Yang, W.S., et al., *High-performance photovoltaic perovskite layers fabricated through intramolecular exchange.* Science, 2015. **348**(6240): p. 1234-1237.

7. Saliba, M., et al., *Cesium-containing triple cation perovskite solar cells: improved stability, reproducibility and high efficiency.* Energy & Environmental Science, 2016.

8. Green, M.A., A. Ho-Baillie, and H.J. Snaith, *The emergence of perovskite solar cells.* Nature Photonics, 2014. **8**(7): p. 506-514.

9. Park, N.-G., *Perovskite solar cells: an emerging photovoltaic technology.* Materials Today, 2015. **18**(2): p. 65-72.

10. Stoumpos, C.C. and M.G. Kanatzidis, *The Renaissance of Halide Perovskites and Their Evolution as Emerging Semiconductors.* Accounts of Chemical Research, 2015. **48**(10): p. 2791-2802.

11. Gong, J., S.B. Darling, and F. You, *Perovskite photovoltaics: life-cycle assessment of energy and environmental impacts.* Energy & Environmental Science, 2015. **8**(7): p. 1953-1968.

12. Hailegnaw, B., et al., *Rain on Methylammonium Lead Iodide Based Perovskites: Possible Environmental Effects of Perovskite Solar Cells.* Journal of Physical Chemistry Letters, 2015. **6**(9): p. 1543-1547.

13. Niu, G., X. Guo, and L. Wang, *Review of recent progress in chemical stability of perovskite solar cells.* Journal of Materials Chemistry A, 2015. **3**(17): p. 8970-8980.

14. Leijtens, T., et al., *Stability of Metal Halide Perovskite Solar Cells.* Advanced Energy Materials, 2015. **5**(20).

15. Wang, D., et al., *Stability of perovskite solar cells.* Solar Energy Materials and Solar Cells, 2016. **147**: p. 255-275.

16. Nguyen Huy, T., Z. Ku, and H.J. Fan, *Recent Advances in Improving the Stability of Perovskite Solar Cells.* Advanced Energy Materials, 2016. **6**(3).

17. Yang, J.L., et al., *Investigation of CH3NH3PbI3 Degradation Rates and Mechanisms in Controlled Humidity Environments Using in Situ Techniques.* Acs Nano, 2015. **9**(2): p. 1955-1963.

18. Bryant, D., et al., *Light and oxygen induced degradation limits the operational stability of methylammonium lead triiodide perovskite solar cells.* Energy & Environmental Science, 2016.

19. Niu, G., et al., *Study on the stability of CH3NH3PbI3 films and the effect of post-modification by aluminum oxide in all-solid-state hybrid solar cells.* Journal of Materials Chemistry A, 2014. **2**(3): p. 705-710.

20. Kaltenbrunner, M., et al., *Flexible high power-per-weight perovskite solar cells with chromium oxide-metal contacts for improved stability in air.* Nature Materials, 2015. **14**(10): p. 1032-+.

21. Lei, Y., et al., *Intrinsic charge carrier dynamics and device stability of perovskite/ZnO mesostructured solar cells in moisture.* Journal of Materials Chemistry A, 2016.

22. Conings, B., et al., *Intrinsic Thermal Instability of Methylammonium Lead Trihalide Perovskite.* Advanced Energy Materials, 2015. **5**(15).

23. Leijtens, T., et al., *Overcoming ultraviolet light instability of sensitized TiO2 with meso-superstructured organometal tri-halide perovskite solar cells.* Nature Communications, 2013. **4**.

24. Wojciechowski, K., et al., *C-60 as an Efficient n-Type Compact Layer in Perovskite Solar Cells.* Journal of Physical Chemistry Letters, 2015. **6**(12): p. 2399-2405.

25. Ono, L.K., et al., *Pinhole-free hole transport layers significantly improve the stability of MAPbI(3)-based perovskite solar cells under operating conditions.* Journal of Materials Chemistry A, 2015. **3**(30): p. 15451-15456.

26. Guarnera, S., et al., *Improving the Long-Term Stability of Perovskite Solar Cells with a Porous Al2O3 Buffer Layer.* Journal of Physical Chemistry Letters, 2015. **6**(3): p. 432-437.

27. Mei, A.Y., et al., *A hole-conductor-free, fully printable mesoscopic perovskite solar cell with high stability.* Science, 2014. **345**(6194): p. 295-298.

28. Li, X., et al., *Outdoor Performance and Stability under Elevated Temperatures and Long-Term Light Soaking of Triple-Layer Mesoporous Perovskite Photovoltaics.* Energy Technology, 2015. **3**(6): p. 551-555.

29. Bag, M., et al., *Kinetics of Ion Transport in Perovskite Active Layers and Its Implications for Active Layer Stability.* Journal of the American Chemical Society, 2015. **137**(40): p. 13130-13137.

30. Snaith, H.J., et al., *Anomalous Hysteresis in Perovskite Solar Cells.* Journal of Physical Chemistry Letters, 2014. **5**(9): p. 1511-1515.

31. Tress, W., et al., *Understanding the rate-dependent J-V hysteresis, slow time component, and aging in CH3NH3PbI3 perovskite solar cells: the role of a compensated electric field.* Energy & Environmental Science, 2015. **8**(3): p. 995-1004.

32. Unger, E.L., et al., *Hysteresis and transient behavior in current-voltage measurements of hybrid-perovskite absorber solar cells.* Energy & Environmental Science, 2014. **7**(11): p. 3690-3698.

33. Kim, H.-S. and N.-G. Park, *Parameters Affecting I-V Hysteresis of CH3NH3PbI3 Perovskite Solar Cells: Effects of Perovskite Crystal Size and Mesoporous TiO2 Layer.* Journal of Physical Chemistry Letters, 2014. **5**(17): p. 2927-2934.

34. Zhao, Y., et al., *Anomalously large interface charge in polarity-switchable photovoltaic devices: an indication of mobile ions in organic-inorganic halide perovskites.* Energy & Environmental Science, 2015. **8**(4): p. 1256-1260.

35. Zhang, Y., et al., *Charge selective contacts, mobile ions and anomalous hysteresis in organic-inorganic perovskite solar cells.* Materials Horizons, 2015. **2**(3): p. 315-322.

36. Azpiroz, J.M., et al., *Defect migration in methylammonium lead iodide and its role in perovskite solar cell operation.* Energy & Environmental Science, 2015. **8**(7): p. 2118-2127.

37. Zhang, H.M., et al., *Dynamic interface charge governing the current-voltage hysteresis in perovskite solar cells.* Physical Chemistry Chemical Physics, 2015. **17**(15): p. 9613-9618.

38. Haruyama, J., et al., *First-Principles Study of Ion Diffusion in Perovskite Solar Cell Sensitizers.* Journal of the American Chemical Society, 2015. **137**(32): p. 10048-10051.

39. Heo, J.H., et al., *Hysteresis-less inverted CH3NH3PbI3 planar perovskite hybrid solar cells with 18.1% power conversion efficiency.* Energy & Environmental Science, 2015. **8**(5): p. 1602-1608.

40. Eperon, G.E., et al., *Inorganic caesium lead iodide perovskite solar cells.* Journal of Materials Chemistry A, 2015. **3**(39): p. 19688-19695.

41. Eames, C., et al., *Ionic transport in hybrid lead iodide perovskite solar cells.* Nature Communications, 2015. **6**.

42. van Reenen, S., M. Kemerink, and H.J. Snaith, *Modeling Anomalous Hysteresis in Perovskite Solar Cells.* Journal of Physical Chemistry Letters, 2015. **6**(19): p. 3808-3814.

43. Frost, J.M., K.T. Butler, and A. Walsh, *Molecular ferroelectric contributions to anomalous hysteresis in hybrid perovskite solar cells.* Apl Materials, 2014. **2**(8).

44. Shao, Y.H., et al., *Origin and elimination of photocurrent hysteresis by fullerene passivation in CH3NH3PbI3 planar heterojunction solar cells.* Nature Communications, 2014. **5**.

45. Zhao, K., et al., *Solution-processed inorganic copper(I) thiocyanate (CuSCN) hole transporting layers for efficient p-i-n perovskite solar cells.* Journal of Materials Chemistry A, 2015. **3**(41): p. 20554-20559.

46. Ip, A.H., et al., *A two-step route to planar perovskite cells exhibiting reduced hysteresis.* Applied Physics Letters, 2015. **106**(14).

47. Dualeh, A., et al., *Impedance Spectroscopic Analysis of Lead Iodide Perovskite-Sensitized Solid-State Solar Cells.* Acs Nano, 2014. **8**(1): p. 362-373.

48. Christians, J.A., J.S. Manser, and P.V. Kamat, *Best Practices in Perovskite Solar Cell Efficiency Measurements. Avoiding the Error of Making Bad Cells Look Good.* Journal of Physical Chemistry Letters, 2015. **6**(5): p. 852-857.

49. Tao, C., et al., *17.6% stabilized efficiency in low-temperature processed planar perovskite solar cells.* Energy & Environmental Science, 2015. **8**(8): p. 2365-2370.

50. Xiao, Z., et al., *Giant switchable photovoltaic effect in organometal trihalide perovskite devices.* Nature Materials, 2015. **14**(2): p. 193-198.

51. Leijtens, T., et al., *Mapping Electric Field-Induced Switchable Poling and Structural Degradation in Hybrid Lead Halide Perovskite Thin Films.* Advanced Energy Materials, 2015. **5**(20).

52. Deng, Y.H., Z.G. Xiao, and J.S. Huang, *Light-Induced Self-Poling Effect on Organometal Trihalide Perovskite Solar Cells for Increased Device Efficiency and Stability.* Advanced Energy Materials, 2015. **5**(20).

53. Stoumpos, C.C., C.D. Malliakas, and M.G. Kanatzidis, *Semiconducting Tin and Lead Iodide Perovskites with Organic Cations: Phase Transitions, High Mobilities, and Near-Infrared Photoluminescent Properties.* Inorganic Chemistry, 2013. **52**(15): p. 9019-9038.

54. Kutes, Y., et al., *Direct Observation of Ferroelectric Domains in Solution-Processed CH3NH3PbI3 Perovskite Thin Films.* Journal of Physical Chemistry Letters, 2014. **5**(19): p. 3335-3339.

55. Beilsten-Edmands, J., et al., *Non-ferroelectric nature of the conductance hysteresis in CH3NH3PbI3 perovskite-based photovoltaic devices.* Applied Physics Letters, 2015. **106**(17).

56. Coll, M., et al., *Polarization Switching and Light-Enhanced Piezoelectricity in Lead Halide Perovskites.* Journal of Physical Chemistry Letters, 2015. **6**(8): p. 1408-1413.

57. Meloni, S., et al., *Ionic polarization-induced current-voltage hysteresis in CH3NH3PbX3 perovskite solar cells.* Nature communications, 2016. **7**: p. 10334-10334.

58. Mizusaki, J., K. Arai, and K. Fueki, *IONIC-CONDUCTION OF THE PEROVSKITE-TYPE HALIDES.* Solid State Ionics, 1983. **11**(3): p. 203-211.

59. Egger, D.A., L. Kronik, and A.M. Rappe, *Theory of Hydrogen Migration in Organic-Inorganic Halide Perovskites.* Angewandte Chemie-International Edition, 2015. **54**(42): p. 12437-12441.

60. Walsh, A., et al., *Self-Regulation Mechanism for Charged Point Defects in Hybrid Halide Perovskites.* Angewandte Chemie-International Edition, 2015. **54**(6): p. 1791-1794.

61. Buin, A., et al., *Materials Processing Routes to Trap-Free Halide Perovskites.* Nano Letters, 2014. **14**(11): p. 6281-6286.

62. Tahara, H., et al., *Experimental Evidence of Localized Shallow States in Orthorhombic Phase of CH3NH3PbI3 Perovskite Thin Films Revealed by Photocurrent Beat Spectroscopy.* The Journal of Physical Chemistry C, 2016.

63. Yin, W.-J., T. Shi, and Y. Yan, *Unusual defect physics in CH3NH3PbI3 perovskite solar cell absorber.* Applied Physics Letters, 2014. **104**(6).

64. Yuan, Y. and J. Huang, *Ion Migration in Organometal Trihalide Perovskite and Its Impact on Photovoltaic Efficiency and Stability.* Accounts of Chemical Research, 2016. **49**(2): p. 286-293.

65. Yuan, Y., et al., *Photovoltaic Switching Mechanism in Lateral Structure Hybrid Perovskite Solar Cells.* Advanced Energy Materials, 2015. **5**(15).

66. Gottesman, R., et al., *Extremely Slow Photoconductivity Response of CH3NH3PbI3 Perovskites Suggesting Structural Changes under Working Conditions.* Journal of Physical Chemistry Letters, 2014. **5**(15): p. 2662-2669.

CHAPTER 6

CONCLUSIONS AND FUTURE WORK

6.1: Organic solar cells

In this work, two high efficiency polymers, PTB7 and PTB7-Th were compared. They have similar backbone with slight modification of sidechain. Both polymers were showed similar device performance. Photo-degradation experiments suggested that PTB7 is more stable than PTB7-Th, which is also supported by theoretical DFT calculations for α C-H bond energy. This suggests that, probably photo-degradation mechanism is guided through bond breaking of α C-H, even in PTB7 family.

We showed that, sidechain modification of a polymer can affect the intrinsic photostability of the polymer. This work can be taken further to test different sidechains to find more robust polymer. This work can also be tested for different polymeric backbones.

6.2: Perovskite solar cells

In this work, first, based on literature, we presented a complete model of ion migration to explain hysteresis. Then using this model, we built up a model to explain light induced changes in a NiO_x/perovskite/PCBM perovskite solar cell.

The model is based on (1) presence of thermally generated ions, (2) generation of ions under light and (3) movement of these ions with different bias conditions.

After device is fabricated, ionic motion leads to decrease in V_{oc} of the device, as ions move towards interfaces. When device is exposed under open circuit conditions, ions move back towards bulk of the perovskite, thus increasing V_{oc} of the device. During light exposure, more ions are also generated in the bulk of perovskite, leading to decrease in I_{sc}. When light exposure is stopped, ions again move to the interfaces. This time, since number of ions has increased, V_{oc} of the device reduces to a value lower than initial value. Reduction in ions in the bulk of the device, leads to recovery in I_{sc}. Excess ions generated by light, slowly neutralize and device recovers its V_{oc} and device performance.

We also showed that, neutralization of ions after exposure is thermally assisted process and device can be recovered quickly if it is annealed at higher temperature, supporting the model proposed here.

We showed that, at higher light intensity, ionic motion to bulk would be faster and thus V_{oc} rise would be faster. Ion generation rate at higher intensity would also be faster & higher, thus current reduction and rate of current reduction would be higher at higher light intensity. Decrease in V_{oc} after stopping light exposure, is also higher for device exposed to higher light intensity, as more ions are created at intense light, which is another verification of the model.

We showed that, rate of degradation depends on the grain size of the perovskite film, suggesting that probably, grain boundaries act as channels for ionic motion.

In this work, we presented a complete picture of light induced changes during and after light exposure in the device performance in NiO_x/perovskite/PCBM perovskite solar cell. All observed phenomena are explained using a model based on ion migration and generation of more ions. Impact of ion migration on stability of the device is thus explained in this work.

This work can be further improved by checking for this model in different architectures of perovskite solar cell. Effect of different transport layers can also be checked. Fabrication conditions of perovskites can also affect the ionic motion and hence device degradation under light, which can also be checked.

APPENDIX

ACCURATE CAPACITANCE MEASUREMENT

Measuring capacitance correctly can be tricky business and key for correct measurement is 1) Quality Factor and 2) choosing the correct equivalent circuit. Before going into details here, first one must understand how a LCR meters work.

In a typical LCR meter, device is subjected to small AC voltage. The meter measures voltage across and current through the device. And then from the ratio of these two, impedance (both real and imaginary part is determined).

$$\bar{Z} = \frac{\bar{V}}{\bar{I}} = R + jX$$

Quality factor is basically a parameter that determines how damped an oscillator is or in terms of LCR circuits, how much of power is being stored on reactance versus that which is being lost on resistance. LCR meter simply measures Q by taking the ratio of imaginary part of impedance to the real part.

$$Q = \frac{|X|}{R}$$

Thus, larger the Q, larger is the effect of C on final measurement and thus more accurate the measurement of C. Q smaller than 1, indicate that resistances are playing more significant role in determining the final impedance and thus measured value of C is being significantly affected from resistances. As a general rule, in this work, Q values below 1 will be considered not good enough for Capacitance measurements.

LCR meters used in this study were 2 terminal LCR meters. In two terminal LCR meter, for capacitance measurement, this impedance is then fitted to either series or parallel equivalent circuit depending on the user's choice to give values of R_s, C_s or R_p, C_p.

As series resistance will affect measurement significantly in low impedance devices, generally a series mode is selected for small impedance devices, whereas parallel mode is selected for high impedance devices. Hioki (manufacturer of the LCR meters used in this work) recommends using parallel mode for impedances higher than 10 kΩ and series mode for impedances lower than 100 Ω and either in between. In a previous work in Microelectronics Research Center, John Carr, recommended used 10 kΩ and 100 Ω as the limiting cases [1]. However, exact derivation of these numbers is not very clear. In this work we derive the exact point where equivalent modes needs to be switched. In the measurement of capacitance spectroscopy, value of impedance goes down with increase in frequency and thus here we calculate frequency above which LCR meter should be switched from parallel equivalent mode to series equivalent mode.

A typical solar cell without any lead inductance can be modelled by the presence of both series and parallel resistance and shown in Fig. A.1.

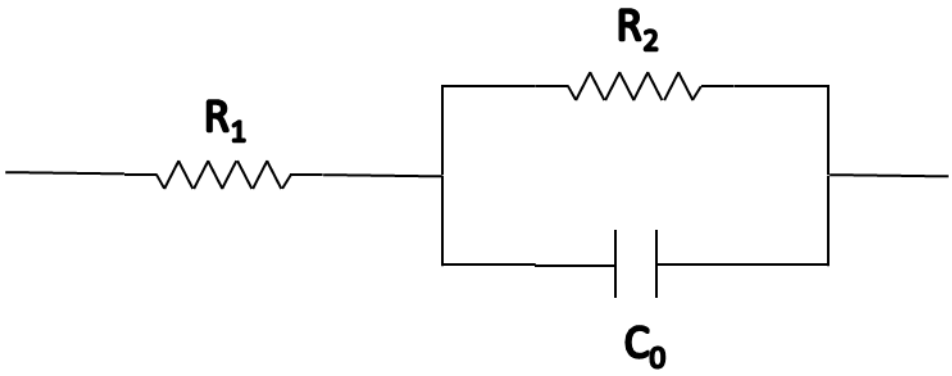

Fig. A.1: Equivalent circuit for a solar cell, assuming single diode model

Here, R_1 is the series resistance in the circuit, R_2 the parallel resistance and C_0 is the capacitance of the solar cell under measurement.

Now for such a circuit, overall impedance would be

$$Z = R_1 + R_2 \Uparrow\Uparrow C_0$$

Or

$$Z = \left(R_1 + \frac{R_2}{1 + R_2^2 \omega^2 C_0^2}\right) + j\left(\frac{R_2^2 \omega C_0}{1 + R_2^2 \omega^2 C_0^2}\right) \quad (1)$$

As per the user choice, LCR meter will fit this Z in either series or parallel equivalent circuit to calculate R_s, C_s or R_p, C_p.

If chosen series mode,

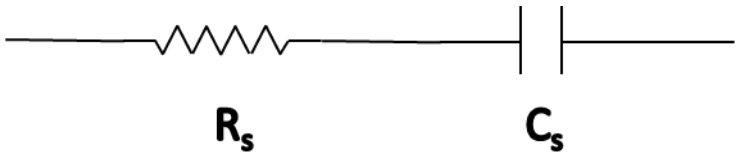

Fig. A.2: Series Equivalent Circuit for R_s, C_s estimation

In series mode, impedance comes out to be,

$$Z = R_s - j\frac{1}{\omega C_0} \quad (2)$$

Thus, when asked for series equivalent Circuit, LCR meter will fit real part of equation (1) into real part of (2) giving,

$$\boxed{R_s = R_1 + \frac{R_2}{1 + R_2^2 \omega^2 C_0^2}} \quad (3)$$

And similarly by fitting imaginary part of (1) into that of (2) gives us,

$$C_s = \frac{1 + R_2^2 \omega^2 C_0^2}{R_2^2 \omega^2 C_0}$$

Or,

$$\boxed{C_s = C_0 + \frac{1}{R_2^2 \omega^2 C_0}} \quad (4)$$

Thus, LCR meter, in series mode, will estimate capacitance value higher than the actual value. At lower frequencies this difference in estimated C_s and actual value will be very high, whereas at high frequencies, estimated C_s will approach actual value of C.

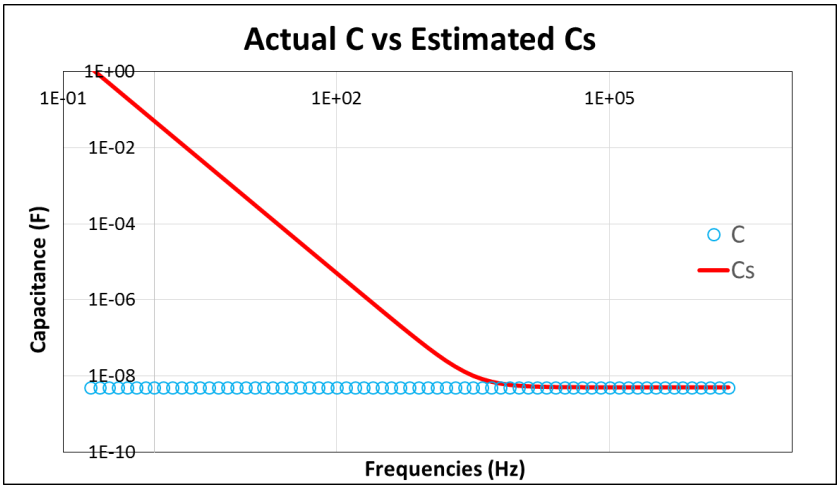

Fig. A.3: Value of C_s that LCR meter will estimate for typical values organic/perovskite solar cell with C_0 (5 nF), R_1 (50 Ω) and R_2 (10 kΩ)

If parallel mode is chosen,

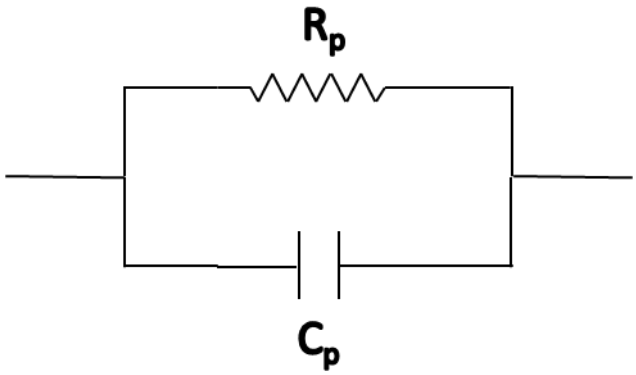

Fig. A.4: Parallel Equivalent Circuit for R_p, C_p estimation

In parallel mode, equation are slightly complicated as equivalent impedance is,

$$Z = \frac{R_p}{1 + R_p^2 \omega^2 C_p^2} + j \frac{R_p^2 \omega C_p}{1 + R_p^2 \omega^2 C_p^2} \tag{5}$$

By fitting real and imaginary parts, we get

$$\frac{R_p}{1 + R_p^2 \omega^2 C_p^2} = R_1 + \frac{R_2}{1 + R_2^2 \omega^2 C_0^2} \tag{6}$$

And,

$$\frac{R_p^2 \omega C_p}{1 + R_p^2 \omega^2 C_p^2} = \frac{R_2^2 \omega C_0}{1 + R_2^2 \omega^2 C_0^2} \tag{7}$$

Dividing (7) by (6) gives us,

$$R_p C_p = \frac{R_2^2 C_0}{R_1 + R_2 + R_1 R_2^2 \omega^2 C_0^2} \tag{8}$$

Dividing square of (8) by (7) gives us

$$C_p = \frac{(1 + R_2^2 \omega^2 C_0^2) R_2^2 C_0}{(R_1 + R_2 + R_1 R_2^2 \omega^2 C_0^2)^2} \times \frac{1}{1 + R_p^2 \omega^2 C_p^2} \tag{9}$$

Again, putting $R_p C_p$ from (8) to (9)

$$C_p = \frac{(1 + R_2^2 \omega^2 C_0^2) R_2^2 C_0}{R_1^2 + R_2^2 + 2R_1 R_2 + 2R_1^2 R_2^2 \omega^2 C_0^2 + 2R_1 R_2^3 \omega^2 C_0^2 + R_1^2 R_2^4 \omega^4 C_0^4 + R_2^4 \omega^2 C_0^2}$$

Or

$$C_p = \frac{(1 + R_2^2 \omega^2 C_0^2) R_2^2 C_0}{(1 + R_2^2 \omega^2 C_0^2)(R_1^2 + R_2^2 + 2R_1 R_2 + R_1^2 R_2^2 \omega^2 C_0^2)}$$

,

Or,

$$C_p = \frac{R_2^2 C_0}{R_1^2 + R_2^2 + 2R_1 R_2 + R_1^2 R_2^2 \omega^2 C_0^2} \tag{10}$$

Or,

$$C_p = C_0 - \frac{R_1^2 + 2R_1R_2 + R_1^2R_2^2\omega^2C_0^2}{R_1^2 + R_2^2 + 2R_1R_2 + R_1^2R_2^2\omega^2C_0^2} \quad (11)$$

And putting (10) in (8)

$$R_p = \frac{R_1^2 + R_2^2 + 2R_1R_2 + R_1^2R_2^2\omega^2C_0^2}{R_1 + R_2 + R_1R_2^2\omega^2C_0^2}$$

Or,

$$R_p = R_1 + R_2 - \frac{R_1R_2^3\omega^2C_0^2}{R_1 + R_2 + R_1R_2^2\omega^2C_0^2} \quad (12)$$

Thus, LCR meter, in parallel mode, will estimate capacitance value lower than the actual value. Value of C_p will decrease with increase in frequency. Thus, at lower frequencies C_p will give better estimation of actual value of C than at higher frequencies.

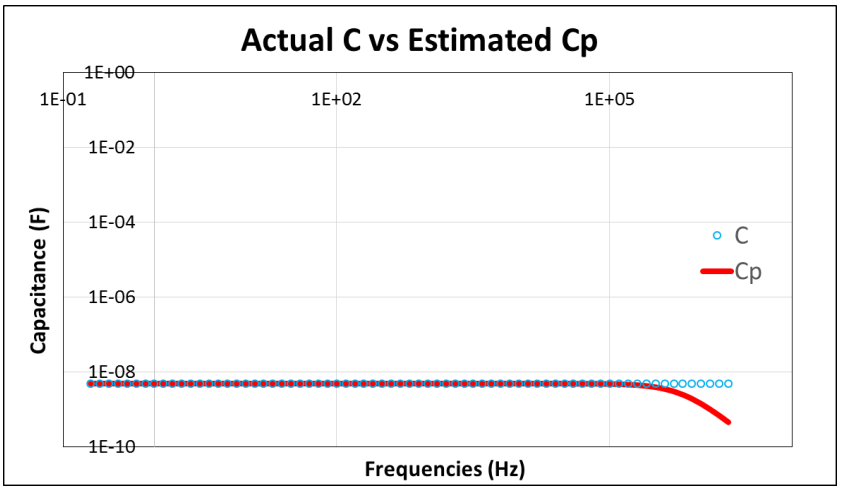

Fig. A.5: Value of C_s that LCR meter will estimate for typical values organic/perovskite solar cell with C_0 (5 nF), R_1 (50 Ω) and R_2 (10 kΩ)

We have showed that C_p estimated actual value capacitance more accurately than C_s at lower frequencies and vice-versa. The exact frequency where C_s estimation is better than C_p estimation can be given by,

$$C_0 - C_p = C_s - C_0$$

Or, $$\frac{R_1^2 + 2R_1R_2 + R_1^2R_2^2\omega^2C_0^2}{R_1^2 + R_2^2 + 2R_1R_2 + R_1^2R_2^2\omega^2C_0^2} = \frac{1}{R_2^2\omega^2C_0}$$

For simplicity, substituting, $R_2^2\omega^2C_0^2 = x$

Gives $(R_1^2 + 2R_1R_2)x + R_1^2x^2 = R_1^2 + R_2^2 + 2R_1R_2 + R_1^2x$

us,

$$R_1^2x^2 + 2R_1R_2x - (R_1 + R_2)^2 = 0$$

$$x = \frac{-2R_1R_2 \pm \sqrt{4R_1^2R_2^2 + 4R_1^2(R_1 + R_2)^2}}{4R_1^2}$$

As, $R_2^2\omega^2C_0^2 > 0$, we can neglect the negative solution

$$R_2^2\omega^2C_0^2 = \frac{\sqrt{R_1^2R_2^2 + R_1^2(R_1 + R_2)^2} - R_1R_2}{R_1^2}$$

$$\omega = \sqrt{\frac{\sqrt{R_1^2R_2^2 + R_1^2(R_1 + R_2)^2} - R_1R_2}{R_1^2R_2^2C_0^2}} \quad (13)$$

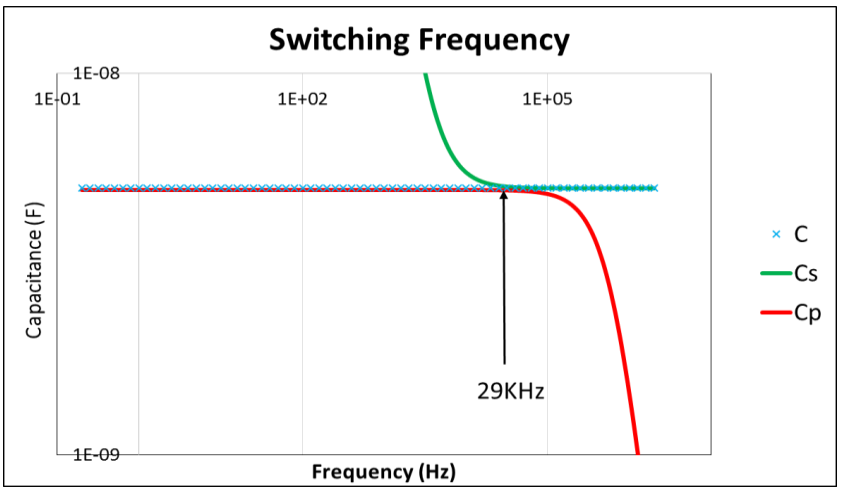

Fig. A.6: Switching Frequency for a typical values organic/perovskite solar cell with C_0 (5 nF), R_1 (50 Ω) and R_2 (10 kΩ).

Thus, if R_1, R_2 and C_0, are known the switching frequency can be calculated.

Exact value of C_0 cannot be found as these solar cell measurements, value of capacitance changes with frequencies. However change in capacitance is not that big and based on experience and typical values of R_1, R_2 for the solar cells, C_s value at around 50 KHz can be used as rough estimation of value of C_0 at the switching frequency.

In a solar cell, R_1 and R_2 should not have much dependence on frequency.
Eq. (3) suggests that R_s at very high frequencies goes to R_1. And thus value of R_s at 200 KHz (maximum possible frequency on Hioki LCR meters) can be considered to be roughly equal to the value of R_1.
Eq. (12) suggests that at very low frequencies R_p goes to R_1+R_2. After knowing R_1 from R_s at very high frequency, R_2 can be roughly estimated by the value of R_p at very low frequency subtracted by R_1.

Once we know values of R_1, R_2 and C_0, ω can also be roughly estimated and CF measurements can be done accordingly.

Most important thing is to measure CV with correct equivalent circuit. If wrong equivalent circuit is used CV measurements done at high frequency can show anomalous results as shown below and thus care must be taken by choosing correct equivalent circuit mode for CV measurements at various frequencies.

Another interesting way to determine switching frequency has been thought. This way is based on the value of Q. In parallel equivalent circuit, $Q = R\omega C$. Thus Q will increase with

frequency. In series equivalent circuit, $Q = \frac{1}{R\omega C}$, and thus Q decreases with ω. When Q is plotted against frequency, interesting behavior is observed that Q initially increases with frequency and then decreases with frequency. Exact determination of Q with frequency can be determined by taking the ratio of imaginary part to real part of impedance.

$$Q = \frac{X}{R}$$

$$Q = \frac{\frac{R_2^2 \omega C_0}{1 + R_2^2 \omega^2 C_0^2}}{R_1 + \frac{R_2}{1 + R_2^2 \omega^2 C_0^2}}$$

$$Q = \frac{R_2^2 \omega C_0}{R_1 + R_2 + R_1 R_2^2 \omega^2 C_0^2}$$

Thus change in Q direction will happen at

$$\frac{dQ}{d\omega} = \frac{(R_1 + R_2 + R_1 R_2^2 \omega^2 C_0^2) R_2^2 C_0 - R_2^2 \omega C_0 \times 2 R_1 R_2^2 \omega C_0^2}{(R_1 + R_2 + R_1 R_2^2 \omega^2 C_0^2)^2} = 0$$

$$R_1 + R_2 - R_1 R_2^2 \omega^2 C_0^2 = 0$$

$$\omega = \sqrt{\frac{R_1 + R_2}{R_1 R_2^2 C_0^2}}$$

REFERENCES

1. Carr, J.A. and S. Chaudhary, *On accurate capacitance characterization of organic photovoltaic cells.* Applied Physics Letters, 2012. **100**(21).

2. Muntasir, T. and S. Chaudhary, *Understanding defect distributions in polythiophenes via comparison of regioregular and regiorandom species.* Journal of Applied Physics, 2015. **118**(20).